

CONCEPTUAL DESIGN REPORT

Scientific Instrument High Energy Density Physics (HED)

21 May 2013

This report was released as a preliminary version in May 2013.
It was edited and released as a final version in December 2013.

*M. Nakatsutsumi and Th. Tschentscher
for the Scientific Instrument HED (WP82)
at European XFEL*

*with contributions from
T. Cowan, A. Ferrari, H.-P. Schlenvoigt (HZDR),
K. Appel, J. Stempfer, and M. v. Zimmermann (DESY)*

European X-Ray Free-Electron Laser Facility GmbH

Albert-Einstein-Ring 19

22761 Hamburg

Germany



Contents

1	Executive summary	5
2	Introduction and overview	9
2.1	Location of the HED instrument	10
2.2	External contributions	12
2.3	CDR review by HED-ART	14
3	Scientific objectives	15
3.1	Condensed matter at extreme excitation.....	15
3.2	Solid-density plasmas.....	26
3.3	Quantum states of matter	36
3.4	Summary of science requirements	40
4	X-ray techniques and requirements	43
4.1	Pump–probe experiments	43
4.2	X-ray excitation and pumping	45
4.3	X-ray probing	47
4.4	Experiment geometries.....	53
4.5	Summary of instrumentation requirements	55
5	X-ray beam delivery	59
5.1	Major requirements.....	59
5.2	Time delivery patterns	62
5.3	Radiation properties of the SASE2 undulator.....	63
5.4	X-ray beam transport components	66
5.5	X-ray diagnostic devices.....	89
5.6	Vacuum system	93
5.7	Equipment protection system (EPS)	94
6	Optical laser installations	95
6.1	“The Laser Plan” for the HED instrument	95
6.2	Pump–probe laser system (PP-OL)	101
6.3	100 TW ultrahigh-intensity short-pulse laser system (UHI-OL).....	105
6.4	100 J nanosecond high-energy laser system (HE-OL)	108
6.5	Additional laser systems.....	111
6.6	Future installation of high-energy laser systems	113
6.7	OL beam transport.....	115
6.8	Laser synchronization and diagnostics	119

7	Interaction chambers and ancillary instrumentation	123
7.1	High-resolution interaction chamber (IA1).....	124
7.2	High-energy interaction chamber (IA2)	125
7.3	Pulsed magnetic fields chamber (IA3).....	126
7.4	High repetition rate sample delivery	127
7.5	Detector requirements	128
7.6	Spectrometers and other ancillary instrumentation	130
8	Experiment hall layout	131
8.1	Transport tube	133
8.2	X-ray optics hutch (HED-OPT)	134
8.3	Experiment enclosure (HED-EXP)	136
8.4	Control room (HED-CTR)	143
8.5	SASE2 laser laboratory (SASE2-LAS).....	144
8.6	HED laser room (HED-LAS).....	145
8.7	Infrastructure rooms (HED-RK1 and HED-RK2)	146
9	Project issues.....	149
9.1	Interfaces to other work packages	149
9.2	Work breakdown structure.....	160
9.3	Schedule outline	162
A	Acknowledgements	163
B	Report on the HED-ART meeting	165
C	References.....	171

1 Executive summary

High energy density (HED) matter is defined as having an energy density above $10^{11} \text{ J}\cdot\text{m}^{-3}$, which is equivalent to 100 GPa (1 Mbar) pressure and 500 T magnetic pressure. The scientific objectives of the High Energy Density Physics instrument (HED instrument) at the European XFEL are to create and explore HED states using the particular features of X-ray free-electron laser (FEL) radiation. Strongly excited solid but below-HED states are also considered to be a key science area, as such transient states are precursors to the formation of HED states in laboratory experiments.

Key science areas at the HED instrument are the following:

- Solid-matter properties following extreme excitation by various means
- Solid matter in states of extreme pressure and density exceeding parameters that can be reached using static compression techniques
- Complex solids in very high pulsed magnetic fields
- Warm dense matter (WDM) and hot dense matter (HDM) systems
- Isochoric creation of WDM using X-ray FEL radiation
- Plasma physics particularly in electron-relativistic regime
- Quantum states generated by extremely high-field laser pulses

Experiments and applications in these scientific areas are generally performed in pump–probe mode, where a first pulse (X-ray or optical laser) excites a sample, and a second pulse (typically, X-ray) probes the sample a defined delay time later.

The X-ray beam delivery system at the HED instrument was optimized for the photon energy range 5–20 keV. The ranges 3–5 keV and 20–24 keV are available too, albeit with certain performance limitations. The X-ray beam size on sample will range from a few micrometres to a maximum of a few millimetres. Various spot sizes will be achieved using compound refractive beryllium lenses (Be-CRL). The maximum focused intensity achievable will be

on the order of 10^{17} – 10^{18} W·cm⁻². The X-ray pulse duration will be 2–100 fs, depending on electron bunch compression. The natural relative bandwidth will be 10^{-3} , but higher resolutions of 10^{-4} will be provided using a channel-cut silicon crystal monochromator. Reaching higher resolution is under consideration. In addition, by means of a split and delay device installed ~ 100 m upstream from the sample, the X-ray pulse can be split into two pulses with a maximum respective delay ranging from a few picoseconds to > 20 ps, depending on photon energy. For the photon energy range 3–5 keV, the larger divergence of the beam and the higher absorption of the CRL will limit the X-ray performance. Table 1-1 shows a brief summary of the X-ray performance at the HED instrument.

Table 1-1. Brief summary of the X-ray FEL beam parameters on sample at the HED instrument

Photon energy	Photon number on sample	Maximum intensity	Smallest spot size	Largest spot size	Energy
keV	/pulse	Wcm ⁻²	μm		mJ
5–24	> 10 ¹² at 5–10 keV > 10 ¹¹ at > 10 keV	> 10 ¹⁷	2–3	> mm	~ 3 mJ at 5 keV, > 1mJ for < 20 keV > 0.7 mJ for > 20 keV
3–5	> 10 ¹⁰	> 10 ¹⁶ *	~ 4 *	> mm	> 1 mJ

* For a few selected energies

To achieve the science goals outlined above, the HED instrument will comprise a large class of X-ray techniques: X-ray diffraction (XRD), X-ray absorption spectroscopy (XAS), inelastic X-ray scattering (IXS), small-angle X-ray scattering (SAXS), X-ray (coherent) imaging (XI), X-ray photon correlation spectroscopy (XPCS), and X-ray emission spectroscopy (XES).

A particularity of the HED instrument will be the installation of high-power optical laser (OL) systems and a pulsed high-field magnet (HFM), which will allow the creation of excited states.

At present, these systems include the following:

- 1 High-energy optical laser (HE-OL) beyond 100 J/pulse
- 2 Ultrahigh-intensity optical laser (UHI-OL) beyond 10^{18} W/cm² focused intensity
- 3 10–250 GW high-repetition pump–probe optical laser (PP-OL)
- 4 High-field pulsed magnet providing ≥ 30 T magnetic field

The anticipated properties of the OL and HFM systems are shown in Table 1-2, including potential upgrades. Precise temporal synchronization and spatial overlap between these systems and the X-rays is one of the challenges at the HED instrument. A particular requirement for the UHI-OL operation is the need for radiation protection of the experiment area. For this reason, the HED experiment area will be enclosed by 0.5–1.0 m thick concrete shielding walls. More details are given in Chapter 8, “Experiment hall layout”.

Most of the experiments at the HED instrument will use solid samples that are irreversibly damaged after strong excitation. The necessity of refreshing solid samples will limit the useable repetition rate for these experiments to 10 Hz, while the European XFEL can provide up to 4.5 MHz inside X-ray pulse trains. Similarly, the UHI-OL and HE-OL systems can be operated at repetition rates of max. 1–10 Hz due to cooling requirements of the laser amplifiers. Therefore, a large class of experiments at the HED instrument will be carried out at 10 Hz or even below. However, the majority of X-ray delivery components will be designed for the full repetition rate of the European XFEL. This is because some experiments can benefit from using the high intra-pulse-train repetition rates between 100 kHz and 4.5 MHz, and also in order not to exclude future instrumentation developments. The HED instrument will be optimized for fast turnover of experiment setups in order to allow a maximum number of experiments to be performed. For this purpose, the use

of dedicated chambers and platforms is being considered, which will likewise minimize the preparation time for each experiment.

Table 1-2. Brief summary of optical laser systems and high-field pulsed magnets to be installed at the HED instrument. More details can be found in Chapter 6, “Optical laser installations”.

	Abbreviation	Repetition [Hz]	Wavelength [nm]	Pulse energy	Pulse duration	Max. power or B field	Remarks
Pump–probe laser	PP-OL	4.5 M	~ 800	0.2 mJ / 4.5 MHz 5 mJ / 200 kHz	15–00 fs	10–250 GW	NOPA
		200 k	~ 1030	100 mJ	0.8 ps or 0.5 ns	~ 100 GW	Yb amplifier
High-energy laser	HE-OL	1–10	1057 or 1064	~ 150 J/ ω ~ 100 J/2 ω	2–20 ns	~ 75 GW	Nd-glass or Nd-YAG
		< 1	528 or 532	> kJ	2–20 ns	> 500 GW	Beyond 2016
Ultrahigh-intensity laser	UHI-OL	10	~ 800	3–5 J	~ 30 fs	~ 100 TW	Ti-sapphire
		~ 1		10–30 J	~ 30 fs	~ PW	Beyond 2016
High-field pulsed magnet	HFM	0.1 – ~ 0.01	—	~ 30 kJ	> 100 μ s	> 30 T	—
		< 0.01	—	> MJ	—	TBD	Beyond 2016

2 Introduction and overview

This document describes the conceptual design of the High Energy Density Physics scientific instrument (HED instrument) at the European XFEL. The HED instrument will be one of the six baseline instruments of the facility. It will provide to a wide community of condensed-matter, plasma, and high-power laser physicists a scientific instrument for experiments not possible anywhere else in the world.

This conceptual design report (CDR) is based on the requirements emerging from the scientific objectives of the HED instrument and the anticipated X-ray techniques to be fielded at this instrument. Major subsystems of the HED instrument are described, including the beam transport elements, the instrument components, and the requirements for further subsystems and infrastructure. Furthermore, the interfaces of the HED instrument to other work packages of the European XFEL project are described with the goal of realizing a highly integrated project.

This CDR has been drawn up in a very short period of only six months, and the design status of the different sections varies widely. After successful review of the CDR in spring 2013, we aim to complete open tasks before establishing technical designs of the most important and long-lead components within about one year. During this period, the design, in particular of the experiment area, will be refined in close collaboration with the future user community. This schedule is considered timely to enable the start of construction of the instrument inside the experiment hall in summer 2015 and first beam in the first half of 2016. Initial user operation at the HED instrument is foreseen to start during the last quarter of 2016.

2.1 Location of the HED instrument

The HED instrument will be located at the SASE2 FEL of the European XFEL. The SASE2 source is a gap-tunable undulator system designed to deliver FEL radiation above 2.3 / 4.1 / 6.4 keV and up to 24 keV for the designated accelerator operation points of 10.5 / 14.0 / 17.5 GeV electron energy [1]. An overview of radiation properties is given in Table 5-2.

The SASE2 undulator and the majority of X-ray transport components are located in underground tunnels. The undulator and the first optical elements are situated inside tunnel section XTD1, while the monochromator and other components of the HED beam transport system are located in XTD6, the southern-most tunnel leading into the experiment hall XHEXP1 (see Chapter 5, “X-ray beam delivery”). The SASE2 X-ray beam transport system allows distribution of FEL radiation to three laterally separated scientific instruments (see Figure 2-1). The third instrument (NNN) will not be built initially, but space for future construction will be kept free. A floor plan for the SASE2 instruments has been developed and is shown in Figure 2-1. The layout basically features three staggered X-ray beams horizontally displaced by ~ 1.4 m. The HED instrument will be located on the very end of the SASE2 south branch (S2S). In addition to the HED instrument, the Materials Imaging and Dynamics (MID) instrument will feature coherence applications with the requirement of a wide horizontal displacement.

The location of the HED instrument at the SASE2 undulator restricts applications to the hard X-ray regime above 3 keV. As a result of workshops with the user community, and from the overall layout of the European XFEL facility, two instruments for high energy density physics had initially been requested by the user community, one for hard (> 3 keV) and one for soft (< 3 keV) X-rays. After considering user community input, a prioritization for the hard X-ray HED instrument was developed. This instrument was included in a proposal for selection of the first six top-prioritized scientific instruments at the European XFEL and confirmed by the Science and Technology Issues working group, the predecessor of the European XFEL Scientific Advisory Committee (SAC), on its meeting in fall 2007. Subsequently, the hard X-ray

HED instrument was presented to the user community at a variety of meetings, including a dedicated user workshop in spring 2009 in Oxford. It is clear that the choice of hard X-rays restricts the applicability of the HED instrument in certain areas, like X-ray heating, resonant absorption by light elements, or resonant absorption of plasma lines in the soft X-ray regime. For some of these applications, the use of the soft X-ray instruments—Small Quantum Systems (SQS) or Spectroscopy and Coherent Scattering (SCS)—should be considered instead.

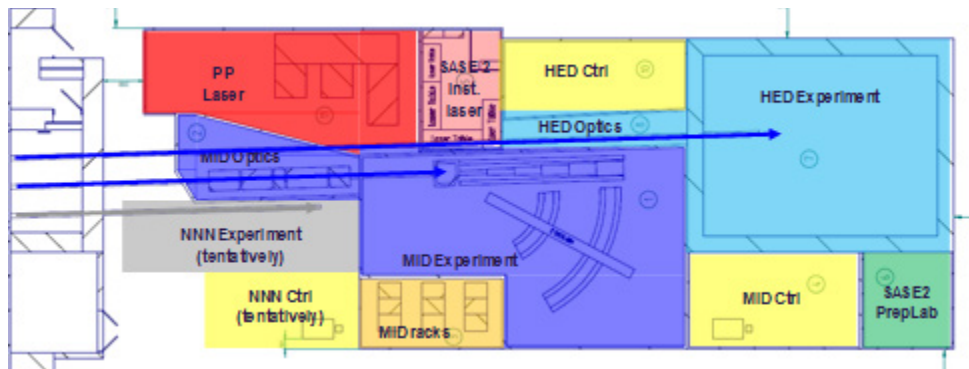
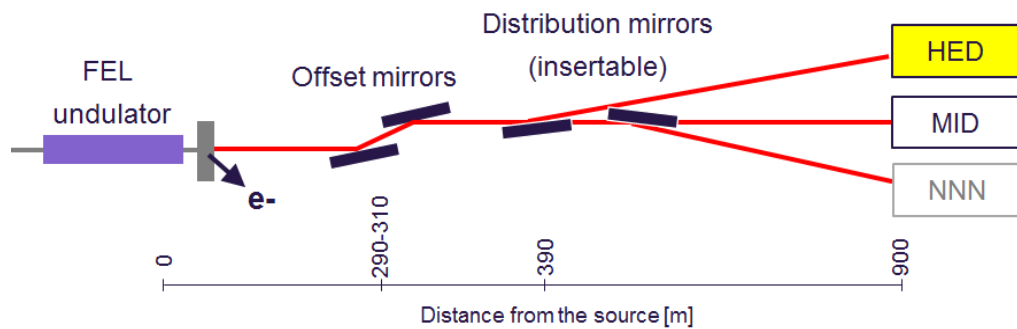


Figure 2-1. Sketch of the SASE2 beam transport system (top) and of the floor layout of SASE2 instruments HED (blue), MID (purple), and NNN (grey) inside the experiment hall (bottom). Red areas indicate laser rooms while green areas mark laboratory space.

2.2 External contributions

This document describes mainly the baseline instrumentation of the HED scientific instrument. This baseline instrumentation will be achieved through manpower and budget of European XFEL. In addition, European XFEL has received a proposal for contributions to the HED instrument by an external user consortium (UC), the Helmholtz International Beamline for Extreme Fields (HIBEF). This contribution will include large laser systems, their diagnostics and infrastructure, a high-field pulsed magnet, additional X-ray instrumentation components, personnel, and more. These additional systems and instrumentation will be fully integrated into the European XFEL and will be available to all users of the HED instrument. At present, not all of the details of this contribution have been identified, but the baseline design of the HED instrument is conceived in a way that allows for later integration of additional instrumentation. For this reason, it is, in several cases, necessary to describe the anticipated instrumentation beyond the HED instrument baseline.

An important contribution by the HIBEF consortium will be the addition of OL systems. Since all laser systems are related to each other, a consistent HED OL concept is required.

While the full concept still needs to be established between European XFEL and the user consortium, a few boundary conditions are clear already:

- The laser systems will serve as reliable tools supporting the scientific programme at the HED instrument. For this reason, the system performance in terms of reliability, ease of operation, up time, maintenance, etc. is equally if not more important than the peak performance.
- One performance challenge for the OL systems exists, however: the repetition rate of the European XFEL facility, which must be matched as closely as possible by the laser systems. While the intra-pulse-train repetition is (in all likelihood) impossible to match, the 10 Hz repetition rate will be targeted for all laser systems (possibly at reduced pulse energy).

- The suite of optical lasers for the HED instrument includes the PP laser system at SASE2 (see Chapter 6, “Optical laser installations”), at least one ultrashort-pulse laser system, at least one long-pulse laser system, and additional lasers for sample characterization (e.g. for velocity interferometer system for any reflector (VISAR) techniques).

Another contribution to the HED instrument is the provision of an X-ray split and delay device through the German Federal Ministry of Education and Research (BMBF) funding grant 05K10M2, realized by the X-ray physics group at the University of Münster, Germany. This device, and its integration into the X-ray beam transport system, are described in detail in the Chapter 5, “X-ray beam delivery”.

This CDR is organized as follows: After this introduction, the scientific objectives are summarized in Chapter 3, “Scientific objectives”. Chapter 4, “X-ray techniques and requirements”, discusses the X-ray techniques and their requirements for X-ray beam delivery and instrumentation. Chapter 5, “X-ray beam delivery”, describes the proposed X-ray beam delivery system, summarizes the source parameters, and provides a description of the common and HED-specific components of the SASE2 X-ray beam transport system. This chapter also includes a section discussing the beam delivery patterns for the HED instrument and the related heat load and damage issues. This is followed in Chapter 6, “Optical laser installations”, by a description of the OL installations. Chapter 7, “Interaction chambers and ancillary instrumentation”, describes the concepts for the various interaction chambers and their ancillary instrumentation requirements. Chapter 8, “Experiment hall layout”, provides the experiment hall layout of the HED instrument with its optics, experiments, laser and control areas, and their respective infrastructure requirements. Finally, Chapter 9, “Project issues”, describes project-relevant issues, such as interfaces to other work packages, work breakdown, schedule outline, and resource estimates.

2.3 CDR review by HED-ART

For external advice and as an interface to the HED user community, an HED-specific advisory review team (HED-ART) has been established. On 11 March 2013, the HED-ART met to discuss and review the HED conceptual design. The report of this meeting is included in Appendix B, “Report on the HED-ART meeting”. During the meeting, many points were brought up.

Some of the most important recommendations for the further HED instrument design are listed in the following:

- Develop a detailed experiment plan for a few key experiments. This plan should then guide the exact layout of the instrument. It is important to cover all needs and phases of an experiment to obtain a full overview of needs. The following experiments were proposed: “Dynamic compression” and “Relativistic laser plasma interaction”, with “X-ray generation of WDM”, “Strong-field physics”, and “High magnetic fields” suggested for a later date.
- Improve the discussion of requirements for two-dimensional (2D) area detectors and foresee their implementation from the start.
- Concern about the proposal of implementing three interaction chambers in the experiment room is due to be expected, but space requirements for varying experiment setups were not quantified. For alleviation, the proposal was made to move the Fourier domain interferometer (FDI) and VISAR laser setups to the HED laser room.

In addition, several detailed comments were made. In part, these suggestions and proposed solutions have been integrated into this final version of the CDR. Where appropriate, comments have been included in the text.

3 Scientific objectives

 This section is only a brief summary of the scientific objectives and does not replace a complete science case for the HED instrument.

The scientific case of the HED instrument has been discussed with the plasma and high-power laser physics communities—first in 2000 and 2001, then in 2006 in great detail at a dedicated workshop in Paris, and finally in 2009 at another workshop in Oxford. This science case had been included in the technical design reports (TDRs) of the European XFEL of 2001 [2] and 2006 [3]. First, in 2005, the requirement for a high-energy laser to excite solids by shock and ramp compression was brought up. This aspect of using the FEL to study matter in extreme excitation states, but still in a condensed-matter state, has in recent years added a high-pressure and materials science case to the scientific objectives of the HED instrument. Even more recently, in 2011, the idea was issued to use high-power lasers to create quantum states and to probe them using the high-brilliance FEL pulses. In the following sections, a brief outline of the different types of applications is given and their primary goals are introduced.

3.1 Condensed matter at extreme excitation

The investigation of condensed-matter systems in states of extreme excitation using X-rays is often limited by the fact that either the experiments cannot be performed in a repetitive fashion because the samples are irreversibly modified, or the photon flux per time interval of observation is too small to collect significant data sets. This limitation is related to the fact that the processes to be observed occur on either the ultrafast (femtosecond to picosecond) or fast (sub-millisecond) timescale. Some investigations have been performed using synchrotron radiation and laser-based X-ray sources, but X-ray FELs offer significantly improved experiment conditions. Synchrotron radiation has the disadvantage of much smaller flux in time intervals below 1 ms and, in particular, a much smaller number of photons in

each X-ray pulse. In addition, the longer pulse duration makes it impossible to study processes faster than a few 10 ps. High-intensity optical laser-based bremsstrahlung or fluorescence X-ray sources have a minimum pulse duration of typically a few picoseconds and do not allow the study of sub-picosecond processes either. In addition, the X-rays delivered by these sources are neither directional nor coherent, and only a small fraction can be used in experiments.

In general, applications in this area are closely related to the investigation of condensed-matter systems that are in equilibrium and using weakly interacting probes. Both conditions fail in most of the cases described below. Here, the excitation of samples is typically strong, and the sampled probe volume will typically not be in an equilibrium state but develop rather dynamically. Also, the interaction of the sample with the probe pulse must be considered non-negligible due to its intensity. However, many of the applications described below treat the excitation and the probing as small distortions, allowing us to assume quasi-equilibrium conditions and apply modified condensed-matter theories.

Three areas of condensed-matter applications are currently being considered for the HED instrument. In addition to investigations of condensed-matter properties following high excitation by OL or X-ray FEL pulses, the ultrashort and brilliant X-ray FEL radiation can also be used to probe the dynamically compressed matter instigated by nanosecond OL pulses. Another area of application is to probe the structure and dynamics of complex solids in very high pulsed magnetic fields.

Solid-matter properties following strong excitation

Possible examples for such studies are investigations of ultrafast phase transitions, like solid–solid transitions, melting or ablation. These transitions are often irreversible and can be initiated using either intense ultrashort OL or X-ray pulses. Intense and ultrashort excitation initially produces a highly non-equilibrium condition with varying excitation density. Interatomic forces, which create solids and determine many of their properties, can be substantially altered, leading to order-to-disorder solid–solid phase transitions.

Femtosecond time-resolved OL reflectivity measurements have provided insights into the electronic response of metals and semiconductors, but do not offer direct information on the nuclear response of a system. In contrast, ultrafast X-ray diffraction can provide atomic-scale spatial and temporal resolution. Static or dynamic structural studies down to ~ 100 ps resolution have been performed using synchrotron-based X-ray sources [4]. But low X-ray flux has prevented carrier-dependent studies of the interatomic potential. Single-shot structure determination with femtosecond X-ray diffraction experiments requires X-ray FEL radiation.

In the case of aluminium, the lattice stability is mostly unaffected by electronic excitation. Electron-photon scattering heats the lattice and results in thermal melting on the picosecond time scale. In contrast, the excitation of semiconductors weakens covalent bonding and softens the lattice [5]. For Peierls-distorted crystals like bismuth, the impulsive electronic excitation shifts the minimum of the potential energy surface and launches coherent, large-amplitude optical phonons, softening the interatomic potential [6,7]. In the case of gold, in contrast, strong electronic excitation reduces the screening of the attractive internuclear potential, resulting in a steepening of the phonon dispersion and hardening of the lattice [8,9]. Retardation of the thermal melting compared to classical nucleation theory was observed [4]. Structural dynamics of photo-excited solids, especially at sub-picosecond resolution, is still poorly understood, as the experimental tools used so far provide only incomplete insights. X-ray diffraction is a well-established tool offering atomic resolution. The applications described here require precisely synchronized, femtosecond-long, bright X-ray pulses like those provided by the European XFEL. As an alternative method, X-ray absorption near-edge spectroscopy (XANES) can be applied to probe short-range order and electronic structure disordering, as was recently tested at the Linac Coherent Light Source (LCLS) at SLAC National Accelerator Laboratory in Menlo Park, California [10].

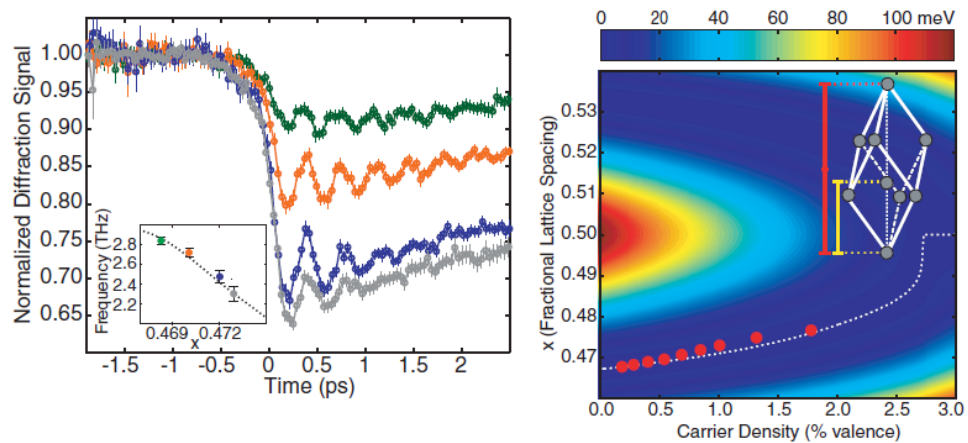


Figure 3-1. (Left) Bismuth (111) X-ray diffraction as a function of time delay between the optical excitation pulse and X-ray probe for excitation fluences of 0.7 (green), 1.2 (red), 1.7 (blue), and 2.3 mJ/cm^2 (gray). The inset displays the optical phonon frequency as a function of the normalized atomic equilibrium position along the body diagonal. (Right) Interatomic quasi-equilibrium position as a function of the percentage of valence electrons promoted into the conduction band. The red circles represent experiments. Figures taken from [7].

A related area is the investigation of materials during laser processing. Today, lasers are routinely used for materials processing and synthesis. In particular, very precise structuring can be achieved, as well as the synthesis of advanced materials that cannot be obtained by conventional techniques. In this context, ultrashort (femtosecond and picosecond) light pulses have demonstrated remarkable advantages. Surface and three-dimensional (3D) structuring, functionalization of materials down to the nanometre scale, pulsed laser deposition of smooth, particulate-free films, and tailored production of nanoparticles are just a few examples. Besides the importance of these processes for technological applications, investigating the interaction of intense ultrashort laser pulses with condensed matter is also a highly promising field from a fundamental physics viewpoint because it addresses important questions in phase transition physics and on the properties of materials at moderately high energy density.

Short-pulse laser irradiation represents a unique way of depositing energy into materials, allowing the realization of states of extreme electronic excitation and/or very high temperature and pressure, and the opportunity to

drive materials close to and beyond fundamental stability limits. As a consequence, structural changes and phase transitions can occur on very rapid time scales, and often along unusual, non-equilibrium pathways. The short X-ray pulses from the European XFEL will offer new possibilities to probe the structural evolution of materials under such strong excitation conditions. Examples of processes to be studied include non-equilibrium order–disorder transitions (solid–liquid, solid–plasma), laser ablation, nanoparticle formation, and structure formation at surfaces.

Solid matter in states of extreme pressure and density

The cores of large gaseous planets—such as Jupiter, Saturn, and many extrasolar planets—likely contain matter in the solid state at pressures approaching and greater than 1 TPa (10 Mbar). The nature of solids at such extreme pressures is basically unknown. Static high-pressure studies in the last two decades have successfully used synchrotron radiation installations and reached pressures up to 300–400 GPa and temperatures up to a few 1000 K. The major platforms here are diamond anvil cells (DAC), which allow compression of tiny pieces of matter to high pressures. To reach higher temperatures, pulse heating schemes have been successfully integrated into these setups. However, this technique has limitations in the maximum pressure and temperature that can be achieved. To extend the accessible pressure–temperature phase space—and thereby gain a platform for studying matter at conditions occurring in large planets and extrasolar planets larger than Earth, as well as to access new structures and materials—dynamic compression of matter using long (0.1 – few 10 ns) laser pulses is pursued at large laser installations. Using these platforms, pressures approaching TPa (10 Mbar) have been reached [11]. However, the laser platforms do not provide the finely collimated, narrow-bandwidth, ultrashort, coherent, and hard X-ray radiation that would allow the structural properties of dynamically compressed matter to be probed at high resolution.

Two methods of dynamic compression using nanosecond lasers can be distinguished. Shock compression uses laser pulses with widths of a few to tens of nanoseconds to transfer energy into matter. The excitation follows a Hugoniot curve generating high pressures and high temperatures (see Figure 3-2). Using this method will enable the investigation of dynamic and

irreversible processes and material properties at high temperatures and pressures. The excellent time and spatial resolution provided by the European XFEL will allow data to be obtained in unprecedented detail. Besides solid–solid phase transformations, multiphase fluid-melt processes will be of particular interest to study core formation processes and deep melts in planetary interiors. Elements and compounds of primary interest include Fe, Mg, Si, C, and their compounds. Related to this work, for many materials, Pickard et al. predicted that completely new structures would appear at high pressures [12]. For example, for Al, electride structures are predicted in the regime of 3.2 to 8.8 TPa (see Figure 3-3). However, shocks sometimes produce a significant temperature increase, inducing e.g. melting.

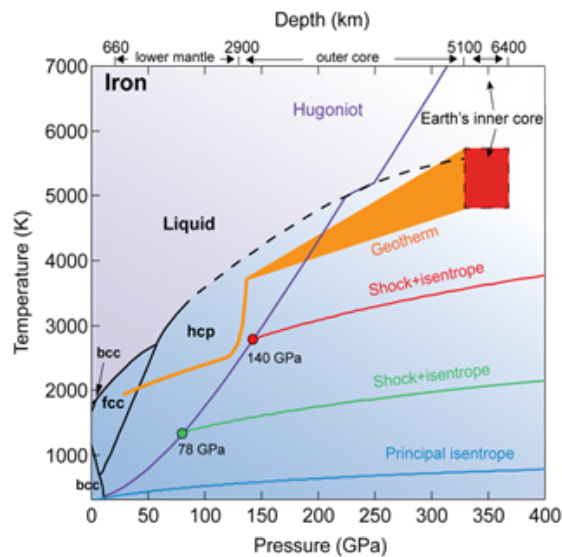


Figure 3-2. Schematic pressure–temperature phase diagram for Fe showing the principal Hugoniot and isentrope. By varying the start conditions through initial shocking, different isentropes can be accessed. The Earth geotherm is shown for comparison. Figure after T. Duffy (LLNL).

The second technique of isentropic or ramp compression uses nanosecond laser pulses with a slowly raising intensity and a steep drop at the end (see Figure 6-3 on page 109). The energy is thus coupled into matter over a longer period, avoiding the creation of shocks. Using this technique, it becomes possible to excite matter nearly along the isentropes, thereby generating very high pressures at relatively low temperatures (see Figure 3-2). Thus, materials present at extremely high pressures can be investigated in the solid state. This method will permit the study of thermodynamic states relevant to

material compositions present in planetary interiors such as giant planets or super-Earths. As an example, expected core pressures of exoplanets are shown in Figure 3-4 [13]. Elements and compounds of major interest here include H_2 , metals, metals in alloys, and molecular solids.

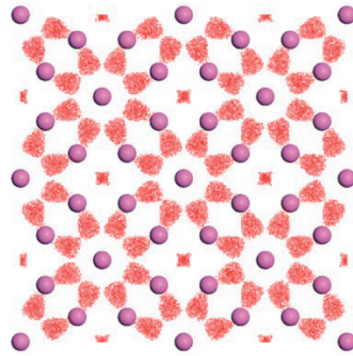


Figure 3-3 Structure representation for incommensurate host-guest electride phase of Al in the pressure range of 3.4 to 8.8 TPa [12]

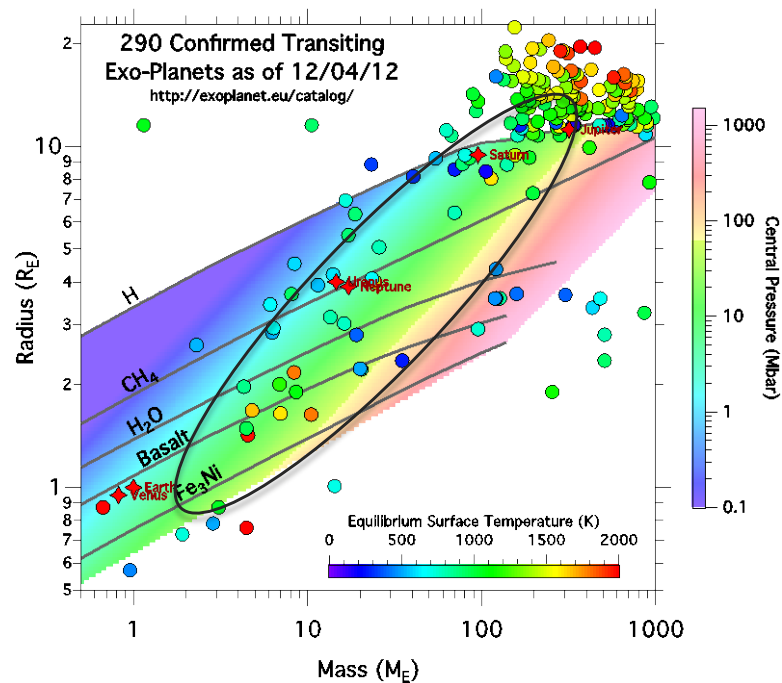


Figure 3-4. Occurrence and core pressure of exoplanets. The ellipsoid indicates planets with expected core pressures of $\sim 0.3\text{--}10$ TPa [13].

As regards instrumentation, a big challenge is the high-energy, nanosecond-duration optical laser (HE-OL) to drive ramp compression. To achieve pressures on the order of 100 GPa and excite a sizeable sample cross section, substantial energy must be provided in a single laser pulse. Estimates indicate that, with 1 kJ of energy, a pressure of nearly 3 TPa may be reached for Al using a 180 μm laser spot, 60 μm sample thickness, and a laser pulse duration of 5 ns (see also Figure 3-5) [14]. High accuracy in shaping the laser pulse, including the possibility to vary the pulse duration and thereby control the dynamics compression rate, will also be important. Frequency doubling to green laser light should be used at these pulse energies to suppress undesirable high-energy electron production. An effort will have to be made to develop samples for these studies. The aim to use high repetition rates (i.e. 1–10 Hz) requires replacing the samples at high rates, e.g. by moving to a fresh spot on a foil sample. In all likelihood, one will have to reduce the complexity of the sample structure. Currently used are layered samples, which often have a different composition in spatially separated areas. Such essentially 3D samples might need to be reduced to 2D samples that can be produced by coating techniques.

The excited matter will be studied using a variety of X-ray techniques. X-ray diffraction (XRD) allows studies of the geometric structure of solid and liquid phases, X-ray absorption spectroscopy (XAS) can reveal information about electronic structure, electron temperature, compression, and local order. Inelastic X-ray scattering (IXS) can be used to determine electron, and possibly, ion temperature distributions. And finally, X-ray imaging (XI) techniques may be used to observe and follow density changes along the shock propagation.

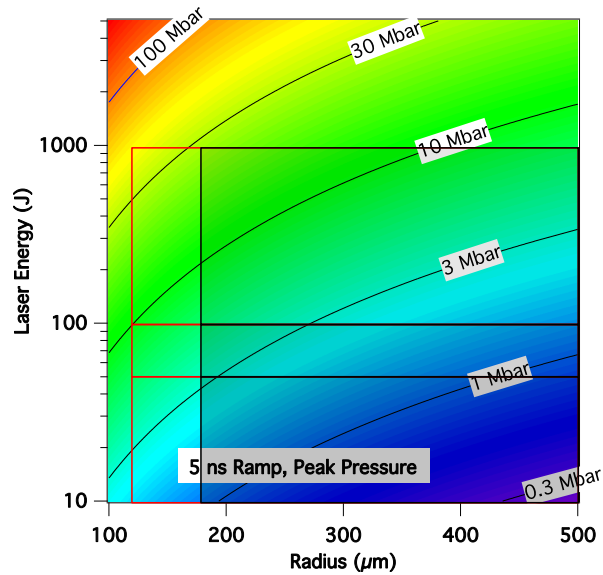


Figure 3-5. Calculated pressures for 5 ns dynamic compression as a function of spot radius and pulse energy. Red lines indicate the accessible region for shock compression ($R > 2d$). The grey shaded area indicates the accessible region for ramp compression ($R > 3d$) for sample thickness d [14].

Magnetism in complex solids

Magnetic fields generate an important phase space element for matter. Electrons carry a magnetic moment, and every material is therefore influenced by magnetic fields. Magnetic fields also affect the structure of materials. Yet a majority of high magnetic field experiments investigate macroscopic properties, while microscopic structure changes are difficult to observe because there are usually no high-field magnet devices available at pulsed, intense, and brilliant X-ray sources. Very high magnetic fields in excess of ~ 30 T can best be achieved using pulsing magnets. These pulses have durations on the order of a few 100 μs up to tens of milliseconds and therefore nicely match the pulse train structure of the European XFEL. The X-ray pulses allow an improved probing of matter in extreme magnetic fields by exploiting the large number of X-ray photons in a single pulse. In addition, sequences of pulses can be employed to follow the response of the sample to the ramping of the pulsed magnetic field.

As an example, the investigation of structural properties of the pyrochlore compound $\text{Tb}_2\text{Ti}_2\text{O}_7$ in response to a pulsed magnetic field is shown in

Figure 3-6. This compound shows a restoration of structural symmetry in intermediate fields and a structural phase transition above 25 T. In this particular experiment, a miniature coil with pulse duration of 1 ms and a peak field of up to 30 T was used [15]. Intensity was recorded with a Si strip detector with 50 μ s readout time. Figure 3-6 shows the field dependence of the (006) Bragg reflection. One observes a very low intensity at ambient field and vanishing of the reflection above an applied field of 8 T. The systematic absence of the (006) reflection originates in a four-fold screw axis, which is violated at ambient and low fields but restored for high magnetic fields, as shown by this measurement. At the European XFEL, similar experiments can be performed using single shots, allowing much more detail about the structural dynamics to be obtained, e.g. as a function of temperature.

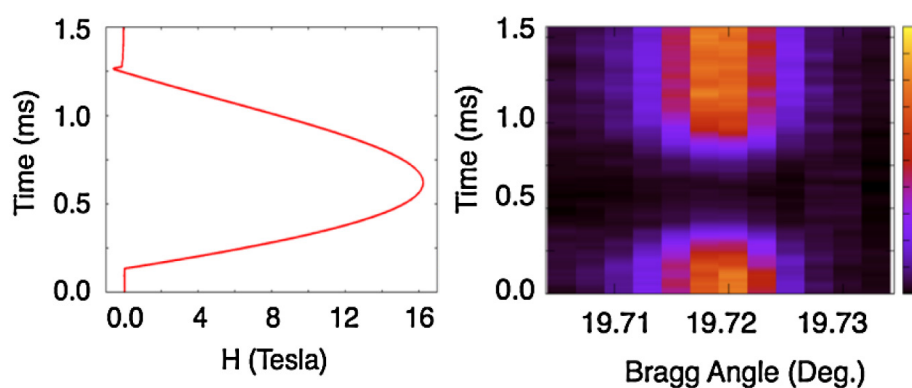


Figure 3-6. (Left) Magnetic-field history. (Right) Variation of the (006) intensity as a function of Bragg angle and time. [15]

A second example is the investigation of the successive metamagnetic transitions of TbB_4 in magnetic fields up to 30 T [16]. TbB_4 shows an intriguing multistep magnetization curve as a function of the field applied along the c -axis [17]. Resonant magnetic X-ray scattering at the Tb L_{III} absorption edge shows a huge enhancement of the magnetic signal. A pulsed magnetic field with 0.6 ms pulse duration was applied and the intensity was measured for increasing and decreasing fields. In Figure 3-7, measurements with and without polarization analysis are shown as a function of magnetic field strength. The polarization analysis enables the determination of the nature and direction of the magnetic moments. A decrease in intensity at 16 T indicates a ferromagnetic alignment of spins, coinciding with the start of an increase in magnetization. The synchrotron results shown here require

several tens of magnetic pulses to obtain reasonable statistics for a single data point, equivalent to several hours of measurement time. With the statistics of the experiment, which are described in [16], details of the field dependence cannot be resolved. The much higher X-ray intensity at the European XFEL will allow improved statistics per data point to be obtained in a single pulse, and therefore temperature and scattering angle to be varied in reasonable time, thus providing much more detailed information about the magnetic structure.

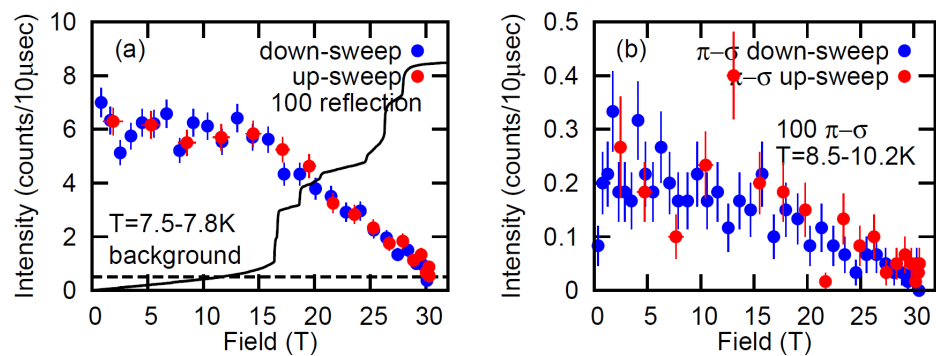


Figure 3-7. Field dependence of the peak intensity of the (100) magnetic reflection without polarization analysis (left) and with polarization analysis in the π - σ channel (right). In the left figure, the magnetization is also shown [16].

For the instrumentation, two types of high-field devices could be used. Mini-coil devices can reach fields of up to 50 T for very short times (< 0.5 ms) and for a reduced sample volume (few mm^3). Large-coil devices can reach very high fields above 50 T with pulse durations of a few to several 10 ms and sample volumes of several 100 mm^3 . While the large coils can be pulsed only at rates of several mHz, the mini-coil devices reach 0.1 Hz. The science applications typically require low-temperature cryostats (2–8 K). Optical laser excitation of the samples inside the magnetic field is not foreseen at present. The proper implementation of the cryostats and pulsed magnetic field devices needs to be developed.

Primary X-ray techniques to study geometric and electronic structures of matter in high magnetic fields are diffraction and absorption spectroscopy. Diffraction from single crystals or powder samples could be done resonantly and non-resonantly to investigate structural properties. Absorption

spectroscopy allows the investigation of the electronic structure, and the magnetic-dichroism technique enables the separation of magnetic states from the rest of the electrons. Chapter 4, “X-ray techniques and requirements”, describes the requirements for the X-ray beam with respect to photon energies, bandwidth, and circular polarization that would enable these techniques at the HED instrument.

3.2 Solid-density plasmas

A second large area of application is solid-density plasmas. Plasmas are macroscopically neutral gases of ionized and neutral particles. While a majority of the universe is in a plasma state, on Earth, plasmas are instable. For the research considered here, we concentrate on dense plasmas, which, in general, cannot be studied using visible light, thus requiring the use of X-rays. When cold, condensed matter is heated to become a plasma, as is done technologically in a variety of processes, the matter transits through an intermediate regime in which both condensed-matter and plasma theories need to be applied. For example, correlation, which is very important for cold solids, still exists in these plasmas and has important consequences. At the same time, ionization already occurs, and therefore recombination and collisions have to be considered. To date, no general theory exists for this intermediate regime, which is called warm dense matter (WDM). Higher-excited dense plasmas are called hot dense matter (HDM) and can also exhibit very complex behaviour.

Three areas of solid-density plasma applications are distinguished below. The first is the creation of well-defined WDM states using intense and ultrashort X-ray FEL pulses. The investigation of WDM states is a second application area. And finally, the X-ray FEL pulses provide very good conditions to study highly excited solids following relativistic laser–plasma interactions initiated by high-intensity OL pulses.

Creation of WDM

WDM, which by its nature is a near solid-density state with finite temperature (≥ 1 eV), can be created by simply passing the European XFEL X-ray beam

through a sample that has a thickness on the order of the absorption length. The advantages of creating WDM using ultrafast X-ray pulses are the volume interaction with the sample and a well-defined photo-excitation process. The crucial experiment observables will be the sample temperatures, i.e. T_i and T_e , the ion–electron thermalization time, and the sample uniformity. Ideally, the sample will be heated uniformly, but, in reality, gradients are unavoidable. As a first measurement to be done, experimental confirmation of not-too-steep gradients is important to verify the conceptual idea that the later expansion of the heated sample would be isentropic. Following this expansion using delayed probe pulses, one could map out, in a unique fashion, a region of the WDM phase space in temperature, density, and pressure. This measurement and the obtained data are important because experimental data on high-pressure states at ≥ 0.1 TPa (1 Mbar), that is, off the principal Hugoniot, is difficult to obtain but is required to generate an equation of state (EOS) for the experimentally attained conditions that mimic WDM systems existing in nature. As of now, two experiments have been performed to this end: one on Al at the Free-Electron Laser in Hamburg (FLASH) in Germany [18] and one on Ag at LCLS [19]. Both of these experiments provided proof-of-principle results, but neither led to the next step, which is to measure the expansion and the uniformity. Indeed, the FLASH experiment turned out to be extremely well-suited to create a uniform sample, as saturation of the energy deposition was achieved, which means that the uniformity was exceedingly high and there would be no gradients. In this case, the only equilibration that needs to occur is between the excited electron subsystem and the cold ions. For hard X-rays, absorption saturation will be more difficult to achieve due to the reduced Auger lifetimes and the more complex valence shell structures of higher-Z elements. Therefore, the possibility to employ this effect will have to be simulated for various materials.

Having verified uniform heating, the next issue that needs to be addressed is the ion–electron energy transfer rate. There are several ways to study this state of matter (see also Figure 3-8).

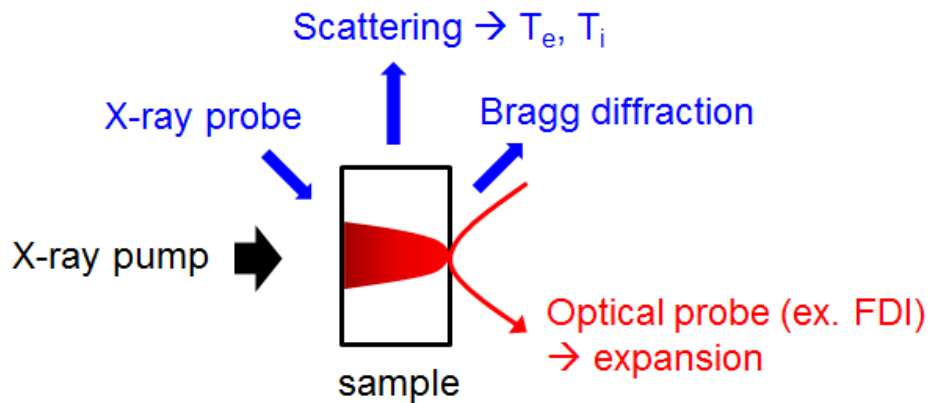


Figure 3-8. Schematic experiment setup to create and probe WDM

First, we could use inelastic X-ray scattering to observe the signal in the collective regime for both the ion and electron features. This will inform about the two temperatures at the same time. This measurement requires high spectral resolution to be able to observe the ion feature, which is separated from the Rayleigh peak by approximately the ion plasma frequency, which is proportional to $\sim (4\pi(n_e+n_i)e^2/m_i)^{1/2}$. This means that the ion plasma feature will get closer to the Rayleigh peak as the atomic number of the ion increases. Thus, this method, when used as a proof of principle, would be restricted to low-Z ions, or extreme resolutions would be required. The second way to measure ion heating is to perform diffraction experiments that can follow the nuclei disorder process and should allow information about the ion motion to be obtained. This is not a direct measure of the ion–electron equilibration, but can indirectly be used to determine the ion heating. Third, experiments have been proposed to look at the change of near-edge absorption. These experiments would discern the heating of the ions by comparison of molecular dynamics simulations of the heated sample. The point of such experiments is to determine whether the isochorically heated sample with a spatially uniform energy density, albeit not in equilibrium due to the electron–ion temperature difference directly after excitation, can equilibrate into a local thermodynamic equilibrium (LTE) state before hydrodynamic expansion of the sample creates gradients that turn the system into a non-LTE state. If the expansion occurs only after equilibrium has been established, then the method of creating a WDM sample using the intense

X-ray beam would be validated, allowing EOS information to be obtained in this important part of the pressure–temperature phase space.

Given that the above-mentioned condition is fulfilled, a new experiment platform for WDM generation would be validated, which would allow a wide range of applications to measure EOS data for various systems and conditions. The experiment results will provide a critical input to theory development and simulations of the transition regime where solids turn into plasmas.

Investigation of WDM and HDM

Investigation of WDM or HDM states created by X-ray or OL pulses will allow open problems in understanding these systems to be solved and better theories and models to be developed. Using X-ray spectroscopy techniques, one can probe plasma creation and the interaction of the atoms and ions within the plasma. The spectroscopic information derived from the emission by the plasma provides diagnostic information about the plasma itself. In addition, for high-density plasmas, one can explore laser pump–probe techniques that have been used previously to probe neutral and singly ionized systems to measure line shapes, observe radiation redistribution, and determine kinetic processes. Using optical probes, such as Fourier domain interferometers (FDI, Section 6.2), one can measure the front and back expansion velocity of critical-density surfaces, which in turn is a measure of the temperature of the electrons heated by the X-ray beam (see Figure 3-8).

Relativistic laser–plasma interaction

The fundamental interaction of ultrahigh-intensity (UHI, beyond 10^{18} W/cm²) short-pulse lasers with solid-density matter is an extremely complex phenomenon that presents many fundamental challenges. At the same time, its understanding is important for many research applications, such as generating secondary particle beams (ions, electrons, positrons, and neutrons) and intense ultrashort-radiation pulses (THz, high-order harmonics, and hard bremsstrahlung), studying magnetized-plasma phenomena of astrophysical interest (e.g. reconnection), or exploring the fast-ignition concept for inertial confinement fusion.

An essential aspect in each of these areas is the absorption of the laser energy into electrons towards relativistic velocities at the critical-density surface, and their transport into and through the solid-density plasma. Near the laser focus, the current density of the relativistic electrons can exceed 10^{13} A/cm², combined with extreme self-generated magnetic- and charge-separation electric fields, up to 10^5 T and 10^{14} V/m, respectively. Collisional and field ionization provide the compensating return currents, whose complicated dynamics depends self-consistently on the local ionization state, effective temperature, and resistivity (collisionality) of the plasma. Present state-of-the-art particle-in-cell simulations predict a variety of rapidly growing plasma instabilities, which cause spatial and temporal non-uniformities in the forward and return current, as well as in the field generation.

A detailed understanding of each of these phenomena, together with their interactions and far from equilibrium, is a grand challenge of modern-day plasma physics. But many of the most fundamental aspects, such as the ionization state and the collision frequency in dense plasma, are not well described by presently available theory and simulation. Probing inside the solid-density plasma with X-rays will open entirely new ways to directly observe these extreme conditions, and will provide fundamental new data for developing improved models, as well as validate or falsify present treatments. Key observables include the local electron density, current density, quasi-static magnetic fields, and ionization state, as well as the growth rate of the various perturbations and instabilities. Coherent imaging techniques can be used to measure density perturbations or local ionization states by using resonant coherent imaging when the X-ray beam is tuned to a bound-bound resonance of a particular charge state. Faraday rotation imaging with crossed polarizers would be sensitive to quasi-static magnetic fields around electron filaments or at material interfaces.

The relevant spatial scales range from the order of the OL wavelength ($\sim 1 \mu\text{m}$) to the plasma oscillation in the solid-density plasma (20–30 nm). These match well with small-angle X-ray scattering (SAXS) with a Q range of 0.006 nm^{-1} to 0.3 nm^{-1} . Relevant time scales range from a few femtoseconds (for electron–electron correlations or ionization dynamics) to several picoseconds (ion motion or field relaxation). The latter can be addressed by using laser pump – X-ray probe techniques, and the former requires non-collinear split-and-delay techniques of the X-ray probe pulse, with variable delays down to a few femtoseconds.

Figure 3-9 illustrates a typical experiment setup where SAXS is used to probe a target foil. In this particular example, enhanced heating of buried layers is investigated, which is predicted to arise from collisional shocks produced inside the solid-density target at the material interfaces [20]. This effect is predicted to arise from the rapid heating of the bulk electrons to a few kiloelectronvolts by the return current, which is in turn driven by the forward-directed relativistic electron current. The gradient in electron density at the material interface produces an ambipolar electric field of several 10^{12} V/m , which accelerates ions at the interface from regions of high electron density towards lower electron density. The high ion–ion collision frequency rapidly thermalizes the directed ion energy at a rate substantially exceeding ion heating by the direct electron–ion collisional coupling. The process proceeds, resembling a collisional shock driven by the thermal pressure gradients, for the duration of the relativistic laser-induced return currents.

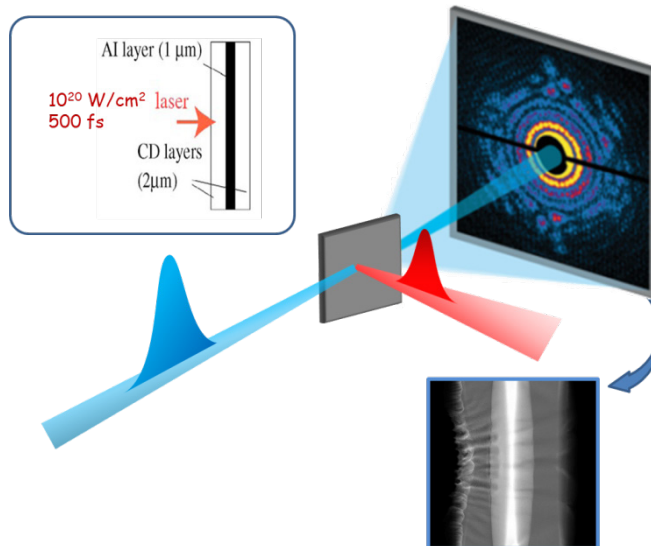


Figure 3-9. Schematic of SAXS coherent imaging of filamentation and hole-boring instabilities or internal interface shocks in relativistic laser-driven layered target foils. The relativistic OL pulse is indicated in red, the X-ray beam in blue. The upper left inset shows the target and laser parameters. In certain cases, iterative phase retrieval can be used to extract the real-space image. As an illustration, the lower right inset shows a 2D PIC simulation for these parameters.

SAXS is used to measure the electron density correlations, which allow the interface expansion to be tracked, as well as the several types of transport instabilities that arise at these relativistic laser intensities. The optical laser is oriented perpendicular to the X-ray beam, with the target set at an oblique angle, in order to preferentially view the interface expansion, as well as the transverse development of the filamentation, hole-boring, and channelling instabilities. Iterative phase retrieval, or X-ray holography, can in principle be used to reconstruct the real-space image—a highly idealized case is illustrated in Figure 3-10 (ideal 2D)—but blurring is expected from the integration over the sample depth along the X-ray line of sight. However, the essential physics content, namely the dynamics of the electron density correlations, is directly measured in the Q-space scattering image. Sampling over many shots with differing delay, or with non-collinear splitting of the probe beam, allows the mode structure, and the growth rates as a function of the scattering vector, to be measured for the relevant perturbations.

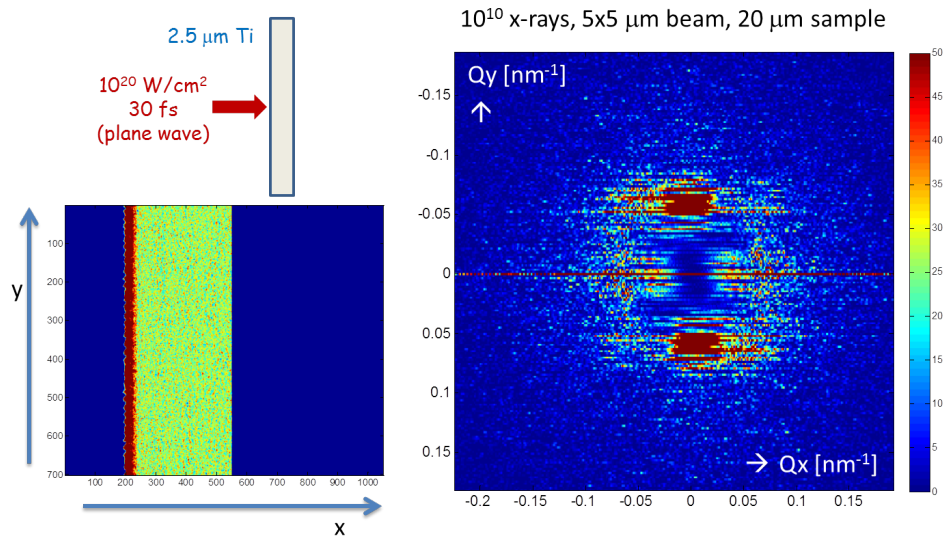


Figure 3-10. Simulation of SAXS experiment measuring electron density correlation transients in a solid-density Ti target, driven at a laser intensity of 10^{20} W/cm². An idealized 2D geometry is assumed, and a large signal size is expected, sufficient to identify principal features occurring at the plasma frequency. This suggests that as few as 10^{10} X-ray photons per pulse are sufficient, which should allow time-resolved studies with few-femtosecond pulses.

By using a collinear geometry (OL and X-ray beam along the same axis), one may gain improved resolution for the individual density channels and observe, as a function of time, their propagation into the target foil. The spatial scale of the fine structures in this example are on the order of > 100 nm.

The intensity of the SAXS signals is largely sufficient to obtain useful images with a single shot, with as few as 10^{10} incident X-ray photons. This is summarized in Figure 3-10, which shows a predicted SAXS scattering signal for an idealized experiment (2D) measuring electron fluctuations inside of a solid-density Ti target driven by a 10^{20} W/cm², 30 fs duration OL pulse. Particle-in-cell simulations show the presence of high-frequency oscillations inside of the bulk, which correspond to the solid-density electron plasma frequency. In addition, a compressed front surface that shows similar transverse periodic features is predicted for these parameters. Both of these are clearly apparent in the simulated SAXS image, where a 20 μ m depth is assumed, for 10^{10} photons incident in a 5 μ m x 5 μ m beam. The false-colour image shows detected photons per pixel, assuming an X-ray CCD with 13 μ m

pixel size, positioned at 2 m. The predicted signal intensity is sufficient for phase retrieval image reconstruction, as well as for X-ray photon correlation spectroscopy (XPCS). Weaker features can be examined with higher incident flux, but it is important to note that 10^{10} photons should be available in the short-pulse operation of the European XFEL, suggesting that SAXS measurements with pump–probe and split-and-delay techniques should be feasible.

Measuring the ionization states

One additional prospect to study the electron filamentation at very early times, before the ion motion leads to significant density fluctuations, is to measure instead the local ionization charge state in the solid-density plasma. Particle-in-cell simulations suggest that, during the first several 10 fs of the laser pulse, field ionization is a primary contributor to the reservoir of free electrons that constitute the return current, followed by the onset of electrothermal instabilities that involve localized heating and ionization in the resistive channels, which subsequently seed the channel formation visible in Figure 3-9. Separating free from bound electron scattering is not possible at small angles. However, as the ionization state increases within such filaments, there is a local shift of the absorption edges (XANES), and as outer shells are ionized, bound–bound excitations become possible, for example at $K\alpha$ and $K\beta$ transition energies. For high-charge states, the atomic screening of the inner shells is reduced and, for example, the $K\alpha$ transition shifts to higher energy. By tuning the X-ray beam energy to a specific value, one can spatially image the local change in X-ray absorption. This can be done by direct point projection imaging, or with higher spatial resolution using coherent diffractive imaging. By tuning above an edge, the cold target is absorbing, and one sees a reduction in absorption for the ionization regions. By tuning to a bound–bound transition, e.g. $K\beta$, the cold target is initially transmissive, and one sees an increased absorption as the $n = 3$ shell becomes ionized. By tuning in the $K\alpha$ range to a specific charge state satellite, one may track the evolution of a single ion charge state. This is summarized in Figure 3-11, for a simulated measurement of the 20+ charge state in Cu. A 2 μm thick Cu foil is driven with a 10^{21} W/cm², 30 fs long OL pulse. The SAXS signal intensity depends on the optical depth along the line of sight, and therefore on both the

feature size and the relative fraction of the specific charge state in the feature volume. For well-defined filaments, the approximate magnitude is similar to that from the electron plasma wave fluctuations considered in Figure 3-10, which is of the order of 1% at solid density.

At present, treating ionization in solid-density plasma simulations is very problematic. The existing ionization models tend to be valid only near equilibrium, and do not treat correlation effects in dense plasma well. The fundamental mechanisms of field and collisional ionization are treated approximately, and do at present not properly include recombination processes. This is an extremely active field in WDM physics, as noted above in “Investigation of WDM” on page 29. The use of coherent X-ray probing of the ionization dynamics and charge state evolution will provide valuable new data.

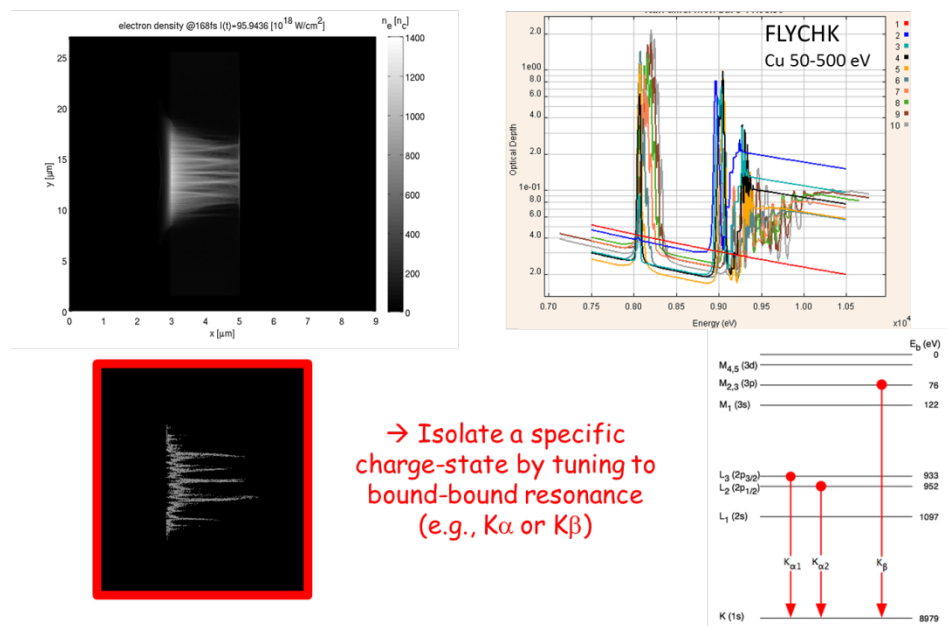


Figure 3-11. Simulation of charge state-selective SAXS experiment

3.3 Quantum states of matter

The availability in the future of ultra-intense lasers at the European XFEL (from 100 TW to the PW regime) will enable the experimental study of matter in extreme electric and electromagnetic fields. This includes possibilities to probe the fundamental nature of the quantum electrodynamics (QED) vacuum state in strong fields, and even to study systems at extreme acceleration, which by the equivalence principle can be related to phenomena in general relativity. New opportunities to test fundamental predictions of strong-field QED and to search for new effects have been discussed in the literature [21, 22, 23]. Of particular interest is to gain insight into the strong-field effects that become important above the Schwinger field of 1.3×10^{18} V/m. In these extreme electric fields, the virtual electron–positron pairs that make up the QED vacuum state can be accelerated to the mass shell and become real, resulting in the creation of positrons and electrons in a process closely related to the Klein paradox [24]. Such strong electric fields can be produced for extremely short times (10^{-21} s) in heavy-ion collisions, or in the Lorentz-boosted rest frame of very high energy electrons propagating in a laser field or channelling through a crystal lattice. In these cases, the observed positron production can be described by one or a few energetic virtual photons of the order of the electron rest mass. New effects are predicted in extremely strong laser fields, where the strong-field interaction is fully non-perturbative and must be described by very high order multiphoton processes. For example, the vacuum polarization correction in perturbative QED is modified by the multiphoton interaction with the real laser field in the virtual-electron propagator.

The Schwinger field corresponds to a laser intensity about six orders of magnitude beyond the current technology. But even well below the Schwinger limit, at fields achievable with the planned PW-class upgrade to the UHI-OL laser, and making use of the unique hard X-ray beam intensity of the European XFEL, the fundamental nature of the non-perturbative vacuum polarization can be probed. Here, the term “vacuum polarization” more precisely means a change of the dielectric and magnetic susceptibilities due to an external electromagnetic field. A prominent example is the propagation

of a probe photon (X-ray beam) through the electromagnetic (quantum) vacuum. Similar to the propagation through a given material (e.g. a plasma), the probe photon may experience (i) dispersive modifications and changed polarization properties and (ii) absorptive effects, e.g. decay into an electron–positron pair. These effects are linked by dispersion relations cutting rules and the optical theorem. A variety of exciting possibilities for possible QED experiments at the European XFEL were discussed at a workshop in Dresden in fall 2011, and it was suggested that the most accessible experiment at the European XFEL would be the “vacuum birefringence” (see Figure 3-12).

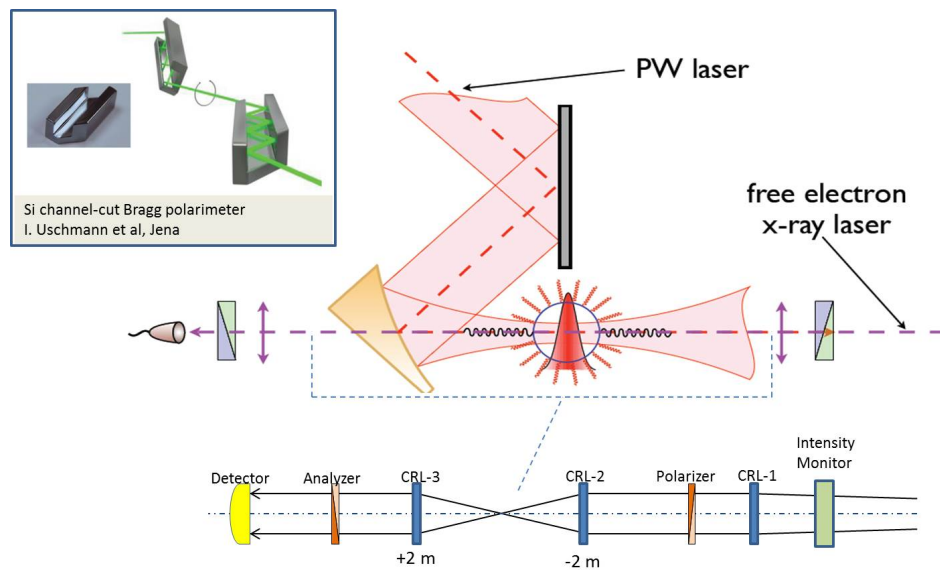


Figure 3-12. Schematic of vacuum birefringence experiment. The PW-class OL beam propagates through focus from left to right, counter to the European XFEL beam (right to left). Silicon channel-cut Bragg crystal polarimeters (inset) are used in crossed polarizer–analyser geometry. Beryllium compound refractive lenses (CRL) are used to ensure large (200 μm) parallel beams at the Si polarimeters, with a tight focus (< 200 nm diameter) to overlap the OL laser focus ($\sim 2 \mu\text{m}$).

Vacuum birefringence

At laser intensities approaching 10^{22} W/cm^2 , the vacuum may become sufficiently polarized that its refractive index will change in one direction only. Much like a calcite crystal, this will cause the polarization of an X-ray probing beam to rotate as it passes through the region of high field. If the X-ray polarization is oriented initially at 45° to the laser polarization, a resulting ellipticity is observed, which can be detected by the transmission through a

crossed X-ray polarizer–analyser system that is set for full extinction of the unmodified X-ray probe. The small transmitted intensity fraction is given by the square of the phase rotation, δ^2 , where

$$\delta = 2\pi \frac{d}{\lambda_x} \left[\frac{I_L}{10^{21}} \right] (7 \times 10^{-13})$$

with I_L the laser intensity in W/cm^2 , d the length of the high-field region, and λ_x the X-ray wavelength [25]. The experiment setup is shown schematically in Figure 3-12.

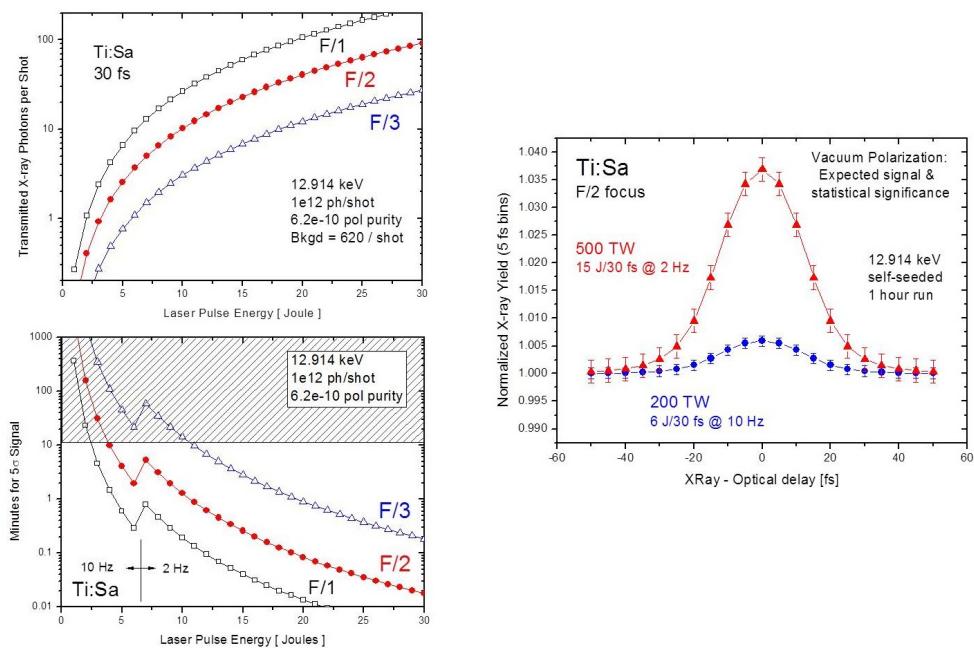


Figure 3-13. (Left) Predicted signal (top) and measurement time (bottom) required per point to obtain a 5σ significant measurement of the birefringence signal, as a function of the OL pulse energy. (Right) Predicted experiment sensitivity (statistical counting errors) with a 12.914 keV, self-seeded X-ray beam of 10^{12} photons per shot, and a one-hour experiment run scanning over an X-ray–OL delay of -60 fs to +60 fs. Predictions are shown for Ti:sapphire lasers of 200 TW at 10 Hz (blue), or 500 TW at 2 Hz (red), focused to diffraction limit with f/2 optics.

Recent advances in Si channel-cut polarimeters by Uschmann et al. at Friedrich-Schiller-Universität Jena, Germany [26] have achieved a polarization sensitivity of 6.2×10^{-10} for 12.914 keV X-rays for a Si(800) polarimeter using a six-bounce geometry. This implies a “background” signal of 620 transmitted photons per shot, above which one must search for the birefringence signal of only a few photons per shot. This requires signal averaging, and an intensity monitor of the incident X-ray beam of better than 1% per shot.

Several challenges remain to realize this experiment at the European XFEL. These include the stability of the spatial overlap, the quality of the tightly focused ($f/2$) ultra-intense laser, and the stability of the CRL Be lens system. The $f/2$ OL focusing implies a $\sim 2 \mu\text{m}$ laser spot diameter. The X-ray beam is focused to about 200 nm diameter. Particularly noteworthy is the effect of any impurities or non-uniformities of the CRL lenses on the X-ray polarization purity, which although expected to be small, has to date only be confirmed experimentally to be smaller than about 1%. Tests using synchrotron beams of the entire X-ray CRL system plus polarizer setup will be required to establish the ultimate feasibility of this approach. An alternative using fully reflective X-ray optics could be considered, but may be spatially prohibitive.

Reference [27] discusses additional interesting prospects, for example the promising opportunity of probing the quantum vacuum birefringence by phase contrast Fourier imaging. Reference [28] reports an enhancement of vacuum polarization effects in a cold collisional plasma. A detailed feasibility analysis of these effects is required to assess their ultimate viability for possible experiments at the European XFEL.

3.4 Summary of science requirements

The application areas outlined above and their observables can be realized using a variety of X-ray techniques. In general, each entails a number of possible realizations. In the sections above, the specific parameters and the respective experimental observables have been investigated for a number of cases. Table 3-1 provides a rough overview of the application areas and their respective major experimental techniques. These techniques and their requirements are discussed in more detail in Chapter 4, “X-ray techniques and requirements”. As can be seen from Table 3-1, a relatively large number of X-ray techniques have been proposed, corresponding to the widespread applications to be fielded at the HED instrument. As we will see in the following chapters, this implies a high flexibility, which is one of the major challenges in the realization of the HED instrument.

Table 3-1. Overview of science areas and applications with respective suggestion of major experimental techniques to be implemented at the HED instrument. (IA: interaction, X: X-ray FEL, OL: optical laser, HFM: high-field magnet, S&D: X-ray split and delay, (R)XRD: (resonant) X-ray diffraction, SAXS: small-angle scattering, XAS: X-ray absorption, IXS: inelastic X-ray scattering, XCD: X-ray circular dichroism, XES: emission spectroscopy, XPA: X-ray polarization analysis)

Science area	Application	Pump	Probe	X-ray	OL
Condensed matter at extreme excitation	IA of intense X-ray pulse; damage; X-ray driven processes	X	X	S&D, XRD, SAXS, imaging	None
		X	OL / other		Microscopy
	Solid-matter properties following strong excitation	OL	X	XRD, SAXS, XAS, imaging	fs pump
	Solid matter in states of extreme pressure and density	OL	X & OL	XRD, XAS, IXS, imaging	ns & fs pump; VISAR, FDI
	Magnetism in complex solids	HFM	X	(R)XRD, XAS, XCD	None
Solid-density plasmas	Creation of WDM	X	X & OL	S&D, XRD, XAS, IXS, imaging	FDI
	Investigation of WDM	X	X & OL	S&D, XRD, XAS, IXS, XES	FDI
		OL	X & OL	XRD, XAS, IXS, XES	fs pump; FDI
	Hot dense matter	OL & X	-	XES	ns & fs pump
		OL & X	X	S&D, XES	ns & fs pump
	Relativistic laser-plasma interaction	OL	X	SAXS, XPCS imaging	UHI pump
Quantum states	Vacuum birefringence	OL	X	XPA	UHI pump

4 X-ray techniques and requirements

This chapter provides an overview of the various techniques to be applied at the HED instrument in order to achieve the scientific goals introduced in Chapter 3, “Scientific objectives”. Only experimental techniques employing the X-ray FEL beam for either pumping or probing the sample system will be considered, as experiments that do not use the X-ray FEL beam can be carried out at other laser facilities.

4.1 Pump–probe experiments

The majority of experiments are expected to employ a first excitation (pump) pulse and a second probe pulse. One or both of these will be an X-ray FEL pulse. An important parameter of pump–probe experiments is the definition and well-controlled adjustment of the delay between the pump pulse and the probe pulse. The HED instrument has the particularity that different sources (X-ray, OLs) may be used. This adds the complexity of having to stabilize the delay between these two independently generated pulses. The systems that are to be employed to stabilize the delay and monitor its value are described in Section 6.8, “Laser synchronization and diagnostics”.

The requirements for the delay between pump and probe pulses originate in the scientific questions to be investigated in the experiments and the physical processes in the sample. The duration of the X-ray or OL pulses used in the experiments is typically shorter than 100 fs. Studying electronic excitation and relaxation processes requires very high time resolution of one up to tens of femtoseconds. Following these processes will be extremely challenging due to the required time resolution. Electron–ion equilibration depends strongly on the specific system and typically takes place in the time frame from 100 fs to several picoseconds, which can be studied in detail at the HED instrument.

The nuclear response of dense matter to excitation, that is, compression or expansion, occurs typically at time scales beyond single picoseconds and continues into the nanosecond regime.

The choice of pump and probe pulses in general follows the requirements posed by the respective scientific problem. Pump sources could be X-rays, an OL pulse, or a magnetic-field pulse. The X-ray pulses provide high penetration, direct interaction with electrons, sometimes even with specific states, ultrashort duration, and relatively high pulse energies (up to a few millijoule). The combined properties of these pulses enable matter to be excited in a unique fashion, leading to the generation of new states of matter. OL pulses can be very intense ($> 10^{18} \text{ Wcm}^{-2}$) or very energetic ($> 100 \text{ J}$) with specific ramp profiles. In addition, high-field pulsed magnets produce high field values ($> 30 \text{ T}$) that will be employed to excite samples into transient states to be studied using the unique properties of the X-ray beam.

For probing the excited state, a variety of OL and X-ray techniques may be employed. In addition to the experiment observables to be retrieved, the state and development of the sample system have to be monitored. This requirement, which is related to the complex processes caused by sample excitation, is usually not necessary in investigations of ground state phenomena performed at synchrotron sources and poses an additional constraint to instrumentation. Table 4-1 provides an overview of pump and probe schemes and the respective combination of techniques.

Table 4-1. Overview of X-ray and OL probing techniques to be applied for the various pump sources. (Key: XRD = X-ray diffraction, IXS = inelastic X-ray scattering, XAS = X-ray absorption, XCD = X-ray circular dichroism, XI = X-ray imaging, XPA = X-ray polarization analysis, SAXS = small-angle scattering, XES = emission spectroscopy.)

	X-ray techniques								OL techniques				
	XRD	IXS	XAS	XCD	XI	XPA	SAXS	XES	Interferometry	Microscopy	FDI	VISAR	Reflectivity
X-ray pumping	•	•	•		•			•	•	•	•		•
OL pumping	•	•	•		•	•	•	•	•		•	•	•
Pulsed B field	•		•	•									

4.2 X-ray excitation and pumping

X-ray excitation is expected to be employed both for *condensed matter in excited states* and *solid-density plasma* applications. This particular usage of the intense X-ray pulses is highly specific to the HED instrument, aiming at the investigation of excited, transient sample states. The particular difference of X-ray pulses and OL pulses is the much higher penetration power of X-rays and the direct interaction with the electron system of the sample. X-rays penetrate dense samples of millimetre thickness (see Table 4-2) and deposit their energy in the photon energy range of 3–8 keV, to a large extent by photoionization, following an exponential law.

Table 4-2. Attenuation length in μm for several X-ray photon energies in keV and selected elements. Data from the Center for X-Ray Optics (CRXO) at Lawrence Berkeley National Laboratory (LBNL) in California [29].

	3	5	8	10	15	25
Plastic	67	311	1315	2694	8707	25786
Diamond (C)	31	149	637	1309	4149	10985
Aluminium (Al)	4.7	20	77	151	500	2234
Iron (Fe)	2.3	9.4	4.1	7.5	22	97
Copper (Cu)	1.5	5.9	22	5.2	15	63
Silver (Ag)	1.9	1.3	4.5	8.4	26	103
Nickel (Ni)	1.6	6.4	23	5.4	16	67
Tungsten (W)	0.3	0.9	3.1	5.6	3.9	15

When selecting photon energies closely above element-specific absorption edges, energy will be absorbed through a well-defined electronic channel [30] and may lead to the depletion of these states [18]. In order to use FEL pulses to excite samples, it is generally necessary to provide the highest pulse energies possible and to have a well-defined and small (sub- μm to $\sim 10 \mu\text{m}$) focal spot. One experimental challenge is the observation of the heated volume with a decent signal-to-background level. The X-ray pulse duration must be selected so as to be able to observe the processes under study. In solids, the equilibration of the electronic system is very fast, and any investigation of the properties of ultrafast electronic processes requires using the shortest available X-ray pulses of few-femtosecond duration. For studies of the equilibration of the electron–ion system, pulse durations $< 100 \text{ fs}$ are sufficient. The radiation intensities achievable at the European XFEL will allow excitation of solids into the dense-plasma regime (see Table 5-3).

For probing the excited system, two possibilities exist. In a first approach, X-ray pulses can be split into two parts using an X-ray split and delay unit (SDU). Such a device offers the unique opportunity to use X-rays for probing X-ray–excited samples. Furthermore, the two X-ray pulses can be highly synchronized with respect to each other since they originate from the same source. The SDU is technically very challenging, and its usage puts boundary

conditions on the experimental realization. Due to the unique capabilities and the long R&D period of an X-ray SDU, it was already decided some time ago to develop a prototype. This device is currently under construction and will be installed at the HED instrument.

A second possibility is to use OL pulses to probe the X-ray-excited samples. While this technique allows high temporal resolution with high flexibility in setup, in general, OLs can provide only surface information due to poor penetration length. No direct information about bulk properties can be obtained. The OL community has therefore developed methods that use surface measurements to draw conclusions about bulk properties by applying models for the excited system. OL techniques have, for example, reached a high maturity regarding the time-dependent characterization of the state and development of macroscopic samples. These OL techniques will be applied in conjunction with X-ray techniques, thus providing a reference for OL-only investigations. Some typical OL probing techniques foreseen at the HED instrument are briefly described in Chapter 6, “Optical laser installations”. Some of the X-ray probing methods are described in the following section.

4.3 X-ray probing

Several X-ray techniques will be employed for probing the sample under study. X-rays interact with electrons, and the scattering can generally be described by the dependence on the structure factor $S(Q, \omega)$. Elastic scattering and diffraction techniques employ $\Delta\omega = 0$ and investigate the angle-dependent scattering to obtain the geometric atomic structure of electron density distributions. Inelastic scattering ($\Delta\omega \neq 0$) is used to investigate the properties of electrons and plasmons in the sample. Photon energy-dependent absorption allows the investigation of the electronic structure and temperature of the electron system. Coherence techniques, like imaging or correlation spectroscopy, can be employed to study mesoscale spatial structure or electron density fluctuations.

X-ray diffraction (XRD)

Using XRD, information about structural properties of the sample is obtained, and the level of information can be very widespread. For example, strain as a consequence of a shock or compression wave, melting, or the onset of a phase transformation may be studied by observation of single Bragg spots, while full structure refinement requires the collection of many Bragg spots. While single crystals will exhibit only one or few Bragg reflections for a specific configuration and the given bandwidth of the X-ray FEL radiation, powder samples (powder diffraction (PD)) will enable many reflections to be observed at once. Operating the X-ray in a specific optimized mode for increased bandwidth of up to a few percent will improve the sampling of Bragg reflections (Laue diffraction (LD)), but still only a few spots will be observable in a single data set.

By performing XRD near absorption edges, resonant XRD (RXRD) can increase the selectivity to the respective elements of the sample. Analysis of the polarization state of the reflected radiation allows information about magnetic structures to be obtained. Another powerful technique is diffraction from liquid or amorphous substances, sampling the Q dependence of elastic scattering ($S(Q)$) and thereby measuring the nearest-neighbour distances. Small-angle scattering (SAXS) provides information about structural order and dynamics on mesoscopic length scales (few nanometres).

The requirements for X-ray parameters posed by XRD techniques can vary widely, but a few general statements can be made. In general, XRD benefits from using the maximum possible photon energy, which provides higher penetration depths and compresses reflections in a smaller angle volume, thus facilitating the experiment setup. Exceptions entailing the selection of specific photon energies are resonant scattering and requirements to sample orientation while employing specific Bragg reflections. A bandwidth of 10^{-4} to 10^{-3} is ideal for single-crystal diffraction and powders, while LD, $S(Q)$, and SAXS will benefit from an increased bandwidth. A bandwidth of a few percent, as may be obtained using special operation modes of the X-ray FEL, is actually still very small for LD but fits the requirements of $S(Q)$ techniques rather well. The requirements to X-ray pulse energy, pulse duration, pump–probe delay, and beam spot size depend mostly on the scientific question and

the interaction of the beam with the sample. For hard X-rays, the Fourier limit of the bandwidth – pulse duration product becomes an issue only for extremely short pulses (< 10 fs) and/or high resolution ($< 10^{-4}$). Small foci and high photon numbers will lead to unwanted sample excitation, which may need to be considered. Since Bragg diffraction from single crystals and big crystallites is highly efficient and does not significantly change the collimation, an incident photon number as small as 10^6 per pulse could generate a severe danger of detector damage. PD and $S(Q)$ techniques distribute scattered photons in a much wider Q -space and will therefore benefit from higher photon numbers to obtain single-pulse scatter with high signal-to-background ratio. In PD, the crystallite size and orientation is a critical issue that needs to be analysed for each sample. In general, reflection from as many crystallites as possible is required. This leads to the requirements to use X-ray beam spot sizes much larger than the crystallite size. The use of 2D area detectors will be essential for the majority of these experiments in order to obtain as much information as possible from a single event. XRD techniques typically require high angular resolution for detection (small pixels or large distance).

X-ray absorption spectroscopy (XAS)

The measurement of X-ray absorption near edges allows the investigation of the electronic structure of the sample by probing if electrons can be absorbed into free electronic levels. While this is a well-known method to measure ground state electronic properties, e.g. in chemistry, the application to excited states of matter has only recently been recognized [31]. The electron distribution also depends on the temperature of the electronic system, and it is possible to determine the electron temperature from the absorption profile. Once the sample volume undergoes ionization and density modulation, e.g. by compression or expansion, the absorption edges will provide indications for such processes. In addition to these solid-density plasmas close to cold matter, the measurement of opacities of hot dense plasmas requires, in a similar fashion, to determine the photon energy–dependent absorption of X-rays.

XAS techniques need a certain photon energy band near the absorption edge of the sample elements. At the HED instrument, only edges in the regime of 3 keV to around 24 keV can be accessed. This allows investigation of the

K-edges of the elements Ca to Mo and of the L-edges of the elements Tc to Bi. The energy band to be probed should be of the order of 30–100 eV to obtain the so-called near-edge features, at least for the L-edges. A much wider energy band of up to a few 100 eV would allow the investigation of geometric structure by employing extended X-ray absorption fine structure techniques (EXAFS). While such measurements have been achieved at X-ray FELs by scanning the photon energy, this technique seems at present too demanding for the HED instrument, thereby limiting the use of techniques like EXAFS and opacity measurements. Other requirements—like X-ray pulse energy, duration, pump–probe delay, or X-ray beam spot size—follow from the specific implementation of the experiment. Typically, these experiments are performed in transmission mode, and the spectral distribution is measured before and after the sample. In order to achieve the required accuracy, very good normalization procedures need to be established.

Inelastic X-ray scattering (IXS)

Inelastic X-ray scattering has been implemented at high-brightness synchrotron radiation sources with great success. The possibility to study and observe lattice and electronic excitations, which was opened up by the X-ray source parameters paired with exquisite instrumentation, has had a large impact in condensed-matter and liquid physics. In addition, Compton scattering at higher momentum transfer could be done at much higher resolution than in previous experiments, allowing details of the electronic system to be studied. This type of X-ray method is sometimes called X-ray Thomson scattering (XRTS) in the plasma community, owing to the transfer of methodologies from the optical domain to the X-ray domain. Studying plasmas or highly excited matter using IXS techniques allows, in principle, the measurement of electron and ion temperature distributions, densities of the free electrons, and the ionization state [32].

Depending on the scientific problem, IXS can be applied to measure the properties of the electronic and/or the ionic system. Generally speaking, the experiment observable is the dynamic structure factor $S(Q, \omega)$ for the momentum transfer Q and the photon energy transfer $\omega = \omega_1 - \omega_0$. For elastic or quasi-elastic scattering ($\omega \sim 0$), $S(Q)$ corresponds to the observable of

liquid diffraction and provides structural order and correlations of the ionic system.

For IXS experiments, the critical requirement is the spectral resolution that needs to be provided for the incident X-ray beam and the measurement of the scattered X-rays. The required resolution depends on the problem under study. For electron distributions (temperature, density, and ionization), a resolution $\Delta E/E \sim 10^{-4}$ – 10^{-3} (~ 1 – 10 eV at 10 keV) will be sufficient, while for ionic distributions (temperature), a resolution of $\Delta E/E \sim 10^{-6}$ – 10^{-4} (~ 10 – 100 meV at 10 keV) will be needed. This extremely high resolution requires specific instrumentation, which has been developed over recent years for synchrotron radiation sources, but which will need to be mastered at X-ray FEL facilities. To measure the Q dependence of the dynamic scattering factor, the measurements need to be performed at various scattering angles θ . Typically, for IXS experiments, the photon energy is uncritical and can be selected according to instrumentation needs and optimization of count rates. Therefore, an IXS instrument could be defined for a specific photon energy.

X-ray imaging (XI)

X-ray imaging is a very powerful tool to determine the real-space and reciprocal-space structure of a sample. Resolutions of a few nanometres have been reached using direct imaging methods. For coherent diffraction imaging on single articles or embedded structures, again a few nanometres seem to be the best achievable resolution at present. This method has the potential to reach atomic resolution. However, at the HED instrument, a more modest approach to imaging is made. Using, in a first phase, mostly direct imaging methods employing absorption or phase contrast, the density modulations of plasma and solid samples can be investigated. In particular, phase contrast imaging using the transverse coherence properties is of interest, as it is sensitive to very small variations of the electron density or phase shift of the sample. Since the method works best for sharp edges or steep gradients, the challenges to overcome are fuzzy boundaries of plasmas due to OL beam profile or transport processes.

Resolution is usually limited by the X-ray detector used to image the transmitted or forward-scattered X-rays. A possibility to overcome this

resolution limit is to use diverging X-ray beams and place the detector at appropriate distances to fulfil optics criteria like Fresnel or Fraunhofer and to match resolution requirements. Using this technique, sub-micrometre resolution can be achieved, provided a focal spot much smaller than 1 μm is created from which the beam diverges. The field of view in these experiments is determined by the distance of the sample volume to the X-ray focus. Experiments may be resonant to enhance scattering at certain materials of embedded structures, but often optimization of the setup could be done for specific photon energies. Usually, a monochromatic beam ($\Delta E/E \sim 10^{-4}$) is used to avoid blurring of scattering features. Since most experiments will be single-shot illuminations, a high stability of the optical system (that is, the lens with respect to the sample) is not absolutely mandatory. However, a stabilized setup would allow proper characterization of the X-ray beam and the focal spots to be performed.

X-ray photon correlation spectroscopy (XPCS)

This technique determines dynamics of electron density fluctuations. At the HED instrument, XPCS may in particular be applied to electron density modulations in highly excited solids and plasmas. XPCS can be done in the forward direction or for large momentum transfer Q (large angle). Here, we consider mostly the forward direction, which is less demanding regarding X-ray parameters. The technical implementation is similar to SAXS, with the difference that XPCS has specific requirements to detector resolution. Since it is necessary to detect speckles, in general the spatial resolution of the X-ray detector has to be very small. Since the HED samples will typically have extended lateral size, the X-ray beam size defines the speckle size. Even for X-ray 2D detectors with the smallest available pixel size (charge-coupled devices, CCDs), the X-ray beam on the sample has to be very small (of the order of micrometres or below). Again, the experiment setup can be optimized for a certain photon energy.

X-ray emission spectroscopy (XES)

XES involves the spectrally resolved measurement of X-ray emission (fluorescence) following non-resonant excitation of the system using X-rays and is usually applied to investigate properties of the fluorescing electronic

state. Here, we extend the term to include self-emission of the sample in a plasma state. In particular experiments, it may even be possible to resonantly pump the plasma using an X-ray pulse of specific photon energy and to observe the change of spectral properties and intensity of the emitted radiation. Such experiments give insight into plasma dynamics and redistribution inside the plasma.

Since the emission does not depend directly on the incident X-ray beam, at least not in non-resonant experiments, the requirements affect the instrumentation more than the X-ray beam. If resonant excitation is considered, it is of course necessary to adjust and scan the photon energy precisely. In this case, the bandwidth too has to be narrow enough to observe the features under study.

4.4 Experiment geometries

For the layout of the experiment area, in particular with respect to shielding of the directed background radiation generated by the UHI-OL beams, as well as for a preliminary design of the interaction chambers, the geometry of the experiment is very important. For the applications described above, the overall geometry can be complex since several beams may be in operation at the same time. Two boundary conditions have to be considered for the geometry. First, the direction and position of the X-ray beam are nearly fixed in space. Thus, the location and orientation of the sample and of the OL beams have to be arranged with reference to the incident X-ray beam. Second, X-ray FEL radiation is fully polarized in the horizontal plane. Therefore, X-ray scattering in the horizontal plane depends as $I(\theta) \propto \cos^2(\theta)$ on the scattering angle θ between incident and scattered X-rays. This dependence leads to a complete suppression of X-ray scattering in the horizontal plane at exactly 90° and to a sizeable reduction of scattering power in the angular range of 60° to 120° . Studying X-ray scattering at arbitrary angles therefore requires using the vertical plane, while fluorescence and X-ray emission can profit from the suppression to improve signal-to-background levels.

The orientation of the sample with respect to the X-ray beam depends on the type of X-ray technique applied. The most important criterion for defining this geometry is the definition of the sample volume probed by the X-ray beam and the respective signal-to-background ratio. For single-crystal samples, the Bragg condition also needs to be fulfilled. In general, full flexibility of the sample orientation with respect to the incident X-ray beam is required.

For the optical laser beam exciting the sample, one can distinguish two major setups (Figure 4-1). It is assumed that, in general, the OL is oriented such that it hits the sample surface perpendicularly. The highest time resolution can be achieved in the collinear or near-collinear geometry, since the OL wavefront and the X-ray wavefront are lined up. Here, the X-ray beam probes a sample volume that is behind the surface area hit by the OL pulse. While this geometry allows the minimization or imaging of lateral gradients, e.g. due to OL pulse shape, gradients in the sample thickness elements are much more difficult to resolve, and typically integration over all depth elements is applied. This integration also renders time-dependent processes, such as shock front propagation, complicated to follow using this geometry. Ideally, for this geometry, the sample should not exhibit any gradients as a function of thickness. To observe such gradients or follow the propagation of e.g. shocks or phase transitions, a perpendicular geometry could be used that allows the temporal and depth evolution of the OL impact on the sample to be imaged or scanned. In this geometry, lateral gradients of the OL-induced process are difficult to observe and are typically integrated over. An additional complication for this geometry is the non-excited sample volume, which is responsible for a relatively small signal-to-background ratio. Thus, experiment geometries with an angle between OL and X-rays varying from 0° (collinear) to 90° (perpendicular) have to be foreseen. An anti-collinear geometry (180°) has been proposed to study relativistic electrons and quantum states. This particular geometry has the advantage that the background due to bremsstrahlung radiation on a forward-scattering X-ray detector may be significantly reduced.

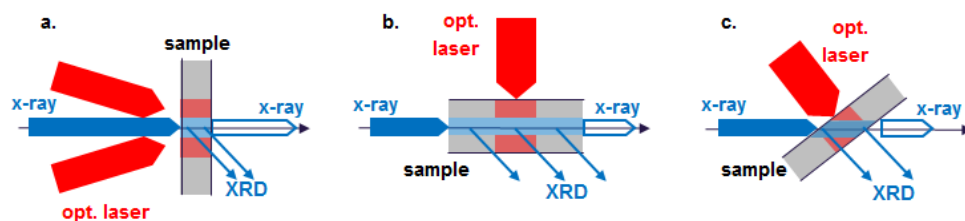


Figure 4-1. Possible experiment geometries with (quasi-)collinear (a), perpendicular (b), and general (c) configuration

4.5 Summary of instrumentation requirements

In the following section, the most important requirements are summarized for the X-ray beam delivery, the performance goals of the OL systems, and the experiment geometries, as concluded from the realization of the scientific goals and the analysis of the various X-ray and OL techniques to be applied. Table 4-3 provides an overview of the requirements to X-ray beam delivery. The major parameters of X-ray delivery are the photon energy $\hbar\omega$, the bandwidth $\Delta(\hbar\omega)$, the pulse energy E , the beam size(s) $\Delta x(\Delta y)$, and the polarization ($^\circ$). The Δ symbol stands for full width at half maximum (FWHM) values. In general, the requirements can vary widely. Therefore, selected parameter ranges are proposed and analysed for certain types of applications. In addition, the requirements to the pulse duration Δt and to the delay τ between pump and probe pulses depend on the scientific problem and range between O(10 fs), for extremely fast electronic processes, to O(100 fs), which is the maximum length and corresponds to the maximum photon number. Finally, the requirement for the repetition rate or time delivery pattern depends on the sample refreshment rate and the OL system repetition rate. Sample refreshment using liquid jets or gases (pulsed or residual) could achieve rates as high as 0.2–1.0 MHz. For solid samples, going beyond 10 Hz is not realistic at present. As to OL performance, the pump–probe (PP) laser system has been designed to deliver repetition rates of 0.2–4.5 MHz. A particular request for the time delivery pattern would be to provide the HED instrument with single X-ray pulses out of a train of X-ray pulses generated by the SASE2 undulator. Such a performance could allow parallel operation of the HED instrument with a second instrument at the SASE2 beamline.

Table 4-3. Overview of requirements to X-ray parameters originating from various applications and X-ray techniques. (Key: PP = pump–probe, IA = interaction, $\hbar\omega$ = photon energy.)

X-ray parameter	Application / X-ray technique	Required value / range	Comment
Photon energy	IA of intense X-ray pulse; damage; X-ray–driven processes, WDM generation	3, 5, 8, 12, 15 keV, K- & L-shell absorption edges, plasma lines	Few discrete $\hbar\omega$; high cross sections at lower $\hbar\omega$; material-dependent absorption edges; plasma lines
	XRD, SAXS, IXS, XPA, imaging (non-resonant)	5, 8, 12, 15, 25 keV	Few discrete $\hbar\omega$; Bragg condition might generate requirement
	RXRD, XAS, XCD	5–10 keV	Rare-earth L-edges
Bandwidth	High-resolution IXS	10^{-6} – 10^{-5}	Special crystal optics generating requirement to $\hbar\omega$
	XRD, SAXS, IXS, imaging, XPCS, XPA	10^{-4} to a few 10^{-3}	Standard crystal optics
	XRD, SAXS, IXS, imaging, XPA	10^{-4} to a few 10^{-3}	Standard crystal optics
	XAS, LD, S(Q)	10^{-2} – 10^{-1}	Special electron beam techniques
Pulse energy	X-ray heating & transition pumping	Max. flux, $O(10^{12}$ photons)	Variation with $\hbar\omega$ and electron bunch charge; Quasi-cont. due to limited no. of attenuators; E- or intensity-dependent exp.
	XRD, SAXS, imaging	10^8 – 10^{10} photons	Limitation due to detector saturation & sample IA
	IXS, etc.	10^{10} – 10^{12} photons	Limitation due to sample IA
PP delay	WDM generation, ultrafast dynamics & equilibration, IXS	0–50 ps	Max. value is given by SDU & depends on $\hbar\omega$
Beam size	WDM generation, X-ray excitation, damage	< few μm	Max. intensity and flux
	XRD, XAS, IXS, SAXS	< few μm	Spatial resolution in scanning mode
	WDM generation, damage	20 μm	Limited by optical diagnostics resolution (FDI, microscopy)
	XRD, XAS, IXS, SAXS	20 μm	Probe centre (homogenous excitation) of optical beam (diam. 20–50 μm)
	XRD, XAS, IXS, SAXS (imaging mode)	Coll. beam (< 500 μm)	Spatially resolving detector, powder diffraction
Polarization	Quantum states	> 95% linear	–
	Electronic states in high B fields	> 95% circular, flipable	Use of X-ray phase plates

Further X-ray parameters concern the coherence properties of the beam or the wavefront flatness. These parameters are important for coherent diffraction imaging techniques, but have at present not been analysed in detail.

The requirements to OL systems are summarized in Table 4-4, in a way analogous to those in Table 4-3, for the parameters pulse duration, pulse shape, pulse energy, wavelength, spot size, and temporal contrast ratio.

For the experiment geometry, the direction of the ultrahigh-intensity OL beam (UHI-OL) is particularly critical due to the directed background radiation and the corresponding shielding needs (see Section 8.3, “Experiment enclosure (HED-EXP)”). The collinear and perpendicular geometries, plus angles in between, seem to be the most important. An anti-collinear geometry might require further investigation. Further requirements, e.g. to ancillary instrumentation, are reported in the corresponding sections of Chapter 7, “Interaction chambers and ancillary instrumentation”.

Table 4-4. Overview of performance requirements and proposed OL systems originating from various applications

OL parameter	Application	Proposed system	Required value / range
Pulse duration	Relativistic plasmas	UHI-OL	30–100 fs
	Laser-driven phase transition	PP-OL	15–200 fs
	FDI	PP-OL	100 fs – 10 ps
	Dynamic compression	HE-OL	2–20 ns
Pulse shape	Dynamic compression	HE-OL	Ramp profiles
Pulse energy	Relativistic plasmas	UHI-OL	> 1 J
	Dynamic compression	HE-OL	> 100 J at 2ω
Wavelength	Relativistic plasmas	UHI-OL	800 nm
	Dynamic compression	HE-OL	~ 1050 / ~ 530 nm
Spot size	Relativistic plasmas	UHI-OL	3–20 μm
	Dynamic compression	HE-OL	10–200 μm
Temp. contrast ratio	Relativistic plasmas	UHI-OL	> 10^8

5 X-ray beam delivery

This chapter describes the various components of the X-ray beam delivery system for the HED instrument. After the major constraints and requirements to the X-ray delivery are considered, the photon beam properties as provided by the SASE2 undulator are summarized. The following section describes the various time delivery patterns to be applied at the HED instrument and discusses the related problems for X-ray optics and beam transport devices. Thereafter, the conceptual design of the X-ray optics and the beam delivery are discussed, addressing the various devices of the X-ray beam delivery.

5.1 Major requirements

Several constraints to the X-ray delivery for the HED instrument follow from the decision on the location of the instrument at the SASE2 south branch (S2S) beam transport. In particular, this location defines the accessible photon energies to above 3 keV. This energy is reached for operation of the electron accelerator at 10.5 GeV and the SASE2 undulator at a closed gap of 10 mm. Experiments requiring smaller photon energies will have to be carried out at the SASE3 scientific instruments. In addition, usage of the X-ray beam in the photon energy range from 3 to 5 keV will require specific solutions due to the increased divergence, higher absorption, and reduced damage threshold for X-ray optics and beam transport elements. In this 3–5 keV range, it will not be possible to provide the X-ray beam to the instrument maintaining the full performance of the source properties. The main photon energy range is therefore 5 keV and above. The maximum photon energy will be defined by the cut-off energy of 24 keV for the X-ray mirrors in the beam transport, provided that the FEL operates in saturation. A concept for a future extension to truly hard X-rays (O(60 keV), e.g. using the third harmonics) are outlined below, but will not be implemented as part of the baseline design of the HED instrument.

Another major constraint to the X-ray beam delivery is the time delivery pattern of the X-ray FEL beam. The high intensity of the X-ray pulses and, in particular, the extreme average power of beyond 4 kW during the 0.6 ms long X-ray pulse trains (see Figure 5-1), can generate a heat load on X-ray optical and beam transport elements that creates serious problems in terms of temperature stability and melting. This constraint has to be considered for each of the devices discussed in this section. An equipment protection system (EPS) will be implemented to avoid damage of beam delivery devices. This system is described in the last section of this chapter.

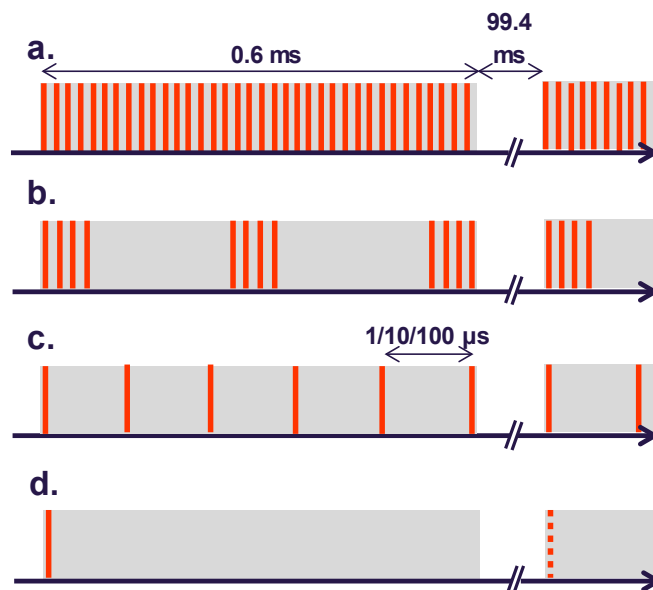


Figure 5-1. Required X-ray delivery patterns at the HED instrument. (a) Low-fluence measurements of repetitive processes and studies following dynamic processes on the 100 ns to ms time scale (e.g. following the response to an external magnetic field). (b) Groups of X-ray pulses. (c) Delivery at reduced repetition rate of 1, 0.1, or 0.01 MHz. (d) Single-pulse delivery with 10 Hz or even less.

A further and important constraint to the X-ray delivery concept is the stability, reliability, and ease of operation of the beam transport system. A single optical axis would allow simplified setting up and (re-)alignment procedures, in particular since the majority of experiments will also use optical lasers. We will see that the implementation of these requirements is very difficult to achieve. We will discuss this issue in the context of the selection of optical

focusing devices and of the monochromator and beam split and delay devices.

For the HED instrument, the following X-ray beam properties are of highest relevance:

- The pulse intensity I [W/cm^2]. This number rules the interaction of the X-ray beam with matter.
- The pulse energy E [μJ]. This number determines the count rate of most X-ray probing techniques and leads directly to the requirement of high transmission of the beam transport system.
- The beam transport system should transport the X-ray beam for the wide parameter ranges of the source in terms of photon energy, pulse duration, and bandwidth, while maintaining the source performance to the highest degree.

While imaging experiments will be performed at the HED instrument, the provision of extremely flat wavefronts will not be considered of highest priority, thereby easing somewhat the requirements to the optical elements. Due to the intrinsic properties of the SASE2 FEL radiation, the X-ray beam will nevertheless have a very high degree of spatial coherence, enabling all kinds of coherence techniques.

In terms of repetition rate of the X-ray beam, the HED instrument is special compared to other instruments. The majority of beam transport devices will be designed to accept X-ray pulse trains as delivered by the accelerator. But, due to the requirement of refreshing solid samples in between X-ray pulses, a sizeable fraction of experiments will be carried out at a maximum rate of 10 Hz. The use of high-energy lasers and high-field pulsed-magnet devices also constrains the repetition rate.

In order to enhance effectiveness of operation at the lowest repetition rates at the HED instrument, the delivery of individual X-ray pulses to the instrument is considered by means of a fast switching mirror or a specific electron beam delivery scheme, but needs to be investigated in more detail. Such a “pulse on demand” mode might work for rates of 1 Hz and below, and would allow

the other SASE2 instruments, such as the MID instrument, to take beam using the remaining > 90% of the available X-ray beam.

This CDR does not take the properties of seeded FEL radiation into account. However, following the proposal by Geloni et al. [33] and successful tests at LCLS [34], the implementation of hard X-ray self-seeding into the SASE2 undulator is presently being discussed. The beam properties at saturation vary mostly in spectral brilliance, due to the much narrower bandwidth and an increased longitudinal coherence. These properties will be easily maintained by the X-ray delivery system described in this report. By employing tapering schemes, the seeded beam could in addition attain much higher pulse energies. For these conditions, the constraints of damage to X-ray optics and beam transport devices will need to be verified. At the time of writing of the technical design report (TDR), the parameters for seeded FEL operation at SASE2 will be better known, and transport of this radiation can then be integrated into the TDR.

5.2 Time delivery patterns

The European XFEL beam operates with a baseline repetition rate of 10 Hz, accelerating trains of up to 2700 electron bunches at distances as small as 220 ns, which corresponds to ~ 4.5 MHz. In principle, this operation of the electron accelerator (sometimes called “burst mode”) provides an identical X-ray delivery pattern. However, the large numbers of electrons bunches are used for various purposes. The first bunches will be used for an intra-train feedback system leading to an improved stability of the electron delivery in position and time. Next, using a 10 Hz magnet, the electron bunches can be distributed to the two electron beamlines, thereby providing the possibility to operate all undulators at a base repetition rate of 10 Hz. And, finally, a fast electron kicker could generate and remove betatron oscillations of the electron bunches that suppress the SASE process. Likewise, FEL generation can be switched on and off for defined undulators. Overall, the electron beam delivery can be quite complex, but has the potential to provide the required pulse pattern to each of the scientific instruments. Figure 2-1 shows a few examples of required X-ray delivery patterns for the HED instrument.

An additional consideration for the X-ray delivery pattern is the effect of interaction of the X-ray pulse with beam delivery devices and also with the sample. Two major processes have to be distinguished. First, an intense X-ray pulse may lead to damage of the device or sample by melting, ablation, or plasma formation. Such a process would require only a single X-ray pulse and is therefore not related to the delivery pattern. Damage thresholds are discussed below in the context of outlining the X-ray focussing scheme. Second, the absorption of X-ray photons leads to energy deposition and heating. Since the small separation of X-ray pulses does suppress heat transport to a large extent, one has to consider cumulative heating effects. Heating will lead to deformation, dilatation, and in the worst case to melting. These effects will have to be carefully considered in the layout of the X-ray delivery system and will in general pose constraints to using a large number of X-ray pulses inside a train.

5.3 Radiation properties of the SASE2 undulator

The HED instrument will be located in the side branch after the SASE2 undulator of the European XFEL, as shown in Figure 2-1. The X-ray transport system spans approximately 1 km between the source point and the scientific instrument inside the experiment hall. The electron accelerator has three working points at 10.5, 14, and 17.5 GeV electron energy. An optimization of the overall facility layout has been done for 14 GeV electron energy, but reaching the smallest photon energies at 3–4 keV or the highest photon energies above 20 keV will require operation of the accelerator at 10.5 and 17.5 GeV, respectively.

Table 5-1 indicates photon energies in dependence of electron energy and SASE2 gap settings. Exact values will be known once the undulator tuning as part of the undulator construction is completed.

Table 5-1. Photon energies at SASE2 undulator as a function of electron energy and gap setting. The magnet period is 40 mm. Values shown in grey indicate that no FEL saturation is expected [1].

Electron energy [GeV]	Magnetic gap [mm]					
	10	12	15	20	24	28
10.5	2.3	3.4	5.5	10.5	14.9	18.6
14.0	4.1	6.9	9.8	18.7	26.5	33.1
17.5	6.4	9.3	15.3	29.2	41.4	51.7

The X-ray FEL radiation properties have been simulated by Schneidmiller and Yurkov [35]. They are listed in Table 5-2. A particular parameter is the charge of the electron bunch. Smaller-charge bunches can be compressed more strongly, therefore providing shorter X-ray bunches. For bunch charges of 20/100/250/500/1000 pC, X-ray pulse durations of 2/9/23/43/107 fs have been simulated. In general, higher bunch charge leads to the generation of X-ray pulses with higher pulse energy, narrower bandwidth, and less coherence.

An important consequence of the source properties and the long distances of the beam transport is the X-ray beam size. Using the centre of the third-to-last undulator segment (~ 12 m upstream of the end of the undulator) as source origin and employing analytical fitting yields for the estimated largest divergence $\Delta\theta_{max}$ and the associated beam size D_{max} [36,35]

$$\Delta\theta_{max}[rad] = 1.2 \times 10^{-5}(\lambda [nm])^{0.75}$$

$$D_{max} = \Delta\theta_{max} \times z$$

These are FWHM values. The 6σ beam size is then $D_{max_6\sigma} \sim 6/2.35 \times D_{max}$. In reality, the divergence changes with bunch charge and electron energy (see Table 5-2). The estimated smallest divergence is

$$\Delta\theta_{min}[rad] = 0.73 \times 10^{-5}(\lambda[nm])^{0.85}$$

This divergence is very close to the diffraction limit. The estimated beam sizes at a source distance of 220 m and 800 m are shown in Figure 5-2.

These distances correspond to the locations of collimation and monochromator optics (see below).

Table 5-2. SASE2 FEL radiation parameters at saturation and for selected photon energy and bunch charge parameters

Parameter	Unit	Value											
Photon energy	keV	3.0**			5.0			7.75			12.4		
Electron energy	GeV	10.5			14			14			14		
Bunch charge	nC	0.02	0.25	1	0.02	0.25	1	0.02	0.25	1	0.02	0.25	1
Peak power	GW	51	47	38	55	49	36	46	37	24	35	24	12
Source size (FWHM)	μm	38	49	58	33	41	49	31	39	46	29	37	49
Source divergence (FWHM)	μrad	6.3	5.1	4.3	4.1	3.3	2.8	2.8	2.3	1.9	1.9	1.5	1.3
Spec. bandwidth	1E-3	3.3	2.9	2.4	2.7	2.3	1.9	2.3	1.9	1.4	1.9	1.4	1.0
Photons/pulse	1E11	1.9	25	92	1.1	14	49	0.6	7.0	20.7	0.3	2.8	6.4
Pulse energy	μJ	85	1090	4050	92	1130	3920	76	864	2570	58	549	1260
Peak brilliance	1E33*	0.6	0.7	0.6	1.5	1.6	1.5	2.4	2.4	2.0	3.5	3.2	1.6
* In units of photons/(mm ² mrad ² 0.1% bandwidth s)													
** Calc. for 2.75 keV													
Parameter	Unit	Value											
Photon energy	keV	15.5			20.7			24.8					
Electron energy	GeV	14			14			17.5					
Bunch charge	nC	0.02	0.25	1	0.02	0.25	1	0.02	0.25	1			
Peak power	GW	29	15	9	21	11	7	25	13	8			
Source size (FWHM)	μm	29	35	54	28	39	60	25	36	55			
Source divergence (FWHM)	μrad	1.5	1.3	1.0	1.2	1.0	0.8	1.1	0.9	0.7			
Spec. bandwidth	1E-3	1.6	1.3	0.8	1.3	0.9	0.6	1.3	0.9	0.6			
Photons/pulse	1E11	0.2	1.4	4.0	0.1	0.7	2.1	0.11	0.8	2.2			
Pulse energy	μJ	49	347	991	35	248	708	42	302	863			
Peak brilliance	1E33*	4.3	2.5	1.6	5.0	2.7	1.5	7.6	4.0	2.3			

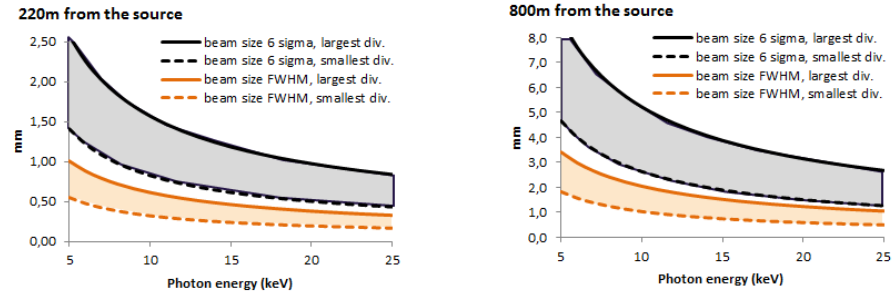


Figure 5-2. Estimated X-ray beam size without any focusing component at 220 m (left) and 800 m (right) from the source point. Shown are FWHM and 6σ size for the largest and smallest divergence.

5.4 X-ray beam transport components

The overall layout of the SASE beam transport has been shown in Figure 2-1. Here, we provide an overview of the devices of the HED X-ray delivery system, which is described in separate sections below. Figure 5-3 schematically shows the major devices and allocates these to the various buildings and rooms. Many X-ray devices will be installed in the beam delivery tunnels, at 150–390 m (XTD1) and at 835–873 m (XTD6). The HED experiment area is located inside the experiment hall (XHEXP), including a hutch (HED-OPT) for the X-ray beam definition and a concrete enclosure (HED-EXP) for the experiments. Three sample positions are currently foreseen (see Chapter 7, “Interaction chambers and ancillary instrumentation”) at a distance of 970–975 m from the source point. Figure 5-4 provides more details about the source distance of these HED X-ray devices.

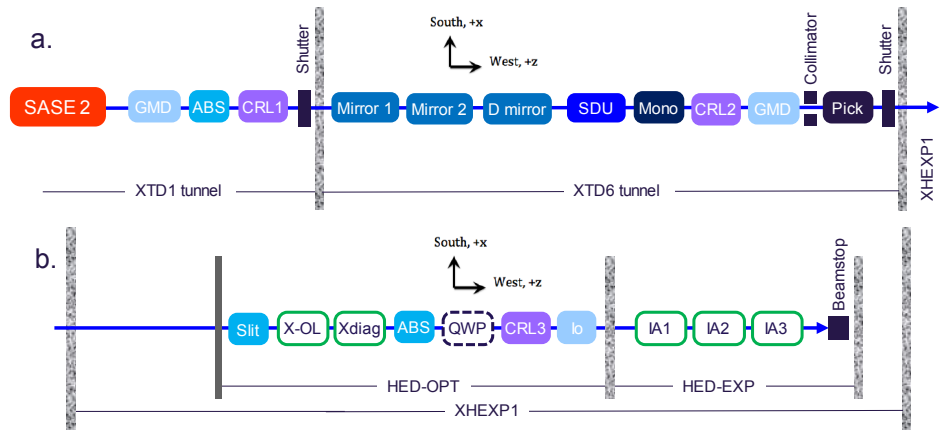


Figure 5-3. Schematic view of major X-ray delivery devices in (a) the XTD1 and XTD 6 tunnels and (b) in the experiment hall XHEXP. (Key: GMD = gas-based intensity and position monitor, ABS = removable, water-cooled, solid-state beam attenuator, CRLn = compound refractive lenses, Mirror 1 & 2 = offset mirror, Mirror D = S2S distribution mirror, SDU = split and delay, Mono = monochromator, Pick = pulse picker, X-OL = X-ray OL cross-correlation measurement, Xdiag = X-ray diagnostics instrument, QWP = quarter wave plate, I0 = Intensity measurement, IAn = interaction chambers.)

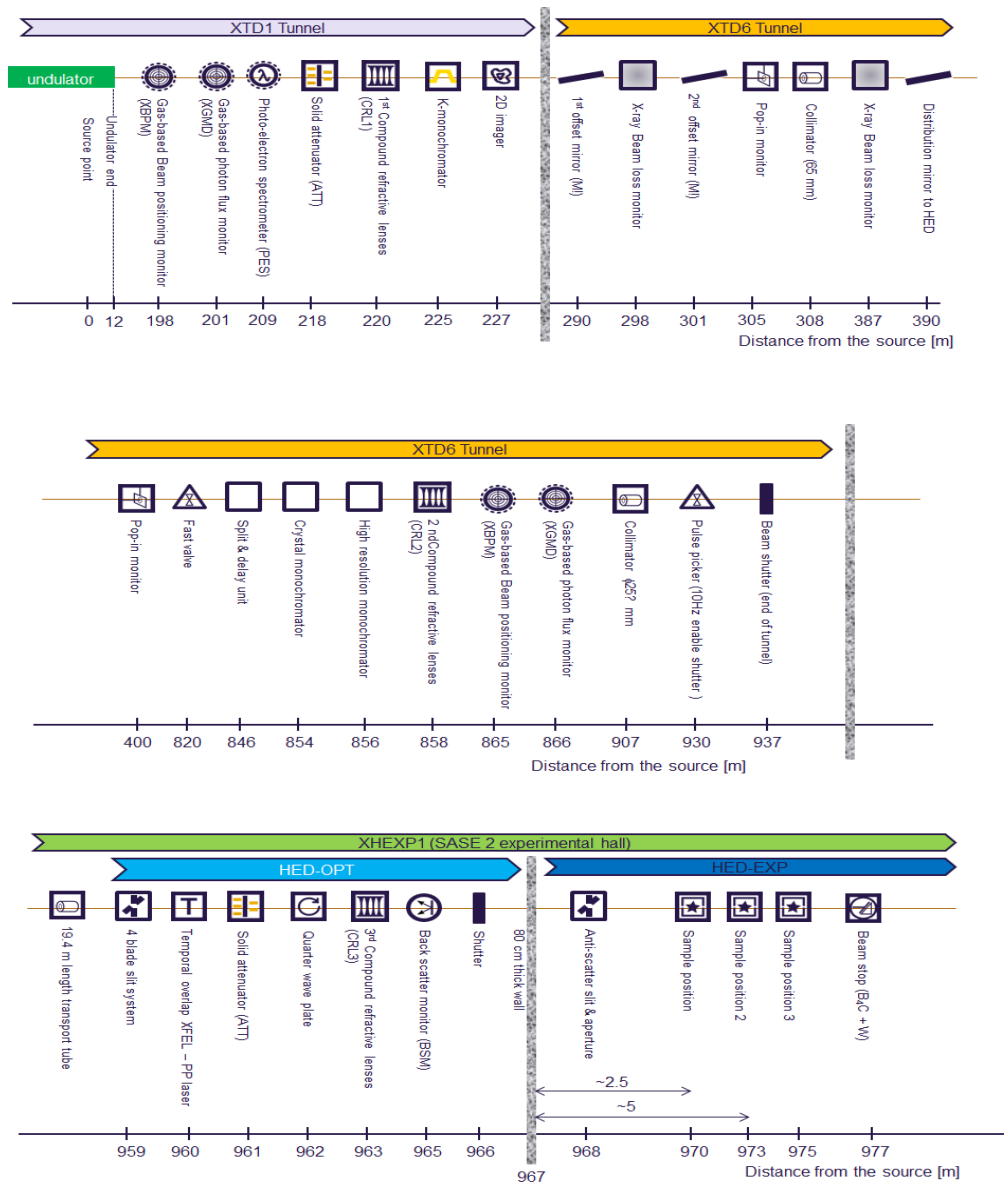


Figure 5-4. Details of HED X-ray devices, including source distances

Offset and distribution mirrors

At 290 and 301 m from the source point, two long mirrors with a useable optical surface of > 800 mm will be installed to horizontally offset the X-ray beam with respect to the straight line of the SASE2 undulator. These mirrors will remove spontaneous and bremsstrahlung radiation from the spectrum. Both mirrors use extreme grazing incidence angles of 1.1–3.6 mrad and generate a variable offset of 25–85 mm. The cut-off photon energy of these mirrors is ~ 25 eV for a grazing angle of 1.1 mrad and a boron carbide (B₄C)

coating with a density of 2.0 g/cm^3 . The first mirror will absorb most of the on-axis high-energy spontaneous radiation power, which could lead to deformation at full beam load. The deformation will be corrected by the second offset mirror, which will be bendable with radii larger than 50 km. The bending mechanism can also be used to focus the X-ray beam in the horizontal plane. This focussing functionality, which allows a matching of the X-ray beam size on the following distribution mirror, will not be utilized for most experiments at the HED instrument, since it creates two source points, thus making the focusing of the X-ray beam more complex.

At 390 m from the source, the distribution of the X-ray beam to the S2S side branch beam transport will be achieved by a third mirror, largely identical to the second offset mirror. This mirror also has a useable optical length $> 800 \text{ mm}$ and is set to operate at a grazing angle of 1.3 mrad in the horizontal plane. It also has a bending mechanism. The location and grazing angle of this mirror are chosen so as to optimize the separation from the central beam S2C at the end of the XTD6 tunnel to $\sim 1.4 \text{ m}$, while providing a high photon energy cut-off. The grazing angle of 1.3 mrad and the B_4C coating with a density of 2.0 g/cm^3 correspond to a cut-off photon energy of 21.4 keV . A higher cut-off of 23.8 keV can be reached by using the bulk Si substrate to reflect the X-ray beam. As a future option, it is possible to coat the mirror with a Pt stripe, either as a second or third reflection area. Using Pt with a coating density of 20 g/cm^3 , it is possible to attain a cut-off photon energy of 60.7 keV , while maintaining a reflectivity of above 0.95. This future operation mode requires a modification or extension of the offset optics and the focusing system.

Figure 5-5 shows the X-ray beam footprint on the distribution mirror for different configurations of CRL1 (largest divergence θ_{max} is assumed). It follows that, without any collimation or focusing, the distribution mirror clips the X-ray beam even below its FWHM size for $\hbar\omega < 10 \text{ keV}$. Focusing by the second offset mirror or using X-ray beam collimation by means of CRLs will thus be necessary to maximize the throughput of the X-ray beam delivery system.

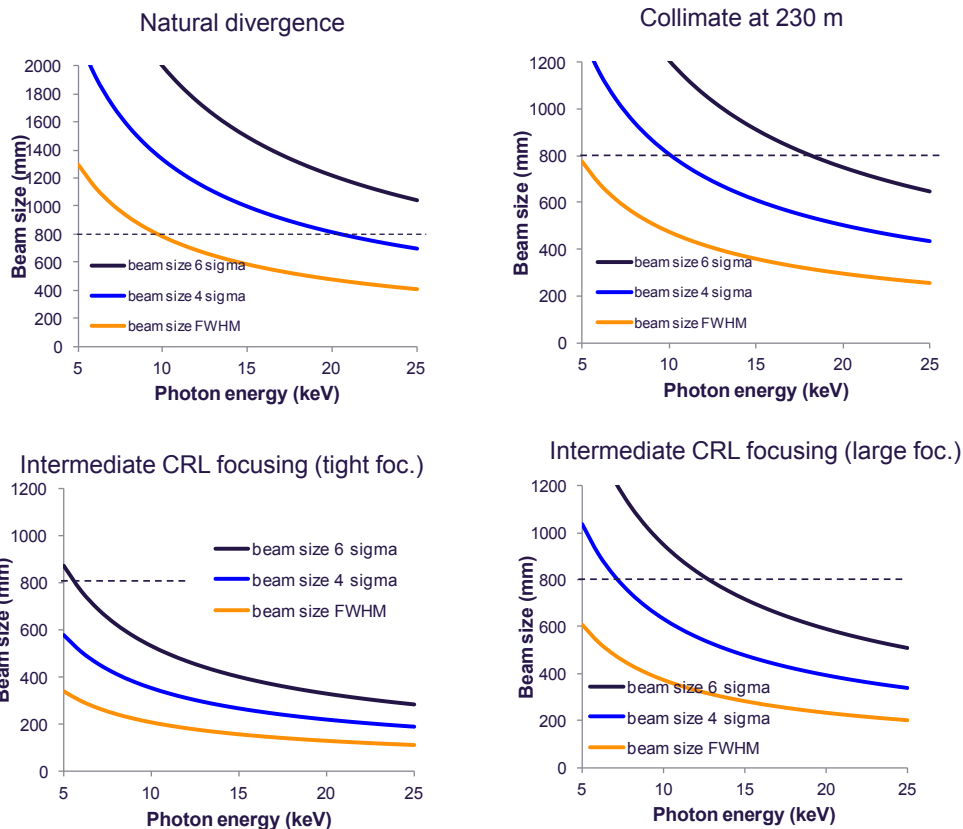


Figure 5-5. X-ray beam footprint on the distribution mirror at 390 m from the source. The grazing angle on the mirror is 1.3 mrad. The horizontal dashed line indicates the effective size of the mirror (800 m). Black/blue/orange lines represent $6\sigma/4\sigma/\text{FWHM}$ values for natural divergence, parallel/collimated beam, and two kinds of intermediate focusing (see “X-ray focusing scheme” on page 71). In all cases, the most conservative divergence is assumed.

In general, when using X-ray mirrors for beam distribution, only one of the instruments at SASE2 can receive the X-ray beam at any moment in time. This is also the current mode of operation. The HED instrument may, however, feature experiments that have a small repetition rate on the order of 1 Hz and even below. This rate is mostly determined by the ancillary HED systems used to excite the sample or create extreme electromagnetic fields. It would therefore be very interesting to use only every tenth X-ray pulse train for experiments at the HED instrument, or to switch on demand to even smaller rates. The remaining X-ray pulse trains could be used at the other SASE2 instruments with less than 10% average flux reduction, likewise enabling operation of two instruments in a quasi-simultaneous mode.

To enable such a mode, two possibilities can be considered: either using a special electron beam delivery leading to two separate X-ray beams, or employing the distribution mirror in a fast switching mode. The latter method seems favourable at present, and the European XFEL X-Ray Optics and Beam Transport group (WP73) will study the possibility to integrate a piezo-electric device in the distribution mirror mechanics to move the mirror at a frequency of up to 1 Hz.

X-ray focusing scheme

The requirement for the X-ray beam size on the sample will vary depending on the experiment. One can distinguish between tight focusing with beam waists of $\phi_{\text{FWHM}} \approx 1 - 3 \mu\text{m}$, medium focusing with $\phi_{\text{FWHM}} \approx 20 - 40 \mu\text{m}$, and large focusing or collimated beam for $\phi_{\text{FWHM}} \approx 100 - 500 \mu\text{m}$. Sub-micrometre ultratight focusing will require very short focal lengths, entailing the integration of the optics into the interaction chambers. For this report, we do not consider this option, but we will continue to investigate how to implement ultratight focusing. In the following sections, we introduce the focusing scheme as part of the HED X-ray delivery system. Because of their simplicity, robustness, and the conservation of the optical axis, it is proposed to employ beryllium-based compound refractive lenses (Be CRLs) [37]. Beryllium is an ideal CRL material due to its high transmission and correspondingly low absorption. This low absorption reduces the heat load issue and enables a large effective aperture, which eventually determines the diffraction-limited beam size.

There are, however, some negative aspects of using Be CRLs for focusing:

- Due to the increased absorption, the application of Be CRLs for photon energies below 5 keV still requires more detailed investigation and is not reported here. A focusing scheme for the photon energy range 3–5 keV needs to be developed in the next realization step of the HED instrument.
- The CRLs are chromatic, and the natural bandwidth of the SASE FEL radiation already leads to a widening of the focal spot sizes. For wide-bandwidth operation, e.g. XAS or X-ray magnetic circular dichroism (XMCD) experiments, and for scanning the photon energy over ranges of

100 eV or more, the consequences for the focal spot properties need to be analysed. For photon energy changes, CRL settings need to be modified, leading to the requirement of focal-spot diagnostics.

- When extending the operation range to very hard photon energies, a large number of Be lenses has to be employed. This could become a funding issue.

Before defining the focusing system, we need to analyse the issue of damage caused by the intense, focused X-ray pulses. This is important since we may be forced to design the focusing system so as not to create foci in the location of components that could be subject to damage.

Damage estimation

We consider here 5 keV as the lowest photon energy using the CRL focusing. The value thus represents the highest absorption by Be and other materials, therefore also the highest dose. The use of higher photon energy is generally “safer” due to the increased attenuation length in the light-Z materials considered in this section. The attenuation length thus the damage threshold differs strongly for materials exhibiting an absorption edge in the X-ray range of interest. Such materials need to be investigated separately in the future. We also do not consider damage due to illumination by multiple X-ray pulses in this section.

The important parameter for single X-ray shot damage is the averaged energy η deposited per atom

$$\eta \text{ (eV/atom)} = \mu_a \times F = \mu_a \times \frac{NE}{A}$$

where F [J/cm^2] is the fluence of the X-ray beam, and N , E , and A are the number of photons, photon energy, and exposed area, respectively. The atomic attenuation coefficient μ_a (cm^2) is

$$\mu_a = \frac{\mu_l m_a}{\rho N_A} \text{ (cm}^2\text{)}$$

where μ_l (cm^{-1}) is the linear absorption coefficient, m_a (g/mol) is the atomic mass, ρ (g/cm^3) is the mass density, and $N_A = 6.02 \times 10^{23}$ is Avogadro's

number. Figure 5-6 shows μ_l for Be, B₄C, and Si. Recent studies show that the single-shot damage threshold for B₄C corresponds to 0.62 J/cm² or ~ 1 eV/atom at 0.83 keV photon energy [38]. For the design of the overall beam transport systems [36], the damage threshold of 0.7 eV/atom for B₄C and 0.4 eV/atom for Si have been used. For Be, experience tells that, at about 600 K ($\Delta T \sim 300$ K), some structural change occurs. We therefore aim to stay below this value for single or multiple exposures. It should be noted, however, that eventually more experimental studies will be needed to confirm the assumptions. Steady-state operation may also require considerable safety factors. For the current design level, we use a dose of $\eta = 0.1$ eV/atom for Si and B₄C as an allowed operation threshold, and $\Delta T \sim 30$ K for Be.

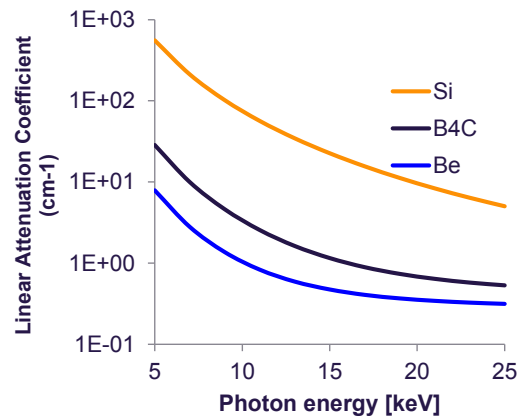


Figure 5-6. Linear attenuation coefficient μ_l for Si, B₄C, and Be

Figure 5-7 shows the energy deposited per atom η vs. photon energy for 10^{12} photons in an area $A = 100 \times 100 \mu\text{m}^2$ for Be, B₄C, and Si. One obtains that B₄C remains clearly below the threshold dose of $\eta = 0.1$ eV/atom, while Si is in a critical regime. Using this analysis, we consider as minimum acceptable spot sizes for Si $200 \times 200 \mu\text{m}^2$, and for B₄C $70 \times 70 \mu\text{m}^2$ at a photon energy of 5 keV. Figure 5-7 also shows how this minimum spot size varies with photon energy. For Be, the spot size of $70 \times 70 \mu\text{m}^2$ corresponds at 5 keV to a temperature increase of $\Delta T \sim 30$ K in a single shot. In the following, we will use these values for a critical analysis of the focusing scheme and of the devices located in beam transport sections with reduced beam size and therefore increased potential damage.

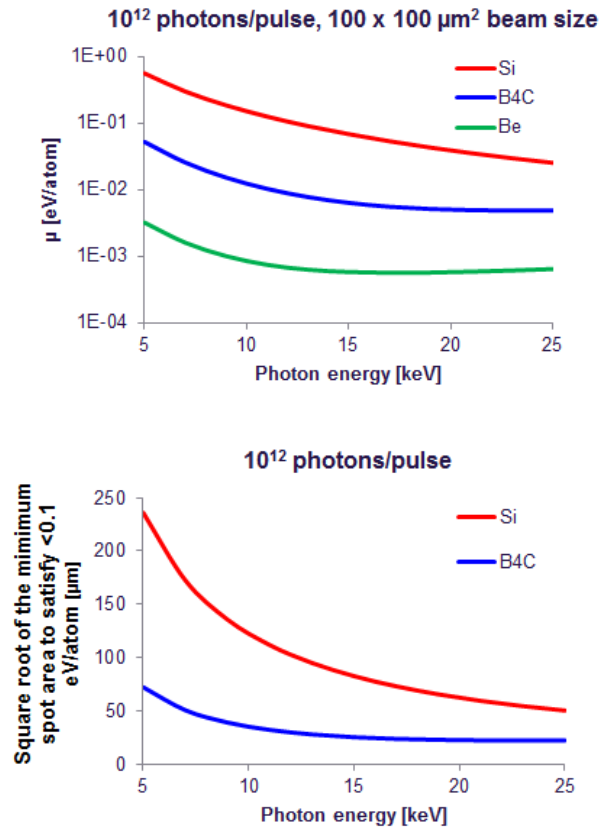


Figure 5-7. (Top) Energy deposited per atom for 10^{12} photons per pulse and a beam area of 0.01 mm^2 . (Bottom) Minimum X-ray beam size to maintain $\eta < 0.1 \text{ eV/atom}$.

CRL basics

CRLs consist of stacks of single lenses as shown in Figure 5-8. The surfaces of the lenses are paraboloids of rotation given by

$$z = \frac{x^2}{R}$$

where R is the radius of curvature at the apex of the parabola profile, and x and z are the transverse and longitudinal directions with respect to the X-ray beam, respectively. Using the thin-lens approximation gives the focal length f as,

$$\frac{1}{f} = \frac{1}{p} + \frac{1}{q}$$

where p and q are the distances from the source to the CRL and from the CRL to the sample, respectively. In the thin-lens approximation, the focal length of a CRL with equal radius of curvature on both sides is given by

$$f = \frac{R}{2N\delta}$$

where N is the number of single lenses, and $n = 1 - \delta + i\beta$ is the refractive index of the material with $\delta = 2.23 \times 10^{-6} \times \lambda^2 [\text{\AA}]$ for Be. For $\delta < 1$ in the X-ray domain, concave shapes are required for focusing.

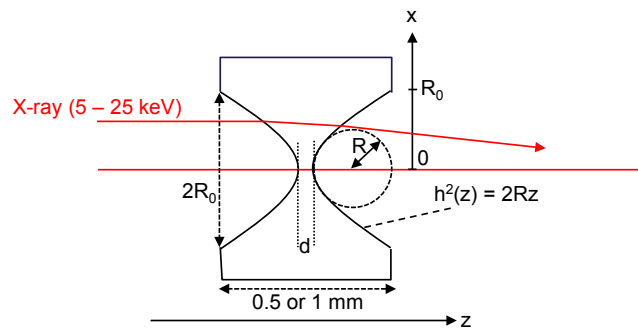


Figure 5-8. Parabolic compound refractive lens (CRL). The individual lenses will be stacked behind one another [37].

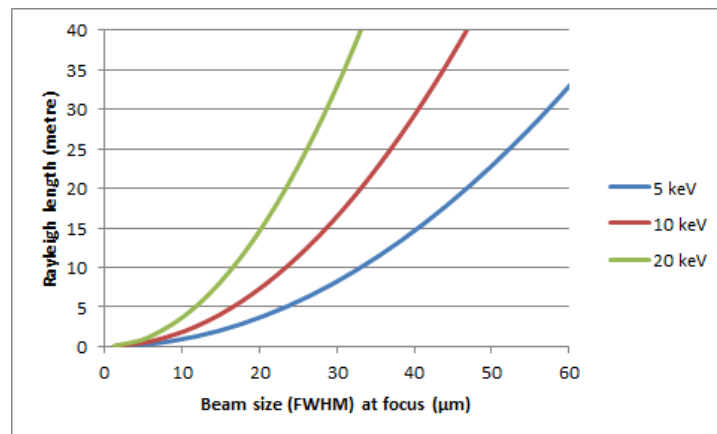


Figure 5-9. Rayleigh length vs. beam size for 5, 10, and 20 keV photon energy

The acceptance of the lens can be limited by absorption. The imaginary part $i\beta$ of the refractive index describes the absorption of a lens, with $\beta = \lambda\mu_l/4\pi$ for the linear coefficient of attenuation μ_l and the X-ray wavelength λ . The transmission $T(x)$ is

$$T(x) = e^{-\mu_l h(x)} = e^{-\frac{\mu_l N x^2}{R}}$$

In 1D, the Gaussian beam intensity distribution right after the CRL is

$$\begin{aligned} I_{\text{out}} &= I_{\text{in}} T(x) \\ &= A e^{-x^2/2\sigma_{\text{in}}^2} \times e^{-\mu_l h(x)} = A e^{-x^2/2\sigma_{\text{out}}^2} \end{aligned}$$

where σ indicates half of the beam waist right before (σ_{in}) and after (σ_{out}) the lens and $1/(\sigma_{\text{out}}^2) = 2\mu N/R + 1/(\sigma_{\text{in}}^2)$. This implies that, due to absorption, transmission through the lens reduces the beam size. The total 1D transmission for the Gaussian beam is simply given by $\sigma_{\text{out}} / \sigma_{\text{in}}$, and 2D transmission is $(\sigma_{\text{out}} / \sigma_{\text{in}})^2$. Taking finite lens thickness d at the apex into account, the total transmission T_{total} is

$$T_{\text{total}} = \exp(\mu N d) \times (\sigma_{\text{out}} / \sigma_{\text{in}})^2$$

The smallest achievable focal spot size of a coherent X-ray beam is determined by the diffraction limit, which is given by $d_{\text{dif}} \sim (\lambda/2NA)$. Here, $NA = \text{MIN}(D_{\text{eff}}, d_{\text{out}}) / 2q_2$ is the numerical aperture. D_{eff} is the effective aperture of the lens [37], and $d_{\text{out}} = 2.355\sigma_{\text{out}}$ is the FWHM beam size right after the lens.

The beam size near focus does not change much over the Rayleigh length: $Z_R = \pi\omega^2 / \lambda = 4\pi\sigma^2 / \lambda = 2.27d_{\text{dif}}^2 / \lambda \propto f^2 \lambda^{-1}$, where f is the focal length of the lens. The definition of Z_R is the distance between the focal point and the point where the beam size gets $\sqrt{2}$ times bigger than the waist size. The total focal depth is thus defined as $2Z_R$. While for tight focusing, the Rayleigh length is of the order of centimetres (1 μm waist size leads to $Z_R = 18$ mm at 5 keV), and for large foci the damage threshold is not an issue anyway, great care will be necessary for medium focusing. For an X-ray spot size of 35 μm , the Rayleigh length at 5 keV is longer than 10 m. All X-ray delivery devices

before and behind the focus in HED-OPT and HED-EXP are therefore affected.

CRL configuration

In order to provide the required beam sizes, a configuration with three CRL assemblies is chosen. The first device, CRL1, is used to parallelize or even marginally focus the X-ray beam diverging from the source. This is required to enable a high throughput of the X-ray delivery system, which otherwise has to deal with very large beam sizes (see Figure 5-5). For the photon energy range below 10 keV, intermediate focusing needs to be employed to provide a beam size at the distribution mirror allowing a 4σ beam transport. CRL1 will be placed at 220 m from the X-ray source and shared with the MID instrument. Its distance to the source is defined by the requirement to parallelize the 5 keV beam using a single lens. The second device, CRL2, is located at 858 m from the source, near the end of the beam transport inside the XTD6 tunnel. CRL2 is used to focus the X-ray beam on the sample position, responding to the requirement of intermediate focusing. The third device, CRL3, will be located as close as possible to the sample position, currently at the end of the optics hutch HED-OPT. This device at 963 m from the source provides tight focusing with a distance to the sample position varying between 7 and 12 m, depending on the interaction chamber. Figure 5-10 shows the three CRL devices, their location, and the application in focusing configurations employing intermediate focus to increase throughput.

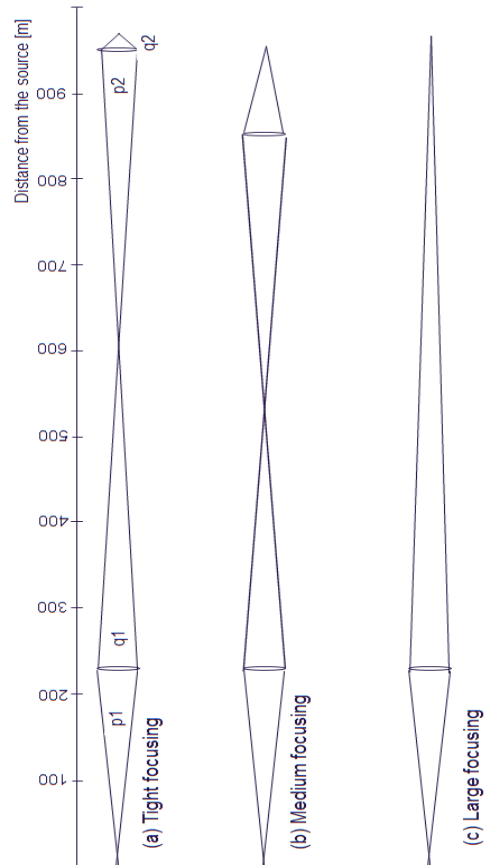


Figure 5-10. (a) Tight-focusing configuration of the CRLs. First CRL at 220 m from the source focuses the X-rays around 595 m. Second CRL images this intermediate focusing point onto the sample. (b) Medium focusing. (c) Large focusing. Details are summarized in Table 5-3.

Tight focusing

Tight focusing is particularly interesting for X-ray excitation experiments, but also for imaging in divergent-beam geometry. The best way is to place the focusing lens as close as possible to the sample. The concept is to place CRL3 at around 7 m upstream of the position of the first chamber (IA1, see Chapter 8, “Experiment hall layout”). In order to maximize the throughput and the flux on the sample, the X-ray beam will be prefocused at 595 m (365 m behind CRL1). At 5 keV, the 2D transmission of CRL1 is > 90% and > 95% above 10 keV. For an X-ray beam size at CRL3 of ~ 940 μm (FWHM), the transmission of CRL3 drops to ~ 50% due to absorption. Furthermore, the beam size on the exit side shrinks to ~ 740 μm (FWHM). The expected beam

size at focus is varying from 1 to 3 μm over the photon energy range of 5–25 keV. Taking total beam transport throughput into consideration, X-ray intensities from a few 10^{17} to nearly 10^{18} W/cm^2 have been calculated (see Table 5-3).

Medium focusing

Larger spot sizes of $\phi = 10\text{--}40$ μm are achieved by using the CRL2 far from the sample. Figure 5-10(b) shows CRL2 at 112 m upstream of the sample. The total 2D transmission in this geometry will always be higher than 90% (see Table 5-3). For this focusing configuration, the long Rayleigh length paired with a relatively small focus lead to a long zone before and after the focus with potential to damage X-ray delivery devices.

Large focusing

The easiest way to achieve the large (> 100 μm) spot is direct focusing using CRL1 (see Figure 5-10(c)). In this geometry, the source is geometrically magnified by $738/230 = 3.2$, giving $\phi_{\text{geo}} \approx 120$ μm . The diffraction-limited focus, however, is even bigger, with ~ 240 μm for 5 keV, high-charge operation (~ 1 mJ, see Table 5-3). This implies that Si-based X-ray optics are still radiation safe, but care will be needed as this beam size is still not far from the damage threshold (see Figure 5-7).

A summary of lens configurations, transmittances, expected spot sizes, and expected focus intensities is given in Table 5-3. Note that the thickness of the lens at the apex is neglected in this calculation. The transmission, and thus intensity and diffraction-limited spot size, are slightly too optimistic. Due to the chromatic nature of the CRL, the third-harmonic component of the X-ray beam will be focused behind the focal plane for the fundamental frequency, towards the detector. Special attention is needed to avoid damage of detectors and other components. We also note that, in the sections above, only the situation for focusing in the focal plane was considered. In general, it is also possible to place the focus at different locations before or behind the sample location. Likewise the beam size at the sample will become larger. While this is wanted in certain situations, and is actually proposed to modify

the X-ray beam size on sample, one needs to consider wavefront distortion away from the focal plane. This issue still requires more analysis.

Table 5-3. Beam size, total 2D beam transmission (assuming thickness at the apex of the lens = 0), and intensity in the focus for various lens geometries. Two extreme divergence cases (most conservative and optimistic) are considered. Intensity: $I = 0.5 \times T \times E / (\Delta t \times \pi d^2)$ for $\Delta t = 2\text{--}100$ fs depending on bunch charge. Assuming 50% of the total energy inside FWHM spot. (Key: E = pulse energy, T = transmittance, d = spot size at FWHM, Δt = pulse width.)

	photon energy	wavelength (nm)	divergence	Bunch charge	pulse duration	Pulse energy	photon number per pulse	Distance source-CRL1	Distance CRL1 - prefocusing point	Distance prefocusing point - CRL2 or 3	Distance CRL2 or 3 - sample	2D total transmittance	photon number on sample	Diff limited spot size $\sim \lambda d_{out}/f$	Intensity
	keV	nm	micro-rad	nC	fs	microJ		metre						micron	W/cm ²
Tight focusing	3	0,41	6,3	0,02	2	85	1,77E+11	220	372	372	7	0,24	4,3E+10	4,0	4,1E+16
	3	0,41	5,1	0,25	23	1090	2,27E+12	220	372	372	7	0,36	8,1E+11	4,3	5,7E+16
	3	0,41	4,3	1	107	4050	8,44E+12	220	372	372	7	0,43	3,6E+12	4,6	4,9E+16
	5	0,25	4,1	0,02	2	92	1,2E+11	220	372	372	7	0,61	7,0E+10	2,5	2,9E+17
	5	0,25	3,3	0,25	23	1130	1,4E+12	220	372	372	7	0,71	1,0E+12	2,9	2,7E+17
	5	0,25	2,8	1	107	3920	4,9E+12	220	372	372	7	0,77	3,8E+12	3,2	1,7E+17
	12,4	0,10	1,9	0,02	2	58	2,9E+10	220	372	372	7	0,92	2,7E+10	1,7	5,6E+17
	12,4	0,10	1,5	0,25	23	549	2,8E+11	220	372	372	7	0,95	2,6E+11	2,2	3,0E+17
	12,4	0,10	1,3	1	100	1260	6,4E+11	220	372	372	7	0,95	6,0E+11	2,5	1,2E+17
	20,7	0,06	1,2	0,02	2	35	1,1E+10	220	372	372	7	0,95	1,0E+10	1,6	4,0E+17
20,7	0,06	1	0,25	23	248	7,5E+10	220	372	372	7	0,96	7,2E+10	1,9	1,7E+17	
Medium focusing	5	0,25	4,1	0,02	2	92	1,2E+11	220	319	319	112	0,92	1,1E+11	34	2,3E+15
	5	0,25	3,3	0,25	23	1130	1,4E+12	220	319	319	112	0,94	1,3E+12	39	1,9E+15
	12,4	0,10	1,9	0,02	2	58	2,9E+10	220	319	319	112	0,99	2,9E+10	27	2,5E+15
	12,4	0,10	1,5	0,25	23	549	2,8E+11	220	319	319	112	0,99	2,7E+11	34	1,3E+15
	20,7	0,06	1,2	0,02	2	35	1,1E+10	220	319	319	112	0,99	1,1E+10	25	1,7E+15
	20,7	0,06	1	0,25	23	248	7,5E+10	220	319	319	112	0,99	7,4E+10	31	7,3E+14
Large focusing	5	0,25	4,1	0,02	2	92	1,2E+11	220	750	-	-	0,97	1,1E+11	220	5,9E+13
	5	0,25	3,3	0,25	23	1130	1,4E+12	220	750	-	-	0,98	1,4E+12	259	4,6E+13
	12,4	0,10	1,9	0,02	2	58	2,9E+10	220	750	-	-	1,00	2,9E+10	180	5,7E+13
	12,4	0,10	1,5	0,25	23	549	2,8E+11	220	750	-	-	1,00	2,8E+11	228	2,9E+13
	20,7	0,06	1,2	0,02	2	35	1,1E+10	220	750	-	-	1,00	1,1E+10	170	3,8E+13
	20,7	0,06	1	0,25	23	248	7,5E+10	220	750	-	-	1,00	7,5E+10	205	1,6E+13

Split and delay unit

An X-ray split and delay unit (SDU) is foreseen with the aim to generate two collinear X-ray pulses with various delays τ . Applications will be X-ray pump–probe, sequential imaging [39], or temporal coherence characterization [40]. A similar device using carbon-coated mirror pairs has been successfully implemented at FLASH for photon energies of up to 0.2 keV [41].

The SDU for the HED instrument will be installed inside the XDT6 tunnel, 846 m from the source, which corresponds to 124 m upstream of the sample. The current SDU layout is designed for photon energies of 5–20 keV. Mo/B₄C and Ni/B₄C multilayers are employed as an X-ray splitter, mirrors, and mixers. The Mo and Ni multilayers are optimized in reflectivity for photon energies above and below 10 keV, respectively. All reflections are in the vertical plane. Wavefront splitting is applied at the second mirror, which acts as a splitter (labelled “BS” in Figure 5-11). Spatial overlapping is enabled by tweaking the mixer mirror slightly such that two beamlets converge and overlap on the sample. Given the rocking curve width of the mixer multilayer, the distance to the sample has to exceed 100 m. The delay is adjusted by mechanical movements of four of the eight mirrors in the beam. Each mirror has several stripes to adapt it to the specific configuration. The multilayer stripes are exchanged by horizontal translation of the inner girder on which all optical devices are mounted. As a special mode of operation, splitting the fundamental at ~ 5 keV from the third harmonic at ~ 15 keV will also be possible. This mode allows the sample to be excited at low $\hbar\omega$ with high fluence, and probed with a temporally delayed third-harmonic pulse at a maximum delay of 4 ps. The 4 keV / 12 keV pump–probe configuration allows slightly longer delays (e.g. 6 ps), but the CRL throughput at 4 keV is limited. It will also be possible to vertically separate one of the split beams. This mode could be used to insert the subsequent monochromator (see “Monochromator” on page 83) for one beamlet only. Typically, the pump beam will require higher flux (thus without monochromator) and the probe beam will require narrower bandwidth (with monochromator). The concept of how and where to compensate the vertical offset has not been clarified yet and is a subject of further investigation.

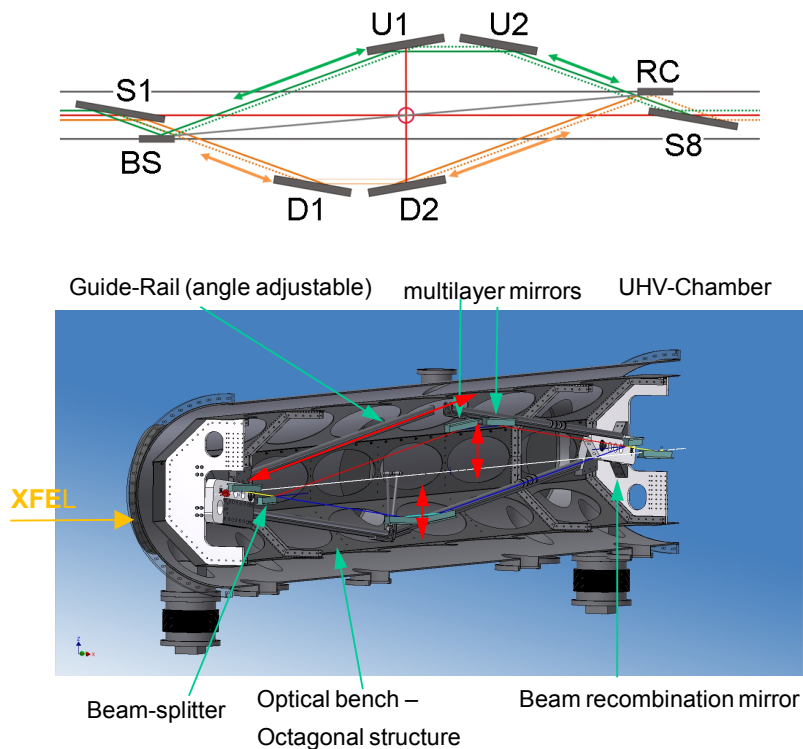


Figure 5-11. (Top) Schematic drawing of the optical layout of the SDU. The X-ray beam is divided geometrically at the beam splitter (BS). The mirrors U1, U2, D1, and D2 can be moved along the beam direction to change the delay τ . The lower (orange) beam will be reflected by the recombination mirror (RC) onto the last mirror S8. (Bottom) Mechanical layout of the optical bench with the optomechanical components.

Since multilayers are chromatic devices, the angle of incidence on the mirror will have to be adjusted for different photon energies to match the Bragg condition. As a consequence, the maximum possible delay τ between pump and probe pulse depends on the photon energy and the multilayer choice. Table 5-4 indicates the maximum delay and overall transmission for different photon energies.

Other performance specifications of the SDU are as follows:

- The 190 mm long mirrors will have a clear aperture of $\sim 6\sigma$ footprint of the X-ray beam for the range of 5–20 keV.
- Coherent diffraction effects induced by wavefront splitting need to be evaluated.

- The SDU will allow different splitting ratios (not only 50/50) between the pump and the probe beam.
- The mirror re-alignment for changing the photon energy will be done remotely via the instrument control system.

For alignment and calibration purposes, two diagnostic stations will be required before and behind the SDU. The device before the SDU will be used to couple a beam, which should be detected on the second device, into the SDU. The system will be developed through an external contribution from Westfälische Wilhelms-Universität Münster (U Münster), Germany, funded by a grant from the German Federal Ministry of Education and Research (BMBF-VBF) [42]. U Münster will also participate in the installation and commissioning of this device.

Table 5-4. Multilayer material, Bragg angle, maximum delay, and total transmission T of the SDU device for photon energies from 4–20 keV

Photon energy [keV]	Multilayer	Bragg angle [°]	Delay [ps]	T
4	Ni (W)	4.58	36	0.16
5		3.66	23	0.23
6		3.07	16	0.33
8		2.3	9	0.47
10		1.83	6	0.21
10	Mo	2.28	9	0.29
12		1.9	6	0.35
15		1.52	4	0.41
18		1.27	3	0.43
20		1.14	2	0.23

Monochromator

Crystal monochromators reflecting in the vertical plane will be employed to increase the spectral resolution from the typical X-ray FEL radiation bandwidth of 10^{-3} by one or more orders of magnitude. As a standard device,

a Si(111) monochromator will be installed inside the beam transport in XTD6 at a distance of 854 m from the source, ~ 114 m upstream from the sample. This device was optimized to reduce angular vibrations and will enable cryogenic or water cooling. Very accurate angular motion will be performed using a precise linear translation (see [43]). The energy range of the monochromator is designed for 4.8–23.8 keV. The artificial channel-cut geometry allows high surface finish, but leads to a variable vertical beam offset of around 10 mm, with a variation in offset of ~ 0.85 mm in the designated photon energy range. Such an offset is problematic for operation, as switching between monochromatic and non-monochromatic modes will likewise require tedious re-alignment and re-adjustment procedures. Two possibilities have been discussed to avoid this issue. First, it is possible to steer the X-ray beam such that it arrives at the monochromator with a vertical offset compensating its own vertical offset. This would work for a single energy, but requires meticulous alignment of the X-ray beam on the monochromator. Second, an additional monochromator with inverted geometry could compensate the offset. Such a four-bounce geometry will work for the entire photon energy range without further adjustment of the X-ray beam, but requires fine adjustment of the two monochromators. Due to the extremely small divergence of the X-ray FEL radiation, the four-bounce geometry does not reduce the monochromatic flux considerably. Using peak reflectivities of 0.9 for each of the two additional reflections, the four-bounce geometry still allows ~ 80% throughput. A further possibility would be to use the second monochromator using Si(511) or Si(555) reflection to achieve a higher spectral resolution of $\Delta\hbar\omega \sim 10^{-5}$ and $\sim 10^{-6}$, respectively. While the Si(511) could simply be mounted on the standard monochromator and cover a fairly large photon energy range of 8–24 keV, the Si(555) requires a somewhat different geometry and covers only a much narrower photon energy range of 10–13 keV. In addition, these high-resolution monochromators could be employed to compensate the vertical offset induced by the first monochromator, but this compensation works only for one photon energy and has to be re-aligned if the photon energy is changed. Figure 5-12 shows a mechanical drawing of the monochromator table with two vacuum vessels, each carrying one artificial channel-cut monochromator crystal.

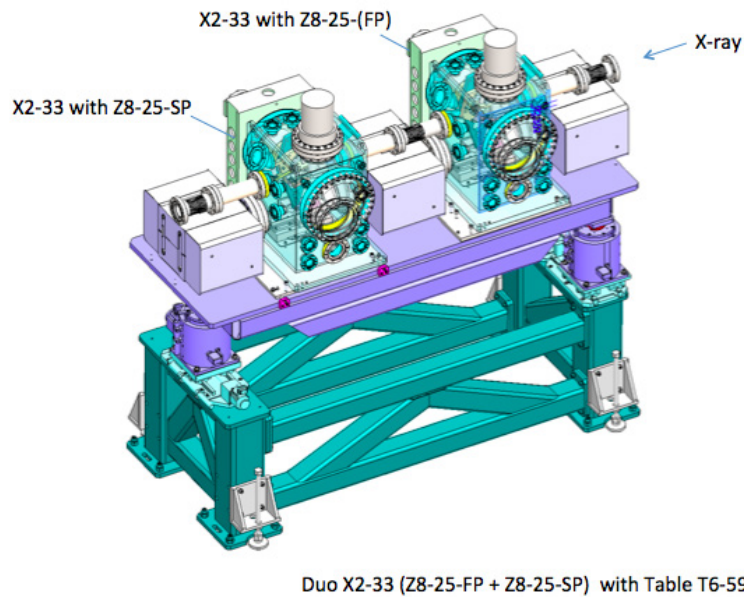


Figure 5-12. Mechanical drawing of the monochromator table carrying two vessels for two monochromator assemblies. Drawing provided by X. Dong (WP73), based on a design by D. Shu (Argonne National Laboratory, ANL).

Attenuators

Attenuators are required to adjust the beam intensity in case the full intensity generates damage or heat distortions on subsequent X-ray delivery devices, and to adjust the beam intensity on the sample for fluence- or intensity-dependent investigations. While the former adjustment is typically made once per experiment, the latter requires changes and settings by the user. For this reason, two attenuator devices are integrated in the HED beam transport. The first device, at 218 m from the source, is used to adjust the beam intensity for commissioning and alignment operations, and also to reduce the heat load on optical elements if necessary. The effects of these first attenuators and their expected wavefront distortion of the beam profile on sample will have to be investigated. These attenuators will consist of 8 to 10 insertable water-cooled carbon pieces of different thicknesses between 75 μm and 20 mm, providing an attenuation of 10–100 over the entire energy range [43].

The second attenuator device will be located inside HED-OPT and allow the user to adjust the intensity or fluence on the sample by changing the attenuation of the incident beam. The requirement to attenuation can be as high as eight orders of magnitude (OD 8). In the framework of the

Femtosecond X-Ray Experiments (FXE) instrument [44], a design has been developed and further optimized consisting of four actuator arms, each holding up to six absorbers in a ladder configuration (see Figure 5-13). Each arm can be moved completely out of the beam. The absorbing pieces will be mounted on water-cooled metal rods. The optimization of the attenuation level will be achieved by using a combination of Si and chemical vapour-deposited (CVD) diamond. The current idea is to have absorber units of 300 μm thick Si and 75 μm thick CVD diamond. Using two arms equipped with 1, 2, 4, 8, 16, and 32 units for each material gives maximum thicknesses of 19.2 mm (Si) and 4.8 mm (CVD) for 64 units. The combined operation of both CVD and Si is important for the lower photon energies due to high absorption. To attenuate the beam below the Si melting threshold, the CVD diamond will be placed in front of the Si attenuators. In order to prevent an accidental irradiation of the copper rods with the FEL beam, a radiation-hard aperture made of for example B_4C should be placed in front of the foil holders.

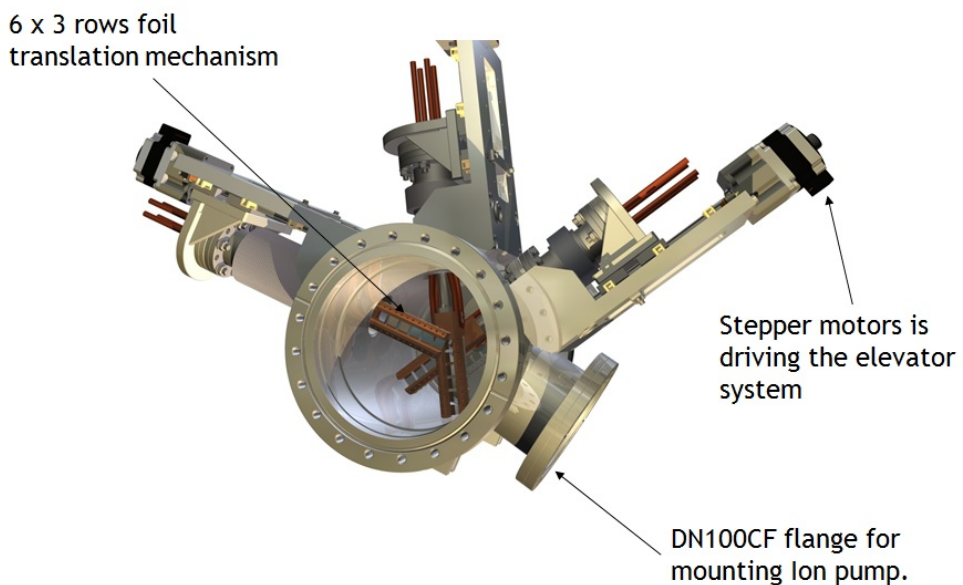


Figure 5-13. Mechanical design and concept of the three-arm attenuator. Design provided by JJ X-Ray, Denmark.

Performance requirements

- The attenuator system should provide $> 10^8$ attenuation at a photon energy of 5–20 keV and $> 10^4$ at 20–25 keV.
- An incremental attenuation of at least three steps per decade will be provided.
- The foil holders should be designed as a fork and have an appropriately set limit, so they cannot be driven into the X-ray FEL beam.
- The filters must not be damaged or degraded when exposed to the full X-ray beam flux at 10 Hz operation in any CRL lens configuration across the 5–24 keV spectral range. 4.5 MHz full-bunch operation, or 3–5 keV operation, should be possible with some limited operation mode.
- The attenuators should preserve the transverse coherence of the FEL radiation to the highest extent achievable.
- The attenuator system is required to change state remotely via the instrument control system. A status signal that indicates the current state of each filter is required. The status of each attenuator should be recorded in the experiment metadata.

In accordance with these requirements, the selection of attenuators and thicknesses and their attenuation are shown in Figure 5-14. Detailed values are given in Table 5-5.

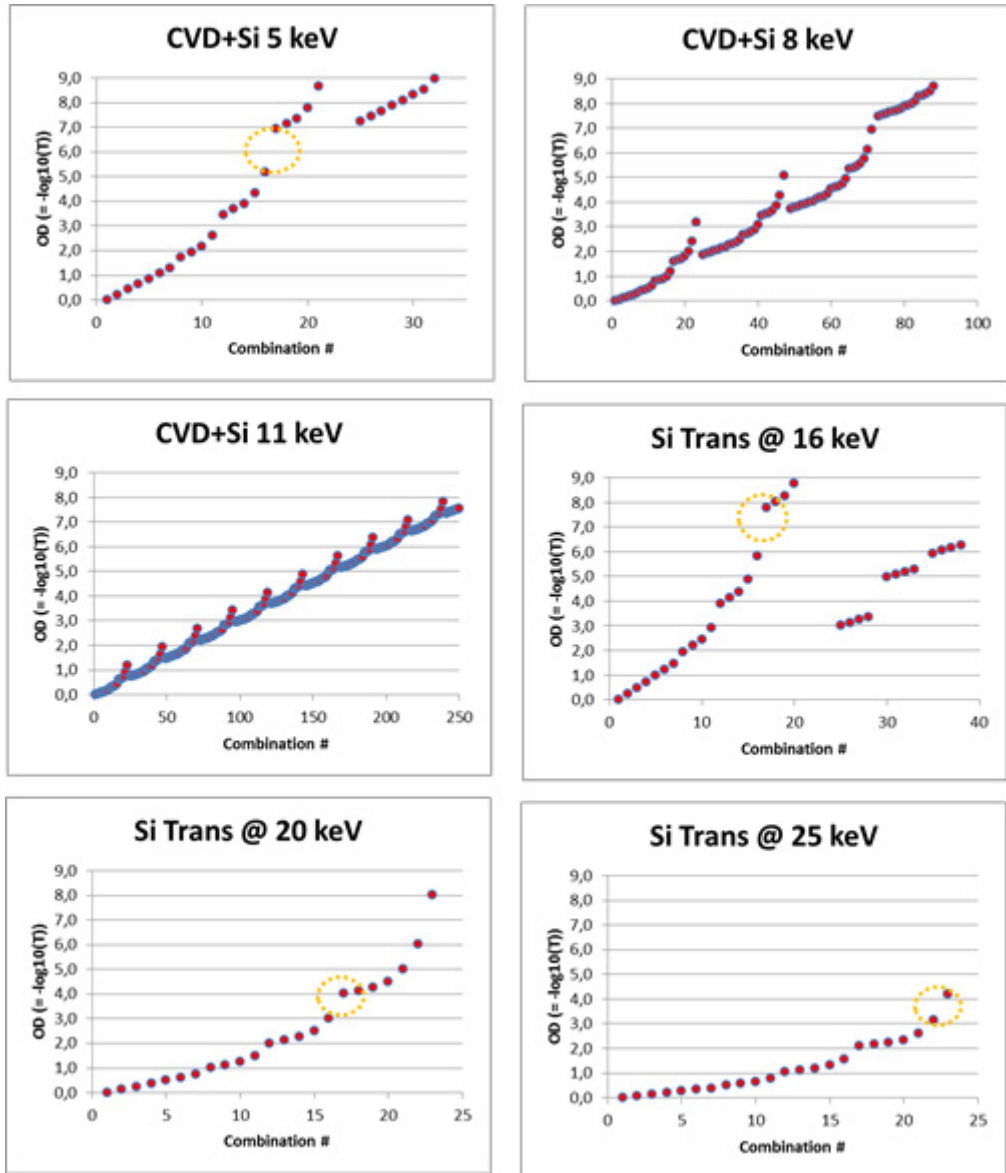


Figure 5-14. Attenuation for various photon energies as a function of filter units. Vertical axis indicates OD value ($= -\log_{10} T$). Orange circles indicate the points where the requirements mentioned in the text are not satisfied.

Table 5-5. Attenuation per step and maximum attenuation for selected X-ray energies. $OD = -\log_{10} T$

Photon energy [keV]	Average step [T%, OD]	Max. attenuation
5	39%, 0.22	$> 10^8$
8	11%, 0.05	$> 10^8$
11	4%, 0.02	$> 10^8$
16	< 43%, 0.24	$> 10^8$
20	< 25%, 0.13	$> 10^8$
25	14%, 0.07	$> 10^4$

5.5 X-ray diagnostic devices

For adjustment and online control of the X-ray properties, several diagnostic devices will be employed in the HED X-ray delivery system. As online devices, the residual gas-based photoelectron spectrometer (PES), X-ray gas monitor detector (XGMD), X-ray beam position monitor (XBPM), and backscatter monitor (BSM) at the end of the beam transport are available. These devices can also accept the highest repetition rates of the X-ray delivery. Furthermore, a time tool providing X-ray–OL cross-correlation measurement should allow online data taking at 10 Hz repetition, while higher repetition rates are limited by detector performance. The same applies to spectrum measurement devices, which are very specific to the experiment, however, and therefore may only be integrated into the specific experiment but not as a permanent device. And finally, insertable screens will be required to verify beam shape and position. These monitors will be invasive and are restricted to 10 Hz single-bunch operation.

Photoelectron spectrometer (PES)

This device is located in the first section in XTD1, upstream of the offset mirrors, at 209 m from the source. Using Xe or Kr residual gas, it measures electron spectra using a time-of-flight detector [45]. Ideally, it will provide mean photon energy and bandwidth of the X-ray radiation. The resolution will

depend on the photon energy since the photoelectron energy depends on the distance to the absorption edge. A further uncertainty is the dynamic range of the device. No experience exists yet with such detectors operated in the hard X-ray energy range, but first devices have been constructed and will be tested with X-ray FEL radiation in the near future.

Intensity and beam position monitor (XGMD, XBPM)

Online non-destructive X-ray FEL pulse-resolved measurement of the photon flux and position is essential. A first beam position monitor and intensity monitor set will be installed in the first diagnostics section, at ~ 200 m from the source. A second set will be installed near the end of the photon tunnel, at ~ 865 m from the source. The second beam monitor also detects losses and position shifts induced by mirrors, CRLs, and other X-ray devices.

The X-ray gas monitor detector (XGMD) and X-ray beam positioning monitor (XBPM) were developed and will be built by a team from Deutsches Elektronen-Synchrotron (DESY), Germany, the Ioffe Physico-Technical Institute in St. Petersburg, Russia, and the Physikalisch-Technische Bundesanstalt (PTB) in Berlin, Germany. The operation of the detector is based on the atomic photoionization of residual gases. The detector will work at up to 25 keV photon energy, but at reduced dynamic range due to the decrease of the photoionization cross section. The XGMD/XBPM units have to meet the requirements listed in Table 5-6.

Table 5-6. Performance requirements for the XGMD and XBPM for the HED instrument

	Requirement	Remarks
Bunch resolution	Pulse-resolved	Pulse-resolved for the XGMD and averaged (≥ 20 s) for the XBPM
Calibration	Relative	Some means to relate to absolute measurement must exist
Targeted absolute measurement uncertainty	$< 10\%$	Higher precision needed for small pulse energies (pump); $< 10\%$ for high pulse energies (probe)
Min. photon energies	3 keV	Core range 5–15 keV; performance reduction is acceptable in extended range
Max. photon energies	25 keV	
Min. dynamic range	10^8 ph/pulse	—
Min. dynamic range	10^{13} ph/pulse	—
Target position monitoring accuracy	$< 30 \mu\text{m}$	$< 10 \mu\text{m}$ desirable
Min. flux density	10^8 ph/ mm^2 /pulse	—
Max. flux density	1.4×10^{12} ph/ mm^2 /pulse	—
Number of bunches per bunch train	~ 200	—
Bunch pattern(s)	0, 1, few, 100, or 200 pulses at 10 Hz	—
Monitor location	~ 930 m	At tunnel end in front of pulse picker
X-ray beam diameter (at monitor)	$\sim 1200 \mu\text{m}$ (at 15 keV)	—
	$\sim 2500 \mu\text{m}$ (at 5 keV)	—
Stay-clear aperture	$\sim 2500 \mu\text{m}$	—

Backscatter monitor (BSM)

This device is located 965 m from the source and ~ 5 m in front of the sample inside HED-OPT. Using backscattering from thin foils, the X-ray pulse energy can be measured. Using appropriate photodiodes located upstream of the foil, the BSM will deliver pulse-resolved signals proportional to the X-ray intensity. If four diodes are placed in a square configuration, in principle, beam position measurements can be performed. These signals are recorded by medium-fast digitizers with several 100 MHz bandwidth.

Spectrum measurement

The gas-based online spectrometer is designed to deal with the high repetition rate of full bunch trains, and offers least interference to the experiment. But this device provides only moderate energy resolution. On the other hand, a crystal-based single-shot spectrometer can provide higher resolution, but it is more invasive. We plan to install one transmissive crystal spectrometer just upstream of the distribution mirror in XTD6 at 380 m from the source.

Insertable screens

Insertable screens will be needed for measurements of the X-ray beam shape and position. In general, such measurements will be performed only for alignment and adjustment purposes. The screens must be removed before full bunch train operation can be enabled. Optical cameras used for detection of scintillator light cannot operate at 4.5 MHz rate either. Also, tuning of the X-ray optics will be restricted to single-bunch operation (10 Hz) for safety reasons. The screens could have a secondary function as adjustment supports using an optical alignment laser to pre-align components in the hutches without X-rays. For this purpose, the scintillators have to be designed for X-ray scintillation and feature a rough surface to scatter the optical laser, in order to detect its position on the screen with the optical camera.

5.6 Vacuum system

The vacuum system of the HED instrument starts at the interface to the beam transport vacuum at the entrance to the experiment hall XHEXP. At this position, the vacuum has to clearly fulfil the strict requirements defined for the ultrahigh-vacuum (UHV) system in the beam transport section. This will be controlled by a pressure measurement on the instrument side of the last valve of the beam transport system. In case the vacuum exceeds a preset level, the valve will close and operation of the instrument will be interrupted.

The ~ 40 m vacuum system of the HED instrument has three major sections. Following a 20 m long transport tube without any optical elements, several devices are located inside the HED-OPT hutch, with options for future installation of special optics. The third section is that of the HED-EXP area, which includes several experiment chambers.

The vacuum in the transport tube will be measured, and, if the pressure is below 1×10^{-7} mbar, a signal will be sent to the interlock system to enable the beam transport into this area and the HED instrument. In normal operation, the pressure in this section will not exceed 1×10^{-7} mbar. Pumping will be achieved using ion getter pumps.

The connection to the HED-OPT section is windowless, but the necessity of installing a collimator (similar to those inside the beam shutter) will be investigated. Devices located in HED-OPT will be permanently under vacuum. In normal operation, the pressure in this section will not exceed 1×10^{-7} mbar, and pumping will be achieved using ion getter pumps. These conditions are very comparable to the optics areas at usual radiation installations.

In normal operation, the connection to the HED-EXP section will be windowless. However, it will be investigated if a valve with a window could be used for specific operation modes to enable usage of the X-ray beam in air in HED-EXP. For < 200 pulses per train operation mode (~ 330 kHz), a diamond window should work [44]. Such an operation mode would significantly facilitate alignment and change procedures in the experiment area.

Furthermore, apertures will be introduced for differential pumping at the boundary between HED-OPT and HED-EXP, thus allowing operation of the experiment chambers at an elevated vacuum level. Devices located in HED-EXP during experiments are usually under vacuum, as the high-power laser beams also require vacuum operation, but with much reduced requirements. The pressure in this section will be aimed at $< 1 \times 10^{-6}$ mbar in order to be able to reliably operate ion getter pumps. The exact vacuum layout, in particular for the multiple interaction chambers, will have to be defined as part of the TDR.

5.7 Equipment protection system (EPS)

Several devices of the HED instrument need to be connected to the equipment protection system (EPS) in order to avoid catastrophic damage by X-ray beam interaction or heating. Table 5-7 lists these devices and indicates the operation modes to be selected if the corresponding device is inserted into the beam. Modes 1 to 4 correspond to 1, 30, 200–1350, and 2700 pulses/train, respectively. Insertion of a valve will lead to the interruption of beam operation. An exception would be the window valve at the interface between HED-OPT and HED-EXP, which will be operated with beam in the closed state.

Table 5-7. HED devices and their EPS operation mode

Device	EPS operation mode	Device	EPS operation mode
CRL1	Mode 3	Attenuator	Mode 3
M3 (distr. to S2S)	Full beam (Mode 4)	CRL3	Mode 2
SDU (incl. diagn.)	Mode 2	CRL3	Mode 2
Monochromator (std.)	Mode 3	Beam monitor	Mode 4
Monochromator (HR)	Mode 3	Window valve	Mode 2–3
CRL2	Mode 3	Beam stop	Mode 3–4
Slits	Mode 3	—	—
Time tool	Mode 2–3	—	—

6 Optical laser installations

This section describes the various laser systems to be used at the HED instrument and gives an overview of their implementation. The current layout was developed with a preliminary understanding of the initial installations and an expectation towards future laser installations. The overall concept how to build up and integrate initial and future laser installations is called “*The Laser Plan*” and is described in the next section.

6.1 “The Laser Plan” for the HED instrument

Combining high-energy laser systems with an X-ray FEL source will offer unique opportunities for experiments that cannot be performed anywhere else in the world. A radiation-shielded experiment area (see Chapter 8, “Experiment hall layout”) and the provision of ample space to build up these lasers, plus the possibility to connect to an external, dedicated laser building, will create a huge opportunity for new science. It will be the responsibility of the scientific community to make best use of the unique properties of the X-ray pulses. It is expected that the platform provided by the HED instrument will be complementary to other existing high-energy laser platforms worldwide. Experiments will need to be performed differently compared to current practice at high-energy all-optical-laser installations. It is also very clear that having the highest laser intensity, energy, and power will not be the first priority. Instead, reliable, stable, and easy operation will be of utmost importance. Other important parameters include a high repetition rate, spatial and temporal contrast, and exact temporal shaping of the laser pulses for dynamic compression applications. High repetition rates of 1–10 Hz enable repetitive experiments to be performed, high statistical accuracy to be achieved, and large parameter ranges to be covered.

An initial list of requirements for all OL installations to be installed at the HED instrument includes:

- System performance—such as reliability, stability, ease of operation, uptime, maintenance, and precision (e.g. contrast, fluctuation, etc.)—is more important than peak performance.
- High repetition rate of 1–10 Hz will be aimed at.
- Laser systems will be specified for the type of experiments to be performed at the HED instrument. This means that the requirements to the laser systems could vary significantly from those at other OL installations.

At present, the science case for the high-energy/power optical lasers is still open and under discussion in the scientific communities.

Two types of applications of high-energy/power laser systems can be distinguished:

- 1 Long-pulse (ns) lasers to dynamically compress matter. This case has been made as early as 2005 and aims at scientific topics related to high-pressure, high-temperature material properties with relevance to astrophysical and materials sciences.
- 2 Ultrashort-pulsed (fs) high-intensity lasers to excite matter relativistically. This case has been made fairly recently in 2011 and aims at studying microscopic processes in matter exposed to extreme electromagnetic fields.

The challenges for both areas are the required laser parameters. For dynamic compression, laser pulse energies eventually reaching beyond 1000 J combined with precise temporal pulse shaping are the final goal (see Figure 3-5). While such lasers exist today at very large laser installations, their implementation into the HED instrument and the requirement to operate at suitable repetition rates is challenging in terms of budget, space, and ease of operation. For relativistic laser–matter interaction, the precision of the laser delivery is critical to achieve the microscopic resolution aimed for. This concerns mostly the spatial profile and the temporal contrast of the laser. The delivery of OL and X-ray pulses has to occur with high precision in time,

space, and energy, as a reduced precision would lead to a raised uncertainty in the experimental results. To fulfil these requirements, the laser system and transport must be stabilized and the various parameters monitored using appropriate diagnostic and measuring devices. Pulse-by-pulse measurements of the beam pointing and the pulse energy will be performed for each of the laser systems near the sample location. While these measurements are more or less standard techniques, the stabilization of the arrival time is a complex procedure, in particular if one aims at femtosecond resolution and if the synchronization of several independent sources is required. The temporal synchronization concept will be discussed in Section 6.8, “Laser synchronization and diagnostics”.

At present, it seems that the initial installation of OL systems, which should be operational in early 2016, will not fulfil all of the requirements listed above. However, “The Laser Plan” should enable to upgrade or replace the initial systems at a later moment in order to reach the expected performance. Room for new developments should also be provided within this envelope. In the following, we briefly lay out “The Laser Plan”.

Activity 1 – Installations until 2016

As part of this programme, the integration of three major plus several secondary laser systems into the HED instrument is planned. Table 6-1 gives an overview of these laser systems.

Table 6-1. Laser systems considered for initial installation until 2016

Laser type	Basic property	Amplification scheme
PP-OL	800 nm / 200 μ J / 15 fs / 4.5 MHz 800 nm / > 3 mJ / 15 fs / 200 kHz 1030 nm / 100 mJ / 0.8 ps or 0.5 ns / 200 kHz	NOPA Yb amplifier
UHI-OL	800 nm / 3–5 J / 30 fs / 1 Hz	Ti:sapphire
HE-OL	1057 nm (glass) or 1064 nm (YAG) / 100–200 J / 2–20 ns / 1–10 Hz	Nd-glass / flashlamp or Nd-YAG / diode

Pump–probe optical laser (PP-OL)

For high repetition rate experiments, only the PP-OL is available with pulse energies of up to a few mJ or even 100 mJ for ~ 15 fs to sub-ns pulse durations, respectively. This laser will be available in 2016 in its almost final version. The PP-OL will also be used for OL–X-ray cross-correlation measurements to determine X-ray arrival time, temporal jitter, and more. This laser will also serve as a time reference for the UHI-OL using OL–OL cross-correlation techniques. The PP-OL will be installed on the floor of XHEXP, and all of the beam distribution will occur in this horizontal plane (see Chapter 8, “Experiment hall layout”). The European XFEL team—in particular the Optical Lasers group (WP78)—is solely responsible for this system. The PP-OL system will be fully embedded into the European XFEL data acquisition (DAQ) system.

Ultrahigh-intensity femtosecond optical laser (UHI-OL)

This ultrahigh-intensity short-pulse laser system will be a “standard” Ti:sapphire chirped pulse amplification laser reaching up to 100–200 TW on sample. The specifications for the UHI-OL system still require more work, in particular with respect to the properties of the pulses on sample. However, implementation of the UHI-OL system is considered achievable within the coming years and as part of Activity 1. The laser will operate at up to 1–10 Hz and will be synchronized using the high-resolution fibre distribution at the facility. Additional jitter of laser delivery, etc. will be measured using cross-correlation with the PP-OL. The UHI-OL will be installed in the HED-LAS room on top of the experiment enclosure (HED-EXP). The pulse compressor to generate short pulses down to ~ 30 fs will be installed in HED-LAS, and the compressed, but unfocused beam will be transported to HED-EXP through a hole in the concrete floor of HED-LAS. The UHI-OL contribution encompasses not only the laser itself, but also its infrastructure, the laser transport, the compressor, the diagnostics, and the manpower to design, install, and commission the laser. The UHI-OL must be integrated as much as possible into the European XFEL DAQ system. The responsibility for the UHI-OL is with the HIBEF UC. European XFEL will coordinate the integration and will need to approve technical designs, integration, installation, and commissioning. WP78 will supervise the laser-relevant activities, while the

HED instrument group (WP82) will coordinate other activities related to the integration of the UHI-OL system.

High-energy nanosecond optical laser (HE-OL)

Definition of the long-pulse laser system is ongoing at present. The difficulties lie in the choice of an appropriate technology scalable to full energy, and in the definition of requirements to temporal shaping of the nanosecond-ramped pulses. Using conventional flashlamp-pumped Nd:glass technology, building a 100 J system with 1–10 Hz repetition rate seems to be feasible. This system can be upgraded to 1000 J level by installing an additional final amplifier with larger beam diameter and reduced repetition rate down to 0.1–0.01 Hz. To reduce the energy consumption and facilitate high repetition rates, the development of diode-pumped high-energy lasers is of high relevance. One of the risks in employing this technology is that it is only about to emerge and no laser of this type operates today. The proposal to build a 100–300 J diode-pumped long-pulse laser system through scientific collaboration has been made recently by the Rutherford Appleton Laboratory of the Science and Technology Facilities Council (STFC) in the UK. We will have to decide in the coming months if such a scenario is realistic. A related challenge is the requirement for precise temporal shaping. Temporal-shaping technology already exists, and is routinely employed at much larger laser facilities [46].

Like the UHI-OL, the HE-OL will be installed in the HED-LAS room on top of the experiment enclosure. The beam will be transported in air, without temporal compression, through a hole in the floor to the experiment area. It is foreseen that, initially, a 100 J system will be built, and then later upgraded to the order of 1000 J. The HE-OL contribution not only encompasses the laser itself, but also its infrastructure, the laser transport, the diagnostics, and the personnel to design, install, and commission this laser. The laser must be integrated as much as possible into the European XFEL DAQ system. The distribution of resources for the laser system still needs to be decided. European XFEL may contribute to this laser and its infrastructure, but will not be able to fund a 100 J system on its own. A significant part of the funding needs to be provided by the HIBEF UC. The responsibility for the HE-OL will have to be clarified once the project is better defined. European XFEL will

coordinate the integration and will need to approve technical designs, integration, installation, and commissioning. WP78 will supervise the laser-relevant activities, while WP82 will coordinate other activities related to the integration of the HE-OL system.

Activity 2 – Research and development until 2016

This activity should be launched immediately after conclusion of the UC agreement in order to prepare for the future upgrades as part of the proposal.

Table 6-2. R&D projects until 2016

Laser system	R&D activity	Partners
UHI-OL	Establish science case for pulse intensities beyond 200 TW.	HIBEF UC, European XFEL
	Implement high-pulse contrast schemes (spatial, temporal).	HZDR
HE-OL	Develop 100–1000 J diode-pumped laser system.	RAL/STFC
	Integrate precise temporal-shaping capability.	RAL/STFC, LLNL

Activity 3 – Installations beyond 2016

This activity is the least defined part of the overall project, since it depends heavily on the outcome of Activity 2. As of today, it seems likely that upgrades or replacements of the initial laser installations will be part of this activity.

Table 6-3. Laser system upgrades considered for beyond 2016

Laser system	Upgrade
UHI-OL	Increase power on sample to few 100 TW or possibly beyond. Also higher energy and longer pulses are considered.
HE-OL	Implement 1000 J (green) laser system.

The following sections provide more details about the various laser systems.

6.2 Pump–probe laser system (PP-OL)

The PP-OL system [47] is currently being developed by the Optical Lasers group (WP78) at European XFEL. A large variety of different pulse specifications and delivery patterns is foreseen in anticipation of user requests (see Table 6-4). The PP-OL uses an 800 nm wavelength with pulse durations down to 15 fs and pulse energies of up to 0.2 mJ for 4.5 MHz full-burst mode (see Figure 6-1). The bandwidth $\Delta\lambda_{\text{FWHM}}$ is approximately 60 nm (for Gaussian-shape pulse). The system can deliver higher pulse energies up to 3–5 mJ when operated at a reduced repetition rate of 200 kHz intraburst. The PP-OL uses optical parametric chirped pulse amplifier (OPCPA) in a non-collinear optical parametric amplifier (NOPA) configuration [48], pumped by the frequency-doubled (515 nm), 800 fs pump pulses. The pump pulse, with a wavelength of 1030 nm, will also be provided optionally to the experiment. At the HED instrument, the PP-OL will be used for probing, pumping, and cross-correlation timing measurements with the X-ray beam.

Table 6-4. Operation modes of the PP-OL system

Mode	Repetition rate	Max. energy/pulse [mJ]	Pulse duration	Wave-length [nm]	Spectral bandwidth [nm]	Pulse-on-demand
I-a	10 Hz burst / 1–4.5 MHz intraburst	0.2	In steps: 15, 30, 50, 100 fs	~ 800 nm	~ 60	Yes
I-b	10 Hz burst / 200 kHz intraburst	5	< 20 fs	~ 800 nm	~ 60	Yes
II	10 Hz burst / 200 kHz intraburst	100	0.8 ps or 0.5 ns	~ 1030 nm	~ 3	Yes

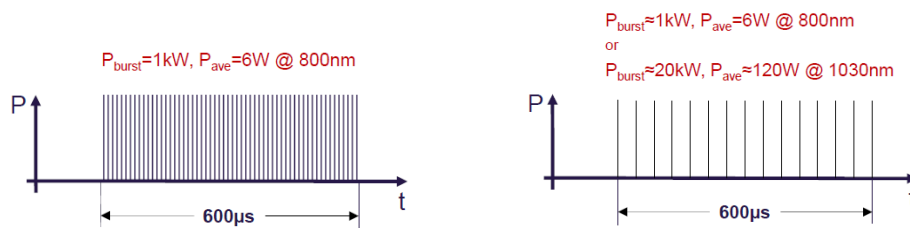


Figure 6-1. PP-OL delivery patterns according to Modes I-a (left) and I-b (right)

PP-OL as an optical probe

The frequency of the X-ray FEL radiation will lie above the plasma frequency of all possible densities that can be created, so the X-ray radiation can penetrate a sample and heat it uniformly to create well-defined conditions. The PP-OL can be used to probe such states. The extremely short temporal duration (15 fs) and precisely controlled delays allow dynamically changing processes to be probed with high temporal resolution. Some examples of application are listed in the following sections.

Reflectometry, polarimetry

Time-resolved measurements of both reflectivity and phase for different polarizations give insight into the optical properties of a heated sample, i.e. conductivity. The *s*- and *p*-polarized reflectivity and *s*–*p* phase difference can be determined by installing appropriately oriented polarizers or waveplates [49]. These measurements provide useful complementary information about the transition from solid to plasma phases.

Shadowgraphy, interferometry

When samples are irradiated by a high-power laser, they are heated, ionized, and expanded. Shadowgraphy (or Schlieren) measurements or interferometry allow the critical density layer of an expanding plasma to be defined with a temporal resolution given by the probe pulse duration. This method can also serve as a test bed for temporal contrast verification for the high-intensity femtosecond laser beam by measuring the interaction surface.

Fourier domain interferometer (FDI)

A Fourier domain interferometer (FDI) [50] enables both the amplitude and the phase of the complex reflection coefficient of an excited solid to be measured with high spatial and temporal resolution in a single shot. These quantities are closely related to both the optical properties of the probed sample and its hydrodynamic evolution. Optical properties are determined by the electronic structure (band structure) of the sample, as well as “fluid” parameters (electron density, temperature, and damping frequency). The comparison of the hydrodynamic evolution using hydrocodes allows the absorption coefficients, the equation of state, and the transport coefficients of the target to be tested. For these reasons, FDI-based diagnostics have been routinely used in OL pump–probe experiments. A first experiment was performed at LCLS, demonstrating the feasibility of FDI measurements in an X-ray FEL environment. Such a technique will also be a powerful tool to study the new regime of matter at high energy density created by X-ray beams, where the pump energy is deposited in the core electrons.

As shown in Figure 6-2, this technique relies on using a linearly chirped optical pulse, giving a univocal relation between the instantaneous frequency and time to encode the pulse spectrum with the time history of the perturbation. After reflection on the sample, the interaction point is imaged on the entrance of an interferometer (typically a Mach-Zender type). The two beam wavefronts are slightly tilted and shifted such that perturbed and unperturbed regions of the probe beam can interfere. The entrance of the interferometer is image-relayed on the entrance slit of a spectrometer. A high dynamic range camera records the spectrum.

The development of an FDI system for the European XFEL is foreseen to be realized in collaboration with Centre Lasers Intenses et Applications (CELIA) in Bordeaux, France. Few- μm and sub-100 fs resolution are envisaged. Following initial assembly, characterization, and test measurements, the FDI setup will be permanently installed at the HED instrument.

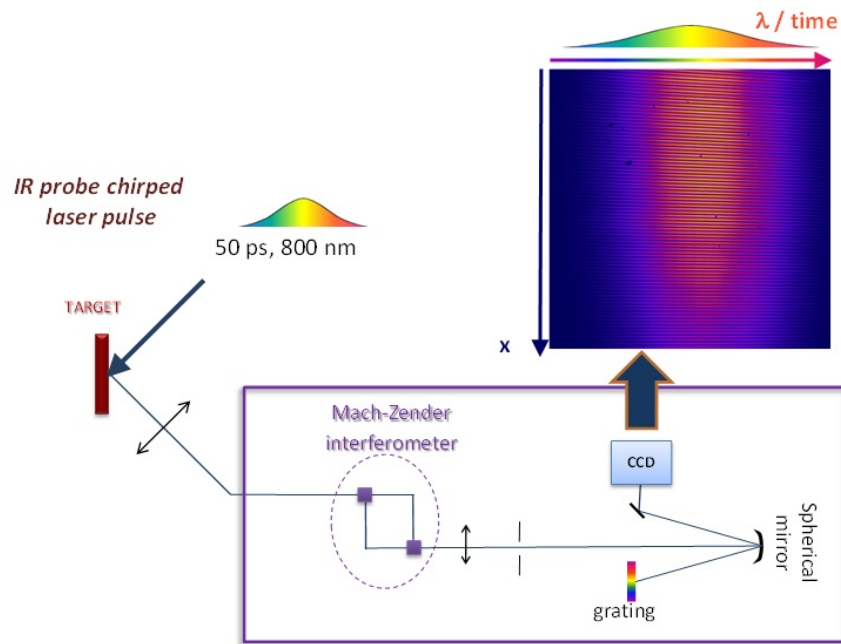


Figure 6-2. Schematic layout of FDI diagnostic system

Initiate heating, melting, and phase transition of solids (OL pump)

Using the PP-OL as a pump pulse and the X-ray FEL pulse as a probe, several powerful means exist to observe temporal changes of the electronic structure of a sample, as is briefly described in Section 3.1, “Condensed matter at extreme excitation”. By tuning the OL energy, pulse duration, or spot size, the excitation state can be controlled.

X-ray pulse diagnostics – time domain

Perfect synchronization between the X-ray FEL and OL pulses is crucial for femtosecond time-resolved pump–probe experiments, in particular when considering timing and arrival jitter as well as drift of the laser delivery. The current concept for temporal synchronization is summarized in Section 6.8, “Laser synchronization and diagnostics”.

Requirements for PP-OL

The PP-OL requirements can be divided into a main and an optional case.

Case I: Very short pulses (in steps: 15, 30, 50, 100 fs) at 800 nm with the option to generate second-harmonic (SHG: 400 nm) and third-harmonic

(THG: 266 nm) radiation for applications requiring shorter wavelengths. All beam delivery optics will have to be adapted to the wavelength. Jitter and temporal overlap management with respect to the X-ray beam is mandatory to achieve adequate time resolution for experiments. This calls for a thorough treatment of dispersion and non-linearity to provide the shortest pulse duration on the sample inside the interaction chamber. For some experiments, the initial pulse duration will be stretched to 1–10 ps while maintaining the broad spectrum (e.g. FDI). A motorized sub-micrometre resolution delay unit for the pump–probe time scan is necessary.

Table 6-5. Requirements to PP-OL beam delivery for various applications

Purpose	Laser energy	Pulse duration	Other
Reflectometry	< 1 mJ	15 fs (shortest)	<i>p</i> -/ <i>s</i> -polarization 2ω
FDI	~ 1 mJ	100 fs – 10 ps	2ω
Excitation	Variable	Short	—
Synchronization with FEL	~ 1 μ J	Short	Supercontinuum generation

Case II (optional): Long pulses in the range of either 800 fs (compressed) or 500 ps (uncompressed) with highest possible pulse energies up to 100 mJ (200 kHz), 1030 nm wavelength will be available on option.

6.3 100 TW ultrahigh-intensity short-pulse laser system (UHI-OL)

Applications

The scientific applications of using 100 TW–class high-power femtosecond laser pulses (UHI-OL) were summarized in Chapter 2, “Introduction and overview”. In brief, the laser intensity above 10^{18} W/cm² on sample pulls electrons immediately away from the parent atoms and injects them into matter with relativistic energies (> MeV). The resulting current density can exceed 10^{12} A/cm². The propagation of these huge currents through solids (so-called hot electron beam) is influenced by dynamically changing resistivity

and self-generated electric (\geq TA/m) and magnetic fields (\geq 100 MG). The fundamentals of hot electron transport have not yet been elucidated due to a lack of appropriate diagnostics with sufficient temporal and spatial resolution. At the HED instrument, the high-brightness, short-pulse X-ray FEL radiation will be used as a unique probe beam to unravel the associated physics of extreme currents in a solid-density plasma. The fundamental understanding of the microscopic process is of general interest, while the generation and transport of hot electrons have their own application, e.g. for the fast-ignition scheme for inertial confinement fusion (ICF). A secondary application could be the use of laser-induced ions for isochoric heating of samples to well-defined WDM states, which will be probed using the FEL beam.

UHI-OL system

The currently planned UHI-OL system is a short-pulse, high-intensity Ti:sapphire laser. This technology is based on chirped pulse amplification (CPA), which has matured over the last decades and is currently entering the petawatt power level. This technology is widespread in many laboratories and commercially available. Attainable pulse duration is 30 fs due to a large bandwidth of \sim 50 nm. Repetition rates up to 10 Hz can be achieved at 100 TW (\sim 3 J) systems.

The laser parameters are summarized in the following:

- 30–50 fs pulse duration after compression.
- 3–5 J energy on sample ($>$ 100 TW).
- Down to \sim 3 μ m focusing spot (FWHM) provides a focused intensity of $>$ 10^{20} W/cm². This focal spot size can be obtained using an off-axis parabolic mirror. Larger focal spot sizes can be achieved using a larger focusing mirror, or by moving out the focus and/or applying an arbitrary phase with a deformable mirror.
- 800 nm central wavelength with a spectral width according to the pulse duration ($\Delta\lambda \sim$ 50 nm).
- 10 Hz pulse repetition rate.
- 80–100 mm beam diameter before focusing; optics should have at least 120 mm clear aperture.

The laser chain consists of an oscillator, which will be optically synchronized to the main clock of the European XFEL. The pulses are temporally stretched, amplified, and finally re-compressed. Temporal stretching and compression are accomplished with dispersive elements. One important aspect is to obtain a high temporal contrast. Due to the very high laser intensity ($> 10^{20}$ W/cm²), the temporal contrast ratio must be higher than at least 10^8 (pre-pulse intensity: $< 10^{12}$ W/cm²) to suppress pre-pulse or amplified spontaneous emission (ASE) radiation. This radiation would itself lead to plasma formation, thereby preventing experiments from being performed in a well-controlled manner. In addition, the pre-plasma leads to more efficient MeV electron generation in a non-controlled manner. Temporal contrast control and proper monitoring are thus very important. Many techniques for contrast improvement have been demonstrated, and some of them are quite mature. They include fast pockels cells, saturable absorbers, and cross-polarized wave generation (XPW). All require sensitive diagnostics to measure and control the spectral phase. Recently, a temporal contrast of more than 10^{10} has been demonstrated for a CPA laser [51].

Room size, infrastructure requirement

The 100 TW Ti:sapphire laser system will occupy several optical tables, in total about 17 m². In addition, the pump lasers and the compression chamber (outer dimension $\sim 3 \times 4$ m² or less, to be determined) must be placed nearby. Together with floor space for the laser operators, a floor space of the order of 60 m² is needed. The laser room should be designed as a clean room (Class 100) with controlled temperature ($21 \pm 0.1^\circ\text{C}$) and humidity ($45 \pm 2.5\%$). Power cables for the pump lasers need to be as short as possible while avoiding huge heat loads in the laser room. Therefore, the power supplies will be installed inside the first HED rack room (HED-RK1) room, which will be located right next to the HED-LAS room. The cable length can thus be minimized. Cooling water will also be provided for the pump laser heads.

Table 6-6. UHI-OL infrastructure requirements based on the DRACO laser system at Helmholtz-Zentrum Dresden-Rossendorf (HZDR), Germany (150 TW, ~ 4 J, 25 fs duration, Ti:sapphire)

Purpose	Type	Requirement
Front end	Space	1 table 1.7 × 2.3 m ² + 1 table 1.5 × 4.3 m ² , 2 external pump lasers “ProPulse” 2 m ²
Amplifier	Space	1 table 1.5 × 4.3 m ² , 8 external pump lasers “ProPulse” 8 m ² , heat removal with 1 He-cooled cryo head
Compressor	Space	3 × 4 m ²
Electricity	Resource	~ 70 kW
Power supply	Racks	1 rack for the front end, motor, and vacuum control, 4 racks for pump laser. (32 HE in 1 rack are assumed. Rack size is 19 inch. 1 HE = 7/4 inches)

6.4 100 J nanosecond high-energy laser system (HE-OL)

Applications

The energetic nanosecond-duration pulse of the HE-OL will be used to drive shocks and shock-less compression in samples. The difference between these types of applications lies primarily in the temporal pulse shape. While shocks use Gaussian pulses of around nanosecond duration, for shock-less or ramp compression, specific temporal profiles have to be used (see Figure 6-3). In general, the laser is focused onto an ablator layer deposited on the target. Material will be ablated, and the ablation pressure is transmitted into the target. Compared to diamond anvil cells, dynamic compression techniques can attain much higher pressures, and they allow studies of strain rate dependencies. In shock compression, a sudden increase of ablation pressure launches a shock wave into the target. To obtain a certain pressure, a relatively large amount of energy is transferred into heat, because the sudden shock expels atoms more than they would require to reach their new

equilibrium positions. The laser pulse must have a steep increase to create a good shock; the duration must be adequately long so that the pressure release / rarefaction wave does not overtake the compression wave. In ramped compression, the ablation pressure increases continuously. The material remains much colder compared to shock compression, and higher pressures can be obtained. However, the overall pulse length is typically longer than for shock compression, and the capabilities of the laser system are less well exploited.

The pulse shape depends on the pressure to be reached, but even more on the material, its phase diagram, the thickness of the sample, and the size of the laser beam. Several conditions link the pulse energy, beam size, and sample thickness. Samples will in general be tamped between two layers of a material transmissive to OL radiation. These layers will avoid hydrodynamic motion of the sample occurring too soon. As a rule, the beam size R on the sample for ramp and shock compression should be three, resp. two times the total thickness D (see Figure 6-3). The following relations for maximum pressure can be found [14]

$$P [\text{GPa}] = 42 (\pm 3) (I [\text{TW}/\text{cm}^2])^{0.71(0.01)} \quad \text{for}$$

$$I [\text{TW}/\text{cm}^2] = E [\text{J}] / (\Delta t [\text{ns}] \pi R^2 [\mu\text{m}^2]) \times 10^5$$

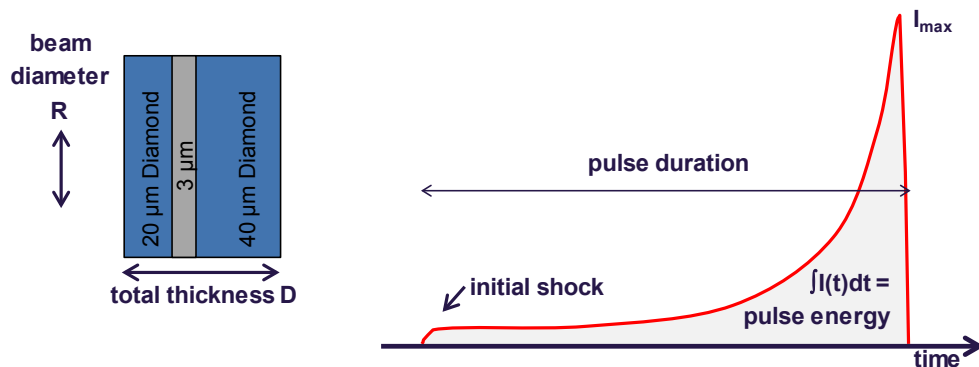


Figure 6-3. Sample geometry (left) and temporal pulse shape definitions (right) for dynamic compression experiments

HE-OL system

This laser will typically be focused by a large lens and pass through a random phase plate to obtain a smooth, flat-top-like focus of $R \sim 100\text{--}500\ \mu\text{m}$ diameter. Frequency doubling ($\lambda_L \sim 500\ \text{nm}$, 2ω) or tripling is required for most of these experiments for several reasons: (1) Generation of undesirable hot electrons, which pre-heat the matter, scales with laser wavelength $1/\lambda_L^2$. (2) High temporal contrast is required to avoid pre-heating, and frequency doubling gives higher contrast. (3) At shorter wavelength, absorption occurs at higher densities due to higher critical density. This can lead to a higher pressure (momentum of the ablated material). The drawback of frequency conversion is a loss of pulse energy. A realistic conversion efficiency from 1ω to 2ω using beta barium borate (BBO) or potassium dihydrogen phosphate (KDP) is typically of the order of 70%.

Several technologies have been scouted. In the following, we use parameters of a National Energetics Nd:glass flashlamp-pumped laser, which can provide 150 J laser energy at 1057 nm wavelength. The pulse duration will be variable between 2–20 ns. A repetition rate of 1–10 Hz can be provided, limited by the heat removal capability from the disk amplifier. The minimum temporal duration is limited by the requirement to avoid B-integral beam degradation, which eventually scales with the amplifier disk size. After the final amplifier, a BBO crystal will be used to convert the 1057 nm wavelength to the 523 nm second harmonic with $\sim 70\%$ conversion efficiency.

Room size, infrastructure requirement

At present, we have a detailed requirement only for a 150 J Nd:glass flashlamp-pumped system. This system can be installed on a $\sim 1.2 \times 2.5\ \text{m}^2$ optical table and will require five 19-inch standard-size racks for the capacitor banks and pulse-forming networks that drive the flashlamps. One more rack will be required to install several cooling groups, the flashlamp chargers, and a control unit. The requirements of temperature and humidity to the laser room are similar as for the UHI-OL system. Power cables for the pump lasers need to be as short as possible. Therefore, the power supplies will be installed inside the HED-RK2 room, which will be located next to the

HED-LAS room. The cable length can thus be minimized. Cooling water will also be provided for the flashlamps.

Table 6-7. HE-OL infrastructure requirements based on a proposed laser system (150 J at 1057 nm wavelength, 2–20 ns duration, Nd:glass disk amplifier; courtesy National Energetics).

Purpose	Type	Requirement
Front end + disk amplifier + BBO	Space	~ 1.2 x 2.5 m ² optical table Shaped source + Nd:YLF front end and booster amplifier, flashlamp-pumped Nd:YAG disk amplifier, BBO crystal for frequency doubling
Electricity	Resource	~ 50 kW at 5 Hz
Power supply	Racks	4 racks for capacitor banks and drivers, 1 rack for cooling groups, flashlamp chargers and control unit (assuming 19-inch standard rack)
Clean room	Level	Better than Class 10000 or ISO 7

6.5 Additional laser systems

As additional lasers, several continuous-wave (cw) He–Ne lasers and laser diodes will be installed for optical alignment purposes. These lasers are classified as Class 2, which means very low potential laser hazard. At least one on-axis alignment laser for each system (UHI-OL, HE-OL, PP-OL, and X-rays) will be installed to simplify optics and diagnostics adjustment without laser or X-ray interlocks.

In addition, an additional Q-switch laser will be implemented for special optical diagnostics, as described below. These lasers are part of the baseline instrumentation.

Velocity interferometer system for any reflector (VISAR)

VISAR [52] is an optical reflection technique measuring the surface motion [53]. Typically, velocities in the range from few m/s to tens of km/s can be measured with sub-100 ps temporal resolution. The VISAR measurement is

based on an interferometric measurement, which relates the velocity to a fringe shift. Two VISAR arms are required to resolve the ambiguity of the fringe shift in case of a discontinuity in the velocity. By coupling a VISAR with a streak camera, the temporal evolution of the surface velocity can be obtained with 1D spatial resolution. VISAR is considered a fundamental diagnostic technique in dynamic compression experiments and is used to determine shock breakout times and shock velocity.

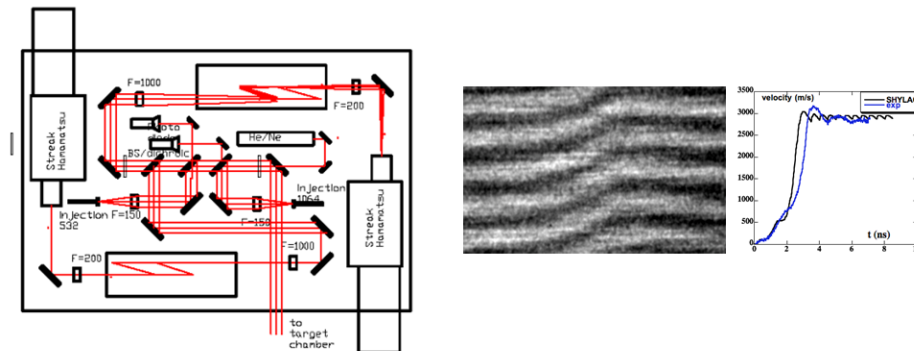


Figure 6-4. (Left) Schematic setup of the VISAR system installed at Laboratoire pour l'Utilisation des Lasers Intenses (LULI) in Palaiseau, France. (Right) Fringe pattern and velocity profile obtained with VISAR in isentropic experiments, courtesy E. Brambrink.

Requirement

In a VISAR application, a 10–50 ns duration probe laser pulse will be required. The long pulse duration is necessary to follow the temporal evolution of the velocity during long compression, which is needed to reach off-Hugoniot states. The required probe laser energy is typically at the mJ to 10 mJ level, depending on pulse duration. It will be useful to have different wavelengths for the probe beam and the driving laser, to efficiently filter diffused light from the driver laser. Lasers of this type are commercially available (for example, “Quanta-ray” Nd:YAG, Q-switch laser). The laser will be installed inside the experiment enclosure HED-EXP on the common laser table. Typical sizes for the VISAR system including the laser are $1 \times 2 \text{ m}^2$. Power consumption is of the order of 7 kW.

6.6 Future installation of high-energy laser systems

The long-term plan for upgrade of the laser systems beyond the initial installation in 2016 is reported at the beginning of this chapter. The laser room HED-LAS has a size of $\sim 110 \text{ m}^2$ and will not provide enough room for a several-100-TW UHI-OL system and a kJ HE-OL system. In addition, the electrical power and space requirements for power supplies may hit space limitations in the HED-RK1 and HED-RK2 rooms. It is therefore necessary to provide additional space for laser installations as part of the upgrade activity. In response to this requirement, the HIBEF UC has proposed to construct an additional building adjacent to the experiment hall, both of which will be connected by an underground laser tunnel. Figure 6-5 shows a schematic presentation of this building and the beam transport into the HED-LAS room.

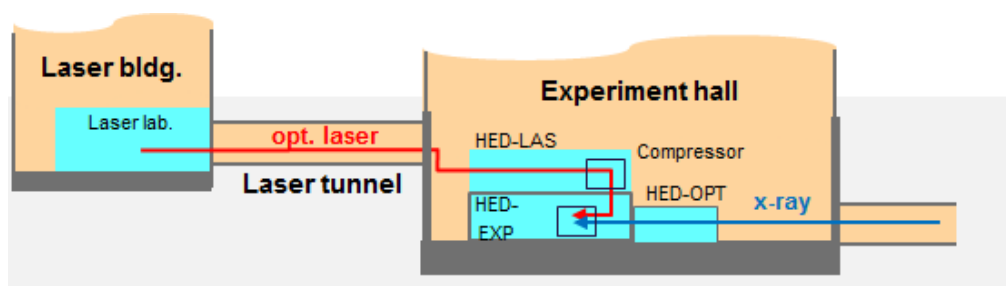


Figure 6-5. Schematic presentation of the laser building adjacent to the experiment hall XHEXP and of the laser beam transport from the laser tunnel, first into the HED-LAS room and then after compression to the experiment area.

Since HED-LAS is directly adjacent to HED-EXP, the final beam conditioning of the two laser systems will be provided in HED-LAS before transporting the pulses into the experiment enclosure. It has also been pointed out that the short-pulse system with its pulse compressor and vacuum beam transport system will benefit specifically from a short and stable beam transport. Details of how the available space will be used for the final amplification stages and beam conditioning for the two laser systems will have to be decided once a better-defined upgrade plan exists.

Proposed upgrade possibilities

The HIBEF UC proposed to provide a substantial laser upgrade including additional installations in a separate building. These apply to both the UHI-OL and HE-OL systems. These upgrades will require significant floor space and larger optics, including compressor gratings. The current concept is to install them into the external building. The detailed strategy and upgrading procedure with minimized downtime have not been clarified yet and will be subject to investigation in the next years.

Upgrade of the UHI-OL system. The simplest way will be an upgrade of the baseline 100 TW Ti:sapphire laser system to the PW level, i.e. 30 J / 30 fs. The repetition rate will be ~ 1 Hz. Another option would be to install a diode-pumped PW laser system with parameters in the range 150 J / 150 fs. Those systems are currently under development at partner institutions in the user consortium. The attainable regimes are slightly different from the Ti:sapphire system. The pulse duration will be longer, which implies lower temporal resolution in experiments, and the pulse energy will be significantly increased. The higher pulse energy leads to a much smaller tolerable repetition rate and to the necessity of providing local shielding close to or inside to the experiment vacuum chamber.

Upgrade of the HE-OL system. Depending on the initial HE-OL system, the upgrade to a $> \text{kJ}$ level could be as simple as adding more amplifiers on top of the initial installation. The repetition rate will however be lower due to more complex heat dissipation management. The choice of technology will have to be made in the coming years. Finally, one other proposal is to use the HE-OL laser as pump laser for the PW upgrade of the UHI-OL. This would mitigate congestion in the laser room, but will exclude simultaneous operation of UHI-OL and HE-OL.

6.7 OL beam transport

PP-OL transport

The PP-OL system (front end, amplifiers, and pre-compressor) is located inside the PP laser room (PP-LAS). From there, the laser beam will be transported to the SASE2-LAS room. This room is shared with the MID instrument and is dedicated to diagnosing the beam properties and optimizing the beam to fulfil specific user experiment requirements (chirp, frequency conversion, etc.). Distinct parts and components are currently undergoing evaluation in close collaboration with the Optical Lasers group and are therefore subject to change. Figure 6-6 illustrates a possible table layout for PP-OL in SASE2-LAS. The beam will be delivered through the vacuum pipe to avoid dispersion in the air (vacuum level: 1–10 mbar is sufficient for this purpose).

Case I ($\lambda = 800$ nm, up to 5 mJ, 15 fs). The OL beam will be picked up using a moveable mirror. After relay imaging, it will be divided into one arm for measuring the temporal cross-correlation with the X-ray beam and a second arm for pump–probe applications. The attenuator/splitter ($\lambda/2$ wave plate and thin-film polarizers) permits a continuously tuneable energy splitting. This detail is currently subject to evaluation as polarizers might introduce parasitic chirp, thus preventing the shortest pulses. Reflective optics can be used as an alternative. Delay Line III (see Figure 6-6) is responsible for pump–probe scanning, whereas Delay Line I and the optional Delay Line II are quasi-stationary translations to compensate path differences between pump–probe and temporal overlapping arms. Such path differences might occur when changing the instrument setup for different experiments. To ensure that the laser beams for pump–probe and temporal cross-correlation applications can be individually selected, they are launched into separate delivery pipes at the entrance to the HED-OPT hutch.

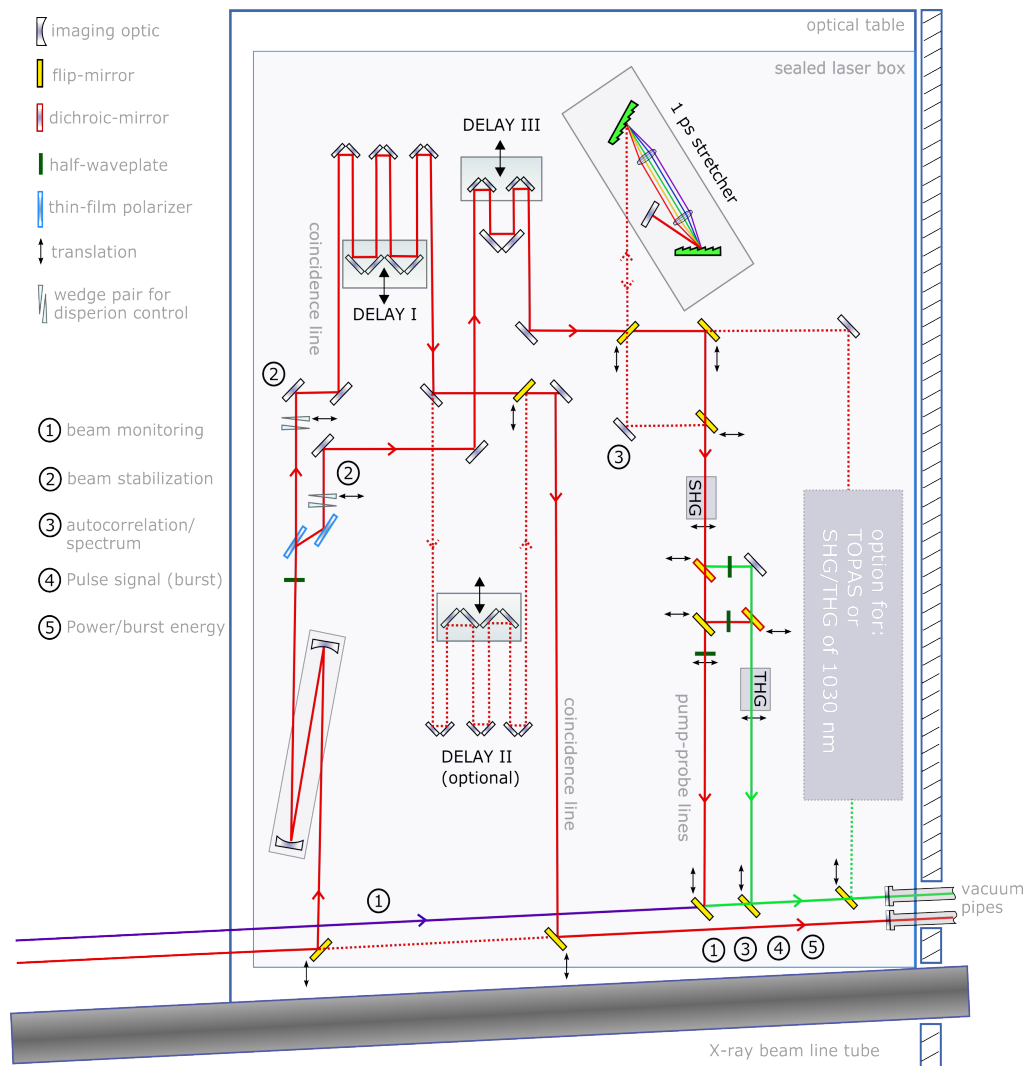


Figure 6-6. (Top) Overview of the PP-OL laser transport (red line). The blue line indicates the X-ray beam. The PP-OL is located inside the PP laser hutch, which delivers the beams into the SASE2 laser hutch. (Bottom) Schematic drawing of the optical setup inside SASE2-LAS (corresponds to the green square of the upper drawing). Red beamline: 800 nm, 15–100 fs short pulses. Purple beamline: 1030 nm long pulses (0.8 ps or 0.5 ns) with high energies. Green beamline: optical path for multiple wavelengths (SHG = second-harmonic generation, THG = third-harmonic generation). Courtesy G. Palmer (WP78)

Displaceable second- or third-harmonic generation (SHG, THG) units offer frequency conversion, and wave plates ($\lambda/2$, $\lambda/4$) serve as polarization control units for the actual experiment. All reflective mirrors must be equipped with zero-dispersion coatings for the respective wavelength operation regime. In

the current design, the laser is negatively chirped to 30 fs pulse duration at the entrance of SASE2-LAS. Its dispersion is conjugated to fused silica. By propagating through fused-silica components with pre-determined length, the beam will be compressed to the 15 fs bandwidth limit (reached inside the chamber after the entrance window). The fused-silica “budget” will be on the order of 30–40 mm length. A pair of fused-silica wedges will make fine-tuning possible.

Case II ($\lambda = 1030$ nm, up to 100 mJ, 800 fs). This setup places much lower constraints on dispersion due to narrow bandwidth. On the other hand, mirrors are needed to supply sufficient damage thresholds. In Figure 6-6, the purple line represents the optical path of the long pulses at 1030 nm. Optional SHG, THG, and polarization control units may be placed next to the short-pulse setup. The numbers in Figure 6-6 stand for monitoring and control locations where pulse properties should be analysed and corrected if appropriate. Some of these observation points are locally flexible, whereas others might have to be fixed (i.e. beam stabilization in red line after delay lines).

The assembly will be mounted on an optical table that is mechanically damped and possibly passively stabilized against thermal drifting. A sealed box will protect the setup from any potential external disturbances. The beam delivery pipes will not hold any mirror mounts (purely transmitting) and will be decoupled from the optical configuration to ensure maximum stability. The design is regarded as an initial system and further extensions may be added at a later stage. Possible changes could include simultaneous operation of different pulses (length, wavelength, spectra, beam size, etc.).

UHI-OL beam transport

The HED laser room (HED-LAS) is situated on top of the experiment hutch (HED-EXP). The pulse compressor will be located inside HED-LAS. After compression, the 100 TW–class UHI-OL beam must be transported under vacuum of 10^{-3} mbar or better. Because of the relatively large bandwidth of the laser, the optics should be non-dispersive, thus beam transport and focusing must be accomplished with mirrors. The mirror coatings have to accommodate the broad bandwidth of 750–850 nm and the high fluence.

Currently, the south port of the experiment chamber is foreseen as the beam entrance. At least one planar mirror will be installed inside the chamber to steer the beam on an off-axis-parabola (OAP) focusing mirror. At least two different positions for the OAP are foreseen for different directions of the OL beam axis with respect to the X-ray beam (collinear and perpendicular). Regarding the focal distance, short and large focal lengths are foreseen to achieve tight and medium focusing. An $f/3$ OAP (focal length ~ 30 cm) will produce a spot of down to ~ 3 μm , and an $f/7$ OAP (focal length ~ 70 cm) will produce a spot of ~ 10 μm on sample.

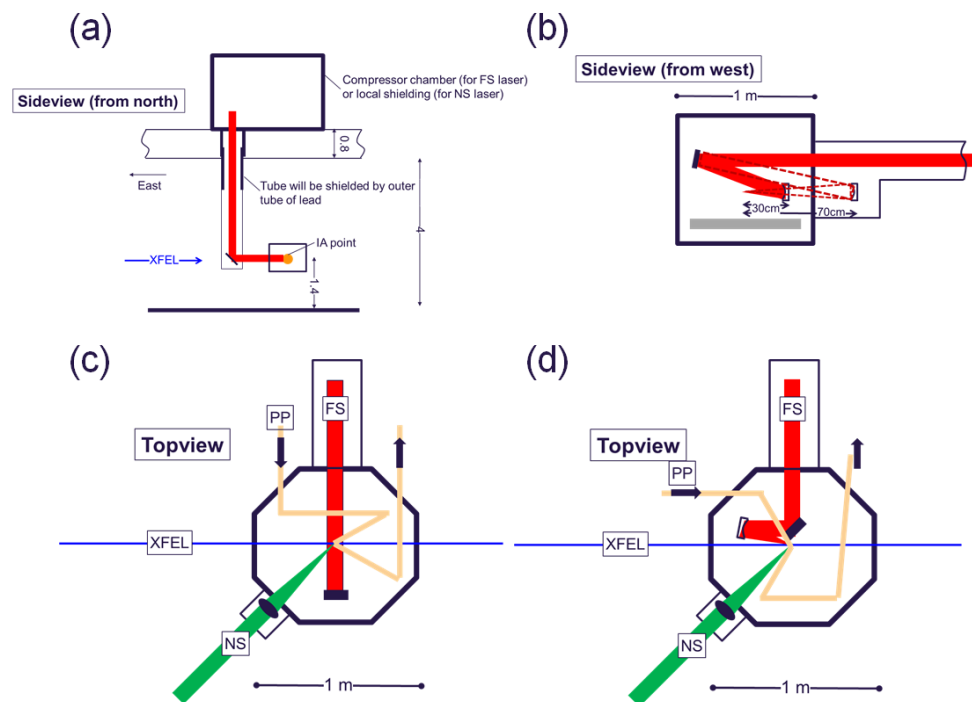


Figure 6-7. Several examples of focusing geometry

HE-OL beam transport

Like the UHI-OL, the HE-OL system (front end, amplifier) will be located inside the HED-LAS room. The HE-OL beam will be brought down through a hole in the concrete floor of HED-LAS to the experiment floor. Due to the long, nanosecond pulse duration, the intensities are a few orders of magnitude lower than for the UHI-OL. Thus, the beam transport could in principle be done in air, because beam breakup in air will not be an issue. However, airflow must be avoided and dry gas at atmospheric pressure is also recommended. This would imply some tubing around the beam. Refractive and reflective

optics can be used because of the narrow bandwidth. But optical damage risk, which is typically described by the fluence (J/cm^2), needs to be properly evaluated. Mechanical stability is rather relaxed since the beam is typically focused to a large spot, typically larger than $100\ \mu\text{m}$. Hence, a small angular jitter does not seriously affect the spot position. The laser will be focused by a lens and pass through a random phase plate to obtain a smooth, flat-top-like focus of $R \sim 100\text{--}500\ \mu\text{m}$ diameter. Frequency doubling ($\lambda_L \sim 500\ \text{nm}$, 2ω) will be done using the BBO crystal before focusing.

6.8 Laser synchronization and diagnostics

It is crucial to deliver the OL and X-ray pulses with a high precision in relative timing, since fluctuations of their delay will lead to indistinguishable experimental results. A precise timing measurement and feedback to stabilize the system are therefore required.

Synchronization concept

The establishment of a timing accuracy on the order of 10 fs between the OL and X-ray pulses at the sample location is requested for applications using the PP-OL and UHI-OL systems. For the HE-OL, a resolution of a few picoseconds or maybe longer should be sufficient. In a first step, all laser systems will be synchronized using a distributed radio frequency timing signal. In addition, a fibre laser signal will be distributed throughout the European XFEL to synchronize with highest precision all time-critical components of the facility—from the injector, to the accelerator components, to the lasers in the experiment hall. This synchronization is designed to reach a precision of better than 20 fs, but its performance will largely depend on how the fibre laser signal is connected to the respective component. Using this synchronization ensured that the different subcomponents “tick” at the same time. In addition, delays due to optical path and timing jitter of the various components have to be considered. Therefore, in a second step, the PP-OL will be cross-correlated with the X-ray pulse arrival. This measurement will be done for each single pulse, and the corresponding value will be applied to correct the expected delay between OL and X-ray pulse at the sample

location. In addition, a cross-correlation measurement of the UHI-OL and PP-OL pulses is necessary, yielding a second correction value to be applied to the expected delay. The measurement value will be recorded on a shot-to-shot basis.

Cross-correlation of PP-OL vs. X-ray arrival

The X-ray–OL timing tool will be located 960 m from the source and 10 m in front of the sample inside HED-OPT. Several techniques have been investigated over the last years. With the current state of knowledge and for the requirements of the HED instrument, we propose to employ a spectrally chirped OL pulse for the cross-correlation measurement of the arrival of the X-ray pulse. This method has been developed and improved at LCLS and DESY [54, 55], and relies on the changes of optical properties induced when an intense X-ray pulse is transmitted through a thin film. The chirped continuum reference pulse then probes the transiently changing optical refractive index. Changes are encoded in the transmitted probe spectrum and are measured using a spectrometer. This method provides a nearly in situ single-shot measurement of the X-ray arrival time relative to the reference OL pulse.

The energy required for the reference laser beam would be only a small fraction of the total PP-OL pulse energy, therefore allowing simultaneous measurement. The X-ray intensity, however, has to be relatively high, since the target material needs to be driven near the damage threshold in order to show strong cross-correlation signals. However, it has been shown that non-destructive and shot-by-shot measurement is feasible at least at 10 Hz repetition rate. To establish this diagnostic tool for measuring each X-ray pulse at high repetition rates of up to 4.5 MHz, more R&D is required. The development and implementation are an R&D issue for all scientific instruments at the European XFEL, and will be worked on by all instrument groups, the Optical Lasers group (WP78), and the X-Ray Photon Diagnostics group (WP74). They will be as standardized as much as possible.

Cross correlation of PP-OL vs. UHI-OL

As a unique requirement for the HED instrument, the UHI-OL system needs to be well synchronized with X-ray and PP-OL too. The current concept uses a temporal cross-correlation measurement with the PP-OL pulses. This implies that even in experiments not using the PP-OL on sample, the temporal overlap of the UHI-OL will rely on the PP-OL–X-ray synchronization. Details of this complex procedure still need to be refined. This synchronization will be done inside the experiment hutch. A streak camera or photodiode will provide a coarse overlap between the OLs. Optical cross-correlation, through second-harmonic generation or optical fringe visualization, will eventually give a precision of less than the individual pulse duration.

7 Interaction chambers and ancillary instrumentation

This chapter introduces the current concept of the setup inside the HED experiment room HED-EXP (see Chapter 8, “Experiment hall layout”). We foresee to place three interaction chambers for high-resolution, high-energy, and pulsed-magnet experiments. These interaction chambers (IA1, IA2, and IA3) are mounted along the X-ray beam at distances of 2.5, 5, and 7.5 m from the east entrance wall, respectively. All chambers will be connected by vacuum tubes, but at least the IA3 chamber can also be removed from the straight beam path. In addition, any mount inside the chambers can be moved out of the beam path in order to either deliver the beam to the sample in the following chamber or investigate the transmitted and forward-scattered X-ray beam at the monitor station. An area detector mount will be located as close as possible to the beam stop. This mount can be used for either area detectors for SAXS- or XI-type experiments, or monitors for intensity or spectrum. The three interaction chambers have different functions, which are described in the following sections. It is considered that the high-resolution chamber (the one located 2.5 m from the wall), the intensity/spectrum monitor, the detector mount, and the beam stop will be built as part of the HED baseline project. The other two chambers will be provided at a later time by the HIBEF UC. On one side of the interaction chambers, the OL beams are prepared and distributed. The other side allows for access to the chambers.

Experiment preparation will have to be done during short periods of either one to two days, during three- to four-week-long experiment runs, or during longer breaks of four to five days in weeks between the experiment runs. These short time periods lead to the requirement of efficient setup and quick alignment procedures. The three-chamber concept will allow for dedicated and (quasi-)permanent experiment configurations. In addition, at least for the smaller chambers, it is considered to use pre-configured experiment platforms

that may be exchanged as a whole assembly. In this way, easier and much faster swapping of experiments will be possible.

The advisory review team (ART) commented that the three-chamber concept would potentially produce an extremely crowded workspace in HED-EXP. A zone of at least 0.6 m around the IA chambers should be foreseen for mounting and placing additional instrumentation. Several options to relieve the congestion in HED-EXP will be investigated: reducing the number of chambers, placing permanent optical diagnostics such as VISAR and FDI inside HED-LAS, and others. An updated concept will be established for the TDR.

In the chambers IA1 and IA2, sample stages will be used to orient, translate, and replace solid samples at repetition rates of up to 10 Hz. Experiments operating at higher X-ray delivery rates either use quickly replenished gas, liquid jets, or solids in cases where fast (< 200 ns) sample recovery takes place. High repetition rate solid-sample delivery is a challenging task described in Section 7.4. The instrumentation of the interaction chambers also comprises various spectrometers and detectors, which are described in the final two sections of this chapter.

7.1 High-resolution interaction chamber (IA1)

The IA1 interaction chamber will be mounted at a distance of ~ 2.5 m from the east entrance wall. This chamber will be used for experiments requiring the tightly focused X-ray beam, and will offer the use of the ~ 100 TW UHI-OL and the ~ 100 J HE-OL laser beams as well. In this chamber with approximately 1 m diameter, space limitations may not allow the use of large-diameter laser optics, which will make the use of higher-energy pulses (i.e. PW-fs laser, kJ-ns laser) very difficult. Additional laser beams (e.g. Quanta-Ray Q-switch laser) for the purpose of sample diagnostics (e.g. VISAR) will be used in this chamber.

An X-ray focal length of 7 m using the CRL3 system produces a $1\text{--}3$ μm X-ray focal spot size (see Table 5-3 on page 80). In addition, further studies will be performed to investigate the possibility to implement a sub-mm focusing

system with even shorter focal length. In this case, the CRL must be located inside or at least very close to the interaction chamber. Smaller foci will require higher stability of the CRL with respect to the sample position, which may be achieved by using a common optical bench supporting the CRL and the sample mount. In order to increase the stability and minimize the influence of vibrations, the sample mount, or even a complete optics platform, will be mounted inside the chamber in such a way that it will be vibration-decoupled from the chamber itself. In this way, vibrations generated by vacuum components and other instrumentation connected to the chamber can be decoupled from the sample setup. This platform should provide enough space for the sample mount and for the last mirrors of the UHI-OL delivery and the diagnostic lasers. It will be investigated whether such a platform could e.g. be dedicated to experiments using only collinear or perpendicular experiment geometries. The HE-OL is much less critical due to the larger beam size on sample with relatively long focal distance. It is considered to mount part of the spectrometers and detectors on the outside flanges of the chamber. In practice, flanges at selected angles with respect to the incident beam will be welded to the chamber. A large access door on at least one side will allow work to be done on parts of the sample mount and optics, or the entire optics platform to be removed and exchanged. The chamber should enable UHV operation with pressures allowing ion pump operation ($O(10^{-7}$ mbar)).

7.2 High-energy interaction chamber (IA2)

This larger chamber, with a diameter of ~ 2 m, will be dedicated to experiments using the highest-energy pulses delivered by the UHI-OL (few 100 TW – PW) and the HE-OL (~ 1 kJ) as the final deliverable of the HIBEF UC. The chamber would provide the instrumentation to perform related experiments, e.g. generating ultrarelativistic plasma–solid interactions or high-field effects using the UHI-OL, or extremely high-pressure experiment beyond TPa. The major differences are the larger optics to avoid damage during beam compression, transport, and focusing. This chamber will be provided by the HIBEF UC.

Examples exist for such chambers at large laser facilities, but also at the Matter in Extreme Conditions (MEC) instrument at LCLS. Their advantage is the open space of nearly 1 m radius around the sample location, which can be used for varying setups. A disadvantage is that setups usually need to be completely removed and rebuilt, which takes a considerable amount of time. Specification of this chamber will be done in collaboration between the HED group and the HIBEF UC.

In the current concept, the centre of the chamber will be located approximately 5 m from the east wall, and another 5 m beam path is available to the area detector mount. This distance should allow for the SAXS-type experiments that have been proposed. Focal spot sizes of a few micrometres to a few tens of micrometres will be available.

7.3 Pulsed magnetic fields chamber (IA3)

The third chamber will be dedicated to high magnetic field (> 30 T) experiments. The exact geometry of the scattering setup still has to be defined, but recent developments for synchrotron radiation sources are very promising and could be easily transferred. Vacuum is required since X-ray windows at small spot size need to be avoided and since the samples are cryogenically cooled. The experiment will require an X-ray spot size of typically a few 100 μm , enabling the chamber to be installed far from CRL3. In the current concept, the chamber will thus be installed last in the row. The reduced X-ray fluence will provide the opportunity to avoid heating or melting of the samples, thus allowing highly repetitive experiments. But the magnetic pulser itself will have a much lower repetition rate, on the order of 1 Hz (in case of mini-coil) or even much lower. Currently, it is not anticipated that this chamber will receive an OL beam. Removal of the chamber from the X-ray beam path provides forward scattering angles and additional space for instrumentation for the IA2 setup.

7.4 High repetition rate sample delivery

Laser–solid target interaction experiments at repetition rates > 1 Hz require precise, reproducible, and automatized sample placement. Typically, samples are extended 2D layers deposited or fixed on a kind of grid providing mechanical stability. The sample thickness is usually defined by experiment requirements originating from the OL or X-ray beams, and values are much smaller than for bulk samples. These sample grid structures will be mounted on an x – y translation stage and rastered over the X-ray focus. Approaching 10 Hz repetition rate, such rastering is already quite challenging, in particular when considering the high precision of the sample positioning along the X-ray or OL beams required to stay inside the focus. Issues like vibration of the sample due to the high accelerations required for fast placement need to be analysed. In order to ease alignment and adjustment and to facilitate operation of a large number of such grids, a well-defined referencing system for the sample grid will be developed. An alternative to rastering of a grid is the use of tape targets, as developed for high repetition rate laser experiments and used recently for laser-based X-ray generation.

Challenges include more than just refreshing the sample, however. The sample needs to be repositioned with respect to the two beams (X-ray and OL) with very high accuracy, typically a few μm or less. In general, three degrees of translation (x , y , z) and two degrees of rotation (θ , ϕ) are needed.

Considering sample grids of 500 μm pitch, a two-inch wafer with a sample area of about $35 \times 35 \text{ mm}^2$ would correspond to ~ 5000 sample positions. Using 1 Hz operation, such a sample could be completely rastered within two hours of beamtime, for 10 Hz within a fraction of an hour. Thus, it becomes clear that rapid exchange of such sample grids is paramount to the efficient operation of the instrument at high repetition rate. Exchange techniques not requiring the breach of vacuum conditions will be most efficient and will be investigated.

It will be the task of the coming months to develop such a sample stage for the HED instrument. This development will be done in close collaboration of

the HED group, the Sample Environment group (WP79) at European XFEL, the HIBEF UC, and the partners involved.

Not discussed here, but equally important, is the development of 2D layered samples for the science proposed for the HED instrument. Together with the scientific community, an effort has to be made to develop new schemes and establish new and affordable sample fabrication methods.

7.5 Detector requirements

In Chapter 4, “X-ray techniques and requirements”, several methods of X-ray scattering to be implemented at the HED instrument are introduced. Several of these methods require direct detection of the X-rays scattered by the sample, e.g. XRD, SAXS, XPCS, XI, etc. Other methods use photon energy resolution, which, at pulsed single-shot sources, leads to the requirement of involving spectrometers. Selected aspects for spectrometers will be discussed in the next section.

X-ray detectors at the HED instrument will have 0D, 1D, and 2D dimensionality. Typical detector time scales are picoseconds to nanoseconds for charge collection and nanoseconds to seconds for readout and data transfer. In general, it is considered to use only time-integrated detector signals. An exception could be the implementation of an X-ray streak camera provided by the HIBEF UC. Slow readout and data transfer is a particular issue for 2D systems. The requirements to dynamic range will have to be analysed carefully for the various applications. However, due to the aim of providing maximum information in a single shot, a high dynamic range will be of great advantage. Detectors should ideally cover the entire photon energy range of 3–25 keV provided at the HED instrument. It is understood that this requirement cannot be paired with constant high performance over the entire range. A further issue is the proximity of high laser fields to the detectors. Electromagnetic pulses (EMP) can raise serious issues and cause potential breakdown of complex electronics. These issues will be considered for the requirements to X-ray detectors for the final implementation.

0D detectors

The 0D detectors provide a signal integrating over a defined space angle. The main application in the experiment area might be to obtain space-, time-, and spectrum-integrated signals for normalization and overview. Filters could be applied to improve the spectral response.

1D detectors

The 1D detectors will be particularly important for MHz repetition rate experiments, since they provide both spatial information and high repetition rate. These detectors are much simpler and much less costly than 2D detectors operating at similar frame rates. Their implementation in spectrometers is thus an interesting alternative to the usually employed 2D detectors, which provide higher spatial selectivity in the detector plane. The spectrum monitor described in Chapter 4, “X-ray techniques and requirements”, could use a 1D detector with MHz-rate capability. Another usage in the experiment area could be the measurement of 1D cuts of power diffraction rings. Details of such experiments have to be defined.

2D detectors

The 2D detectors will be used for a multitude of applications. The requirements can vary widely and need to be detailed for the most prominent types of experiments. The baseline of the HED instrument does not include a 2D detector operating at MHz frame rates, like the Adaptive Gain Integrating Pixel Detector (AGIPD), the Large Pixel Detector (LPD), or the DEPFET Sensor with Signal Compression (DSSC). (See the website of the Detector Development group (WP75) for details.) This seems justified by the large number of experiments requiring solid-sample refreshment that are therefore not able to employ MHz repetition rates. However, the future implementation of single modules of the AGIPD or LPD detectors should not be excluded. For 2D detection, we consider at present CCDs (standard or scientific solutions) or pixel detectors (mostly scientific solutions), which are available from external providers. Large-angle ($2\theta \sim 60^\circ$) scattering experiments will require large-area detector (at least 1 k x 1 k, 15 cm size) very close to the sample (e.g. 5 cm). As part of the technical design, these issues and specifications

for the detectors will be developed in close collaboration with the Detector Development group (WP75) at European XFEL.

7.6 Spectrometers and other ancillary instrumentation

Two major applications for spectrometers are considered. First, the measurement of inelastic X-ray scattering requires detection of a photon energy shift with respect to the incident photon energy. The amount of this shift depends on the exact type of experiment and can be very small (O(meV)) or can reach several 100 eV. Due to kinematic considerations, the shift varies with X-ray scattering angle, and the implementation of spectrometers for this purpose has to consider this requirement. In general, the count rate per X-ray pulse is relatively small. Specific spectrometers will be defined for these cases.

Second, the measurement of self-emission by the excited sample or plasma can vary largely in photon energy and resolution. Emission spectra depend on the element composition of the sample and on the plasma temperature. Plasma emission lines can be extremely narrow, demanding high spectral resolution. Imaging the emitting sample area onto the detector is also important to obtain higher selectivity. Specific spectrometers will be defined for these cases.

8 Experiment hall layout

This chapter describes the layout of the HED instrument inside the experiment hall XHEXP. There are several rooms with different functions. We can distinguish between X-ray rooms having to fulfil radiation safety requirements and infrastructure rooms to install the necessary infrastructure for the HED instrument. In addition, several laser rooms house the OL systems. Figure 8-1 and Figure 8-2 show an overview of the rooms affiliated with the HED instrument. Figure 8-1 shows the location of SASE2 instruments at the south end of the XHEXP hall. The X-ray FEL beam comes from the east (left in the drawing). A particularity of the HED instrument is the laser room (HED-LAS) located on top of the HED-EXP room. Two infrastructure rooms housing electronic racks are located next to HED-LAS on the elevated level too. Table 8-1 provides a brief summary of the HED rooms and lists related interlock and safety requirements.

Table 8-1. Interlock and safety requirements for HED rooms inside XHEXP

Room name	Description	Size W x L x H [m]	Safety precautions	Inter-lock	Search
Transport tube	X-ray beam transport	~ 20 m length	None	No	No
HED-OPT	X-ray optics and OL–X-ray timing tools	1.9 x 9 x 3.5	Radiation safety Laser safety	Yes Yes	Yes
HED-EXP	Experiment hutch	11.5 x 9 x 4 (inner)	Radiation safety Laser safety Electric safety	Yes Yes Yes	Yes Yes
PP-LAS	PP-OL location	4 x ~6	Laser safety	Yes	No
SASE2-LAS	Diagnostics & preparation of PP-OL pulses for HED & MID instruments	13 x ~6	Laser safety	Yes	No
HED-LAS	UHI-OL and HE-OL	12.4 x 11.5 x 3.5	Laser safety	Yes	Yes
HED-RK1	Electronic racks	3.1 x 13 x 2.5	None	No	No
HED-RK2	Electronic racks, capacitor banks for HE-OL	2.5 x 11.5 x 3.5	None	No	No
HED-CTR	HED instrument control	4.6 x 7 x 2.7	None	No	No

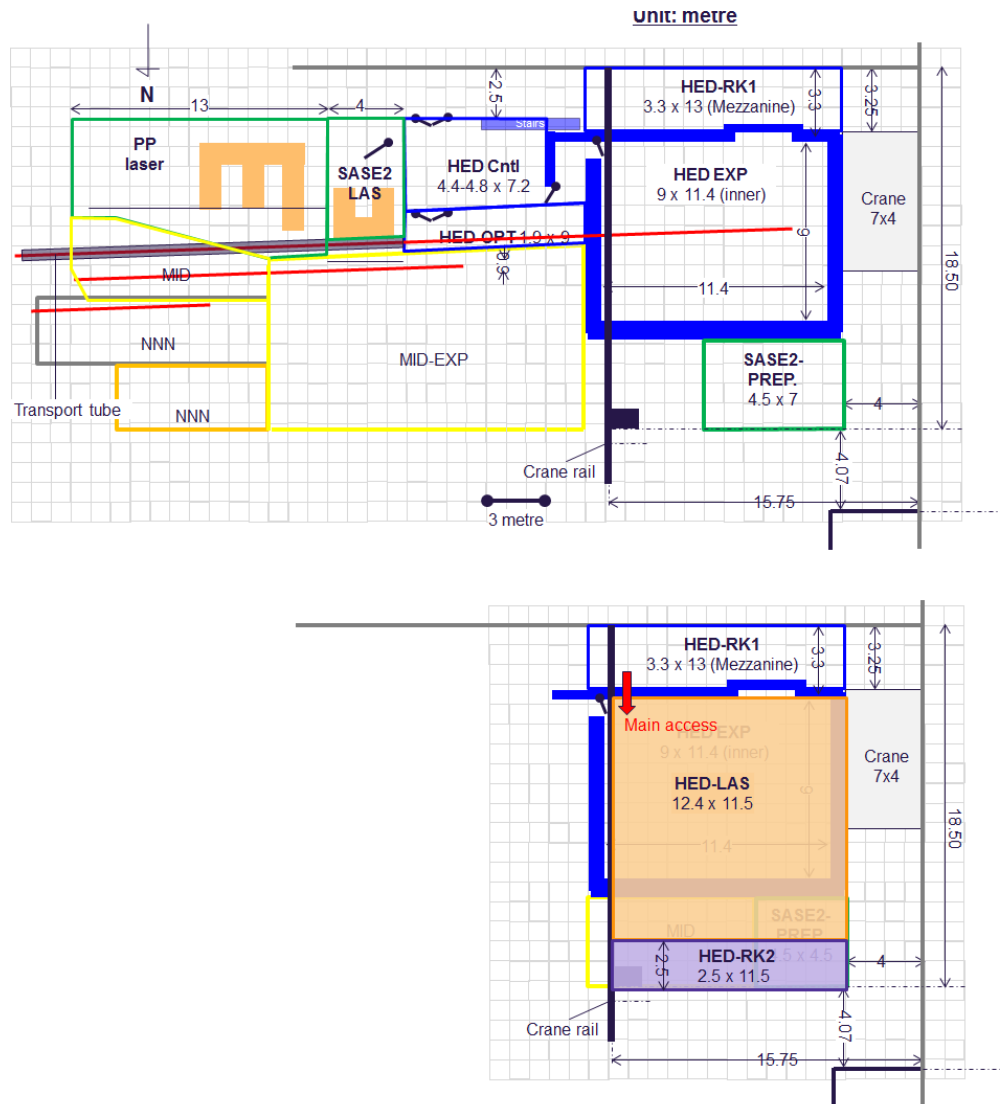


Figure 8-1. Layout of the SASE2 area inside the experiment hall XHEXP. Shown are only the HED-relevant rooms. One square indicates $1 \times 1 \text{ m}^2$. (Top) Experiment floor. HED-RK1 is at the mezzanine level at 3.5 m height. (Bottom) HED-LAS and HED-RK2 at 4.8 m height above the floor.

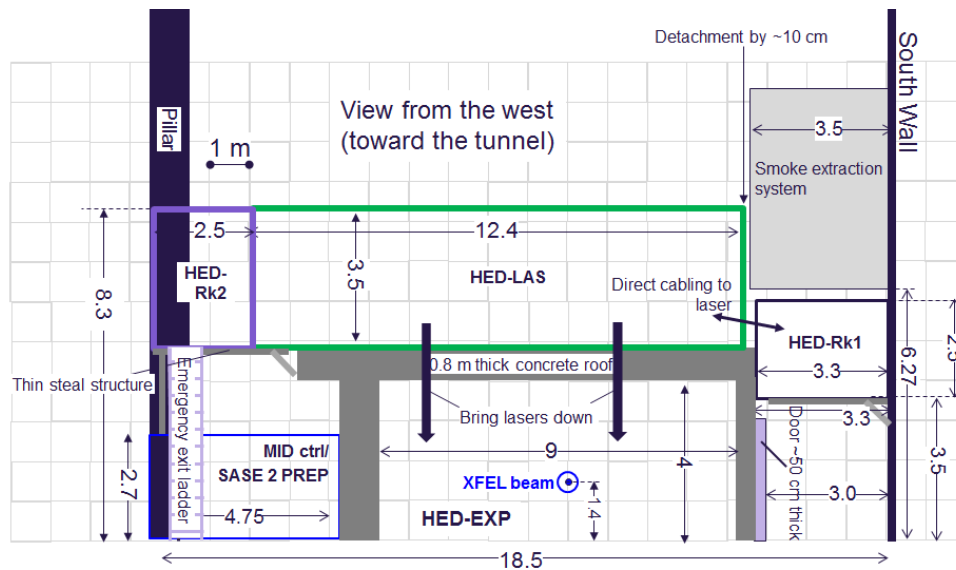


Figure 8-2. Rear view of the HED-EXP area looking from the west wall and indicating the infrastructure room adjacent to the experiment room

8.1 Transport tube

To connect the X-ray beam transport in the tunnel with the HED-OPT hutch, a ~ 20 m long vacuum transport without any optical element will be installed. The transfer tube passes through open space and through the rooms MID-OPT, PP-LAS, and SASE2-LAS. A tube diameter of 100 mm is foreseen. The tube centre will be at a height of 140 cm above the floor, and the supports will be mounted such as to minimally interfere with the main usage of these rooms.

Radiation protection concept

By means of a collimator system inside the preceding beam section (XTD6), the X-ray beam will be collimated such that it cannot hit or interfere with the walls of the transport tube. Furthermore, the status of the vacuum system will be provided to the interlock system in order to ensure that operation is enabled only for a vacuum level better than 10^{-7} mbar. In addition, a radiation monitor inside the SASE2-LAS room, near the end of the transport tube, ensures that no background radiation is generated. An open question is whether backscattering from the receiving aperture or slits inside HED-OPT

could lead to a radiation background and the requirement of shielding. Assuming that backscattering is not an issue and that the conditions above are fulfilled, the transfer tube will remain without lead shielding.

8.2 X-ray optics hutch (HED-OPT)

HED-OPT has a length of 9 m and an inner width of 1.9 m (see Figure 8-3). The height of the lead roof panel should be 3.2–3.5 m. The accessible inner height is 3.0 m. The X-ray beam transport is on the north side, approx. 50 cm from the wall at a height of 1.4 m above the floor. On the south side, a ~ 1 m wide space is reserved for access and transport. A manually operated crane trail with a load of 500 kg will be available. Access to the room is provided by a double door connecting to the HED-CTR room. As to X-ray beam delivery devices, the slits, attenuators, CRL3, backscatter monitor (BSM), and several screen will be located in HED-OPT. These devices are all under UHV conditions and are connected by vacuum tubes inside which the X-ray beam is contained. An X-ray shutter at the end of HED-OPT will enable operation with X-ray beam in HED-OPT without the need to close and interlock the following HED-EXP room. This will facilitate independent operation of the two X-ray areas and allow more efficient use of the instrument.

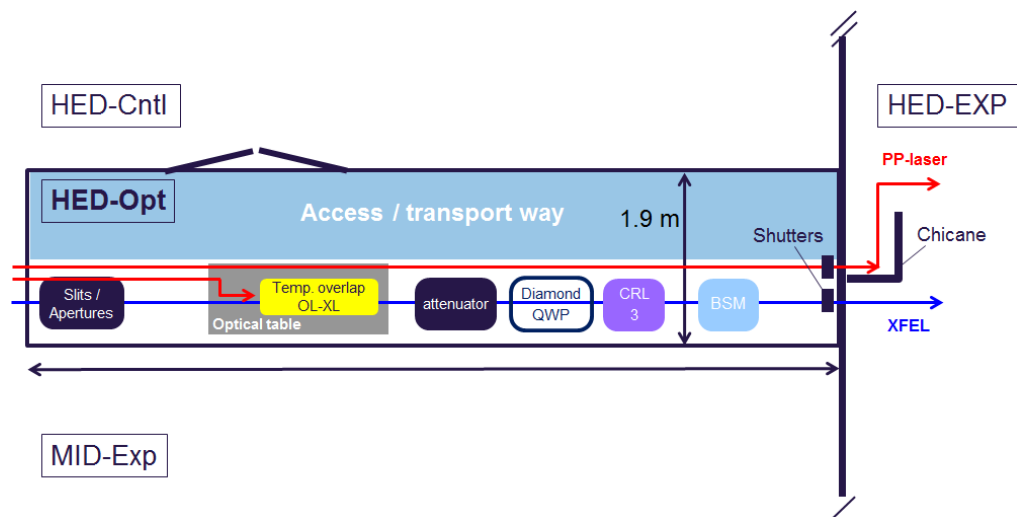


Figure 8-3. Layout of the HED-OPT hutch. Next to the X-ray devices, the PP-OL beam transport is indicated.

An optical bench is included to establish PP-OL–X-ray timing cross-correlation measurements. The PP-OL beam is transported from the SASE2-LAS room in vacuum tubes mounted parallel to the X-ray equipment, at a height of 1.05 m. Two vacuum transport tubes will be used for the two pulses used for cross-correlation measurement inside HED-OPT and for the pump and reference pulses used inside HED-EXP.

HED-OPT needs to have radiation protection and optical laser precautions. Requirements for temperature and humidity stability will not exceed those of the experiment hall and will be established by air exchange between HED-OPT and the experiment hall.

Radiation protection concept

The HED-OPT area will be used with X-ray FEL radiation and therefore requires radiation shielding and a personnel interlock system. Simulations for the radiation shielding of this area have been performed in summer 2012 by Y. Asano at the Super Photon ring-8 GeV (SPring-8) in Hyogo, Japan [56]. Three distances from the X-ray beam to the walls of the HED-OPT hutch have to be considered. Towards MID-EXP (north side), the distance is ~ 50 cm. This is the closest of all the relevant distances. Since the X-ray beam is relatively close to the wall, it needs to be clarified whether the necessary lead thickness will be required for the entire wall or only for a region of ~ 1 m around the beam height. Towards HED-CTR (south side), the distance is 140 cm. The roof panel will be a minimum of 1.8 m above the X-ray beam. Towards HED-EXP, a concrete wall of 80 cm thickness provides sufficient radiation shielding. For the wall at the entrance to HED-OPT (east side), a shielding thickness of 3 mm lead plus 10 mm iron (or equivalent) is considered. Table 8-2 indicates the respective distances from walls to X-ray beam and gives thicknesses for shielding materials, either lead only or lead/iron compounds.

Table 8-2. HED-OPT geometry and shielding requirements for pure lead (assuming 2 mm iron/steel structural support) and lead plus thick iron equivalents

Wall	Distance to X-ray beam [m]	Pb thickness [mm]	Pb+Fe thickness [mm]
South	1.4	4.5	3 + 10
North	0.5	7.5	6 + 10
East	0–9	4.5	3 + 10
Roof	> 1.8	4.5	3 + 10

Laser interlock concept

Inside HED-OPT, the PP-OL will be mostly used to perform timing cross-correlation measurements with the X-ray beam. This semi-permanent setup can be shielded such that the access to HED-OPT will be possible also for people not trained in OL operation. But it should be anticipated that other measurements using the PP-OL might be performed in this room. For this purpose, an OL interlock needs to be available that is independent from the X-ray interlock. Due to the limited space, no anteroom with interlocked double door can be integrated. It rather is planned to provide a laser curtain inside HED-OPT that will prevent stray light from exiting the hutch in case the door is opened. The interlock will act on a laser shutter at the boundary of SASE2-LAS and HED-OPT, disabling the laser beam transport into the room. In case the OL radiation transport to HED-EXP is completely enclosed, it will not be affected by this interlock.

8.3 Experiment enclosure (HED-EXP)

HED-EXP is the main experiment room where users will carry out experiments at the HED instrument. Figure 8-4 shows the conceptual layout of the room. Due to secondary radiation generated by the UHI-OL system, this area has to be enclosed by 50–100 cm thick concrete walls. There are two accesses to HED-EXP: a heavy-load door on the south side (3 m width, 2.5 m height opening) and the chicane entrance in the southeast corner. The big door allows for transport of large components. It has to provide the shielding equivalent of the south wall and will require special movement. It will

therefore be used only for transport and will generally be closed. Personnel access occurs through the chicane entrance.

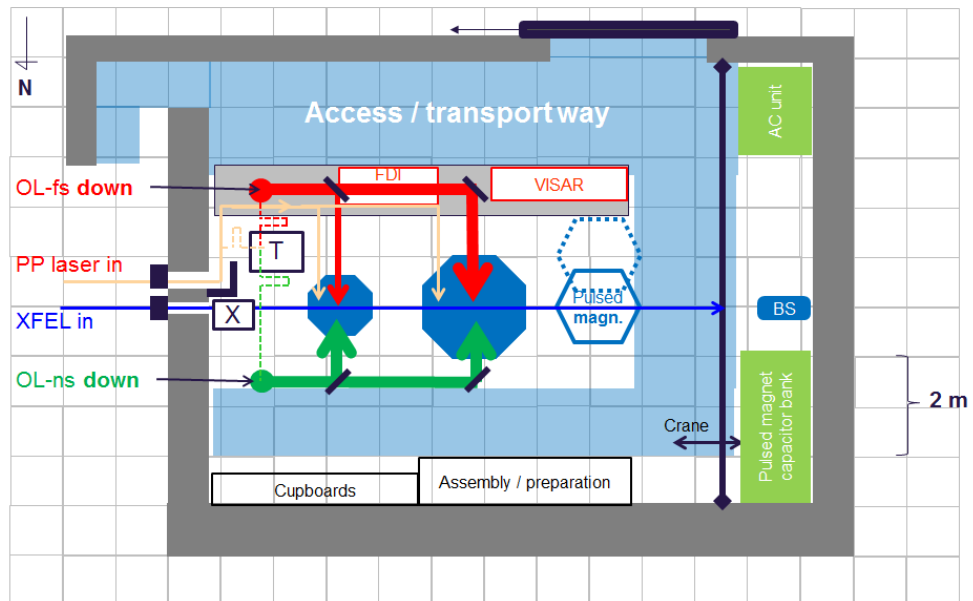


Figure 8-4. Layout of the HED-EXP enclosure. Square “T” is a placeholder for the timing overlap of three optical laser beams. Square “X” is a placeholder for X-ray optics, such as anti-scatter slits, CRLs, or KB mirrors for extreme focusing.

The HED-EXP area is 96 m² with an inner length of 11.5 m and a width of 9 m. A ceiling height of 4 m will allow air distribution and provide space for an overhead crane, while enabling a useable height for the experiments of 3.5 m. The X-ray beam enters HED-EXP on the east side with a beam height of 1.4 m above the floor and is finally stopped at a beam stop device near the west wall. Access to the north area of the hutch has to pass underneath the X-ray beam transport. Tentatively, we foresee three interaction chambers for tight-focus, high-power, and pulsed-magnet experiments, respectively. These are located behind one another on the X-ray beam path.

All OL beams enter the area on its east side. The PP-OL comes through the east wall at a height of 1.05 m, and the UHI-OL and HE-OL come through the ceiling at a distance of roughly 1.0 m from the east wall.

Radiation protection simulation for HED-EXP

HED-EXP will be used with X-ray radiation, produced either by the X-ray FEL or as secondary radiation following the interaction of the UHI-OL with matter. The room therefore requires radiation shielding and a personnel interlock system. It could happen that the radiation levels due to UHI-OL operation are much higher than those generated by the X-ray FEL beam. We therefore developed a corresponding radiation-shielding concept that fulfils the radiation protection requirements for operating the UHI-OL. This solution will at the same time fulfil the needs for the radiation protection of the X-ray FEL beam. The HE-OL will operate at much reduced irradiance and will not have specific radiation protection needs.

Simulation of the radiation levels has been performed by means of an established FLUKA Monte Carlo radiation code [57]. The simulation results have been cross-checked with measurements at the DRACO laser at Helmholtz-Zentrum Dresden-Rossendorf (HZDR), Germany [58]. The simulations have been performed for two sets of laser parameters (see Table 8-3) and for two geometries (see Figure 8-5). The parameters given in the second column of Table 8-3 correspond to the operating conditions of the 100 TW–class laser system to be built by 2016. The radiation shielding will be defined according to the needs of operating this laser at repetition rates of 1–10 Hz. Parameters in the third column of Table 8-3 correspond to the proposed upgrade to a 1 PW–class laser. The higher laser intensity generates higher radiation levels, which have therefore also been analysed. In order not to exceed the radiation levels as defined for operation of the 100 TW laser, the maximum repetition rate of the PW laser will be reduced accordingly.

The two simulated geometries correspond to the operation of the laser beam perpendicular to the incident X-ray beam, and to a collinear geometry. The first case is considered to be the main operating condition, the second is used less frequently. For the perpendicular geometry, the laser beam will always impinge onto the target in the south-to-north direction. Anti-collinear operation may be used in exceptional experiments with special operating conditions. The beam will be focused onto the target, located 3 m from the east and 4 m from the north wall at a height of 1.4 m from the floor, which determines the

3D position of the interaction (IA) point. For the simulations, a 20 μm thick gold foil was used as target.

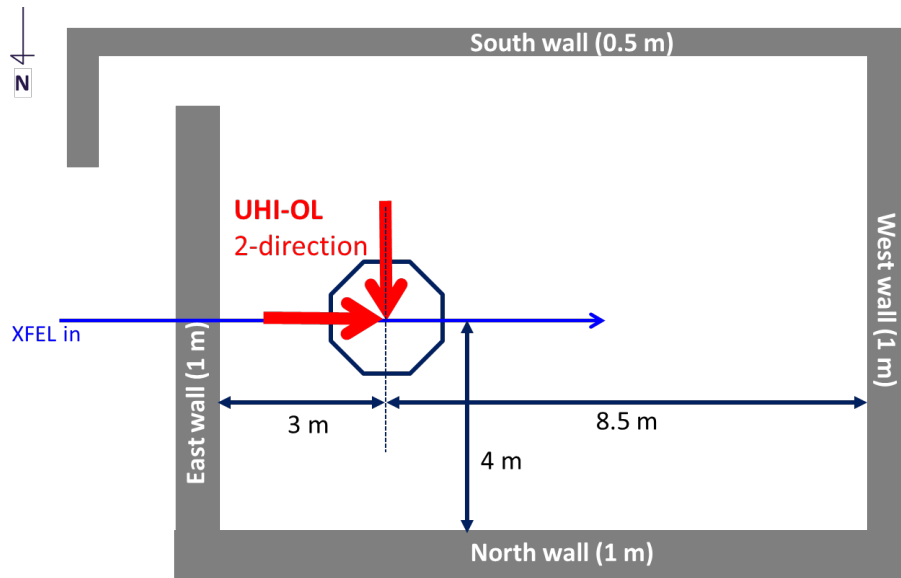


Figure 8-5. Geometry of HED-EXP for the radiation simulations. The two red arrows indicate the two alternative perpendicular and collinear geometries.

Table 8-3. Input parameters of the UHI-OL and the generated electron pulse used in the FLUKA Monte Carlo simulation

	100 TW class	PW class (upgrade)
Laser energy on target	2 J	11 J
Pulse duration	30 fs	30 fs
Spot size (80% pulse energy)	3 μm	3 μm
Peak irradiance	$1.7 \times 10^{20} \text{ W/cm}^2$	$1 \times 10^{21} \text{ W/cm}^2$
Electron temperature	2 MeV	5 MeV
Charge (from 16% coupling)	160 nC	800 nC

This heavy element and the relatively large thickness correspond to a worst-case scenario. Important parameters of the electron pulse for the simulation are its mean kinetic energy and its pulse charge. The mean kinetic energy is determined by the laser irradiance on the target using the theoretical scaling

in Ref. [59]. The charge is estimated by energy conservation with a given conversion efficiency of laser energy into hot electrons. Simulations were compared to measurements using the DRACO laser at HZDR (2 J, 30 fs duration, $30 \mu\text{m}^2$ spot size in $1/e^2$ (3.6 μm FWHM), and 80% of energy in spot, $1.8 \times 10^{20} \text{ W/cm}^2$), which has nearly identical parameters as the planned 100 TW laser. The measurements yielded an electron temperature of $T \sim 2 \text{ MeV}$ [59]. At DRACO, radiation doses were monitored around the 30 mm thick Al interaction vacuum chamber. At 1 m from the chamber wall, a dose of 2–10 $\mu\text{Sv/shot}$ was measured. For an electron half-opening angle of 45° and an electron charge of 160 nC, this dose is consistent with respective FLUKA simulation results. A charge of 160 nC correspond to a conversion efficiency from laser to electrons of 16%. All simulations generated per-shot ambient dose equivalents, $H^*(10)$, to be scaled by the repetition rate of the laser.

Simulation results in Figure 8-6 show the radiation levels inside and outside of the HED-EXP enclosure. For 100 TW parameters and 1 m heavy concrete, an ambient dose outside of the enclosure wall of $10^{-5} \mu\text{Sv}$ per pulse is observed, corresponding to $3.6 \times 10^{-1} \mu\text{Sv/h}$ at 10 Hz operation. For the perpendicular geometry, the radiation level outside of the 0.5 m heavy-concrete south wall is one order of magnitude smaller. The simulations show that this geometry yields the most severe radiation levels compared to those with collinear geometry at the west wall (1 m heavy concrete) and to the roof panel (0.8 m normal concrete). Furthermore, for PW laser parameters, one observes radiation levels approximately two orders of magnitude higher, limiting the repetition rate to 0.1 Hz. The simulations further indicate that the specific type of heavy concrete does not have a significant influence on the attenuation of radiation. Based on existing experience, we therefore suggest the use of iron-containing heavy concrete.

Another issue is the investigation of activation of material surrounding the IA point. This study was only performed for the PW laser parameters, but using extremely long exposures at repetition rates on the order of 1 Hz, which by far exceed the accessible rates $< 0.1 \text{ Hz}$. Even for this unrealistic scenario, the activation of wall concrete and sample chamber components remains below a

level of $1 \mu\text{Sv/h}$ directly after exposure and less than 10 nSv/h after 10 min cooling time.

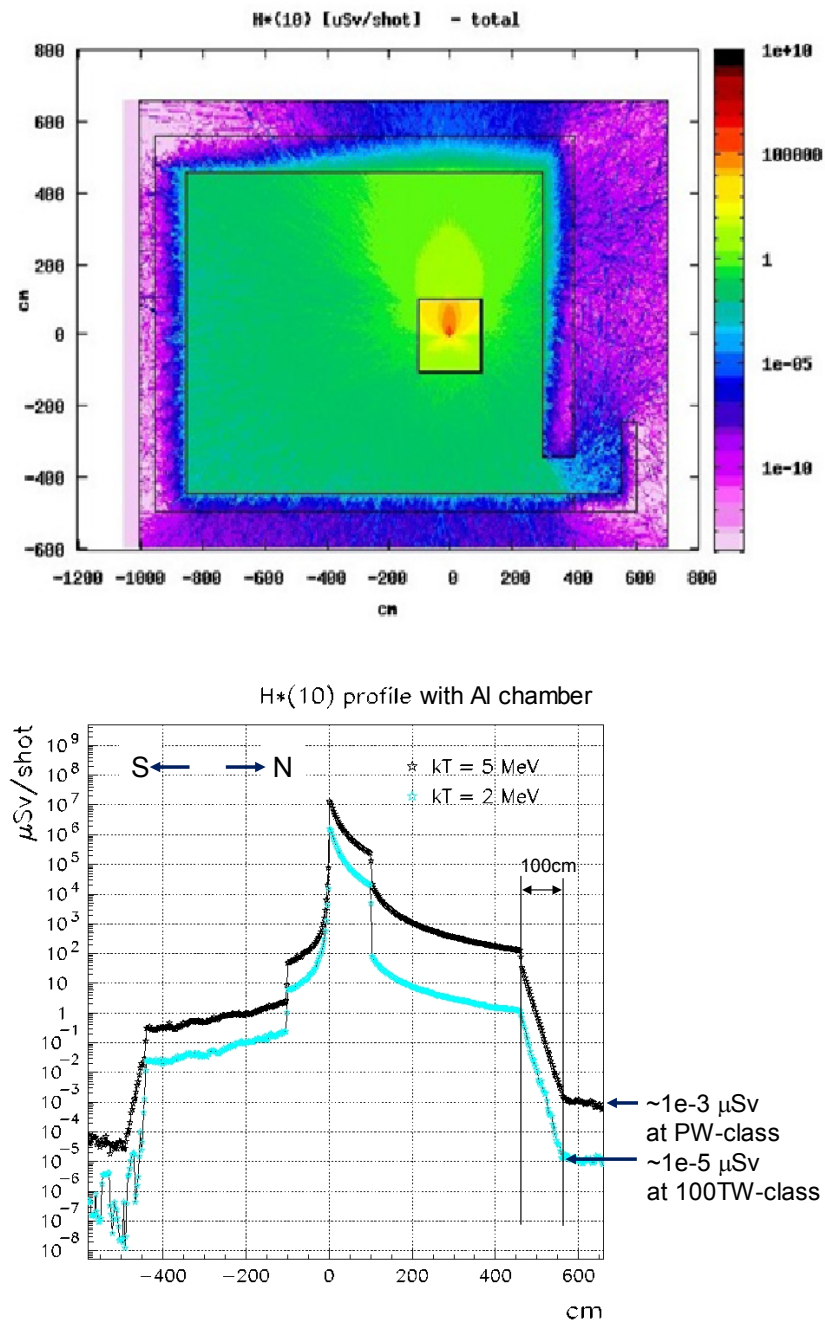


Figure 8-6. (Top) $H^*(10)$ distribution in $\mu\text{Sv/shot}$ in a plane including the IA point. (Bottom) Line-out of the simulated $H^*(10)$ distribution in $\mu\text{Sv/shot}$. Shown is a south-to-north cut including a 30 mm Al vacuum chamber at 1 m from the IA point. The light-blue line corresponds to 100 TW, and the black line to 1 PW laser parameters.

Based on the results of simulations and experiments, we conclude that the HED-EXP room has significant shielding requirements. The shielding equivalents shown in Table 8-4 have to be reached for the side walls and the roof of HED-EXP.

Table 8-4. Shielding equivalent of HED-EXP walls

Wall	Description	Wall thickness
East	Entrance for X-ray FEL; entrance for PP-OL beams	0.8 m, heavy iron-based concrete
North	Principle laser pointing direction; distance to IA point ~ 4 m	1 m, heavy iron-based concrete
West	Secondary principle laser pointing direction; distance to IA point ~ 6–8 m	1.0 m, heavy iron-based concrete
South	Opposite to principal laser pointing direction; access door	0.5 m, heavy iron-based concrete
Roof	Access door; entrance for UHI-OL and HE-OL beams; height 2.6 m above IA point	0.8 m, normal concrete

Any opening in these walls needs to achieve the corresponding shielding equivalent. In addition, the ambient dose level outside of HED-EXP will be monitored. In case an integrated dose of 2 μ Sv is exceeded in a time period of 4 h, laser operation will be blocked for the remainder of the 4 h period. Activation of material inside HED-EXP is not considered to be an issue and does not require specific radiation protection measures.

Laser interlock concept

Inside HED-EXP, several OL configurations can occur. In general, the room must be secured by a laser interlock system ensuring that only qualified laser operators can enter the room during laser operation. This applies to all lasers in HED-EXP: PP-OL, UHI-OL, HE-OL, and other Class 4 systems, such as a Q-switch laser for the VISAR diagnostic. This system is independent of the X-ray interlock. The interlock will act on a shutter disabling the laser beam transport into HED-EXP.

Since the UHI-OL operation can generate ionizing radiation independent of the X-ray FEL beam, it must have two operating modes, called *alignment* and

experiment modes. In the *alignment* mode, qualified laser operators have access to the HED-EXP area. In the *experiment* mode, no one will be allowed to enter, and HED-EXP must be searched and radiation-interlocked. The radiation interlock system installed for accelerator and FEL operation will provide a signal to the laser control system stating these conditions. Only if this signal is available will it be possible to operate the UHI-OL beam in HED-EXP in the *experiment* mode. The HE-OL will also have *alignment* and *experiment* operation modes, with similar boundary conditions for the operation and laser control system.

8.4 Control room (HED-CTR)

HED-CTR provides the workspace for the experimenters. At least three different activities can be distinguished: instrument control, data analysing, and miscellaneous activities. A sketch of HED-CTR is shown in Figure 8-7. This room is laid out such as to give experimenters access to HED-OPT and HED-EXP. In addition, transport of components into HED-OPT will be done through HED-CTR. The size of the room is approximately 4.6 x 7 m² with an inner height of 2.7 m. The access to HED-EXP is designed as a chicane to avoid radiation leakage from HED-EXP. The chicane will also serve for laser interlock and clothes changing for clean working conditions inside HED-EXP. Interlock panels for access to HED-OPT and HED-EXP will be installed next to the access doors inside HED-CTR. Stairs outside HED-CTR that partially cover the south façade provide access to the HED-RK1 and HED-LAS rooms on the elevated floor level.

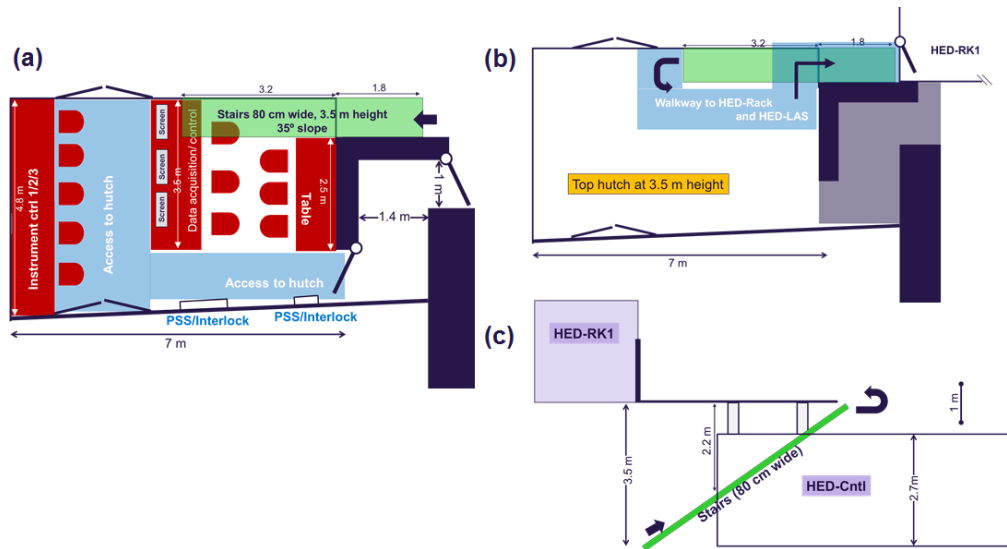


Figure 8-7. Layout of the HED-CTR room: (a) Top view. (b) Top view of the ceiling level of HED-CTR, which will be used as a footpath to access the HED rack rooms and HED-LAS in the top hatch. (c) Side view showing how the stairs will be arranged.

8.5 SASE2 laser laboratory (SASE2-LAS)

The SASE2 laser laboratory will be situated next to the PP-LAS room. In this room, qualified laser operators can tune the PP-OL to fulfil specific requirements for OL beam delivery. This room is shared with the MID instrument, and only a part of its interior is relevant to HED. Laser components for the different instrument delivery systems are located on separate tables.

Laser interlock concept

SASE2-LAS houses several laser tables with complex instrumentation. Access to this room during operation of the laser is allowed only to experienced and trained personnel. An interlock ensures that no untrained personnel can enter the room during laser operation. An anteroom with interlocked double door is foreseen, and the interlock will act on a laser shutter at the boundary between PP-LAS and SASE2-LAS.

8.6 HED laser room (HED-LAS)

The HED laser room will be situated on top of the experiment hutch at a height of 4.8 m from the experiment floor. As shown in Figure 8-8, the room size is around 140 m² (12.4 x 11.5 m²) with an inner height of the room of 3.5 m. The 80 cm thick floor should allow nearly vibration-free conditions, which will be tested using a vibration simulation. The room will house the two HED laser systems, UHI-OL and HE-OL. Details of these lasers are provided in Chapter 6, “Optical laser installations”. The front end, amplifiers, and compressor gratings for the two lasers will all be installed in this room. Access to the room will be through a door on the south side. Another door on the north side connects HED-LAS to the HED-RK2 room. Instrumentation will be transported into the room through a large opening or door on the west side of the room. The exact concept of this transport still needs to be defined, as the door is 4.8 m above the floor.

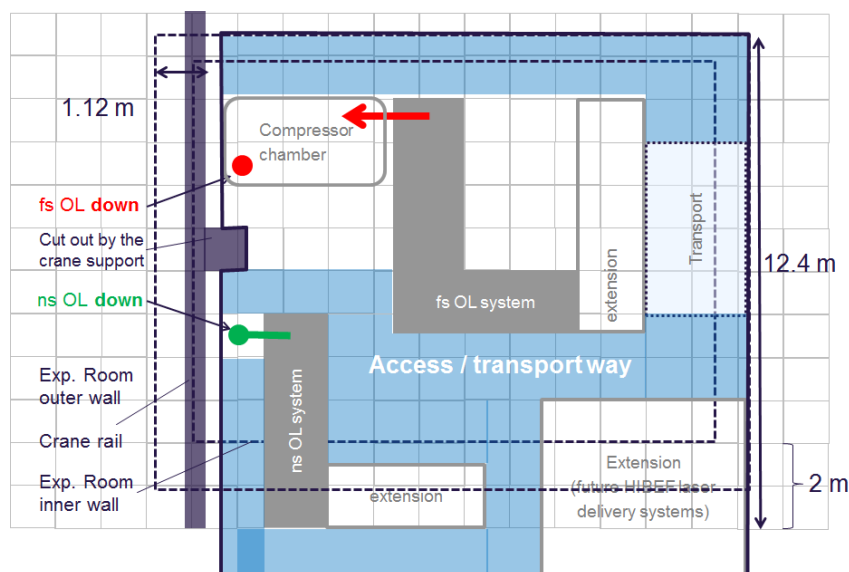


Figure 8-8. Layout of HED-LAS room at 4.8 m height

There will be two holes in the floor with a diameter of 20–25 cm. These holes will be used to transport the UHI-OL and HE-OL beams to the HED-EXP room. The exact position of these holes still requires definition. They are currently placed close to the east wall in order to minimize interference with the overhead crane inside HED-EXP. The area on the west–north side (lower

right in Figure 8-8) is a placeholder for the space required to receive the future HIBEF laser beams (500–1000 TW short-pulse laser and kJ long-pulse laser), which will be delivered through transport tubes from a future external laser building.

In order to assure a stable and reliable OL delivery, HED-LAS has to fulfil the following strict conditions with respect to cleanliness, temperature, and humidity stability:

- Temperature stability of $21 \pm 0.1^\circ$ is required.
- Humidity control of $45 \pm 2.5\%$ is required.
- Clean room Class 100 will be provided.
- Mechanical vibrations have to be evaluated and minimized to prevent pointing fluctuations.

Laser interlock concept

HED-LAS houses several high-energy laser systems. Access to this room during operation of the laser is allowed only to experienced and trained personnel. In addition, during full-energy operation of the OL systems, no personnel access is possible. An interlock ensures that no untrained personnel can enter the room during operation and that no person is in the room during high-energy operation. An anteroom with interlocked double door is foreseen. It has to be defined in detail on which components the interlock acts.

8.7 Infrastructure rooms (HED-RK1 and HED-RK2)

For installation of electronic racks, two infrastructure rooms will be needed. The first, HED-RK1, will be situated at a mezzanine level at 3.5 m height from the experiment floor, on the south side of the HED-LAS room. The room size is $3.1 \times 13 \text{ m}^2$ with 2.5 m inner height. This room should be used for electronic racks to accommodate controllers and power supplies for the X-ray beam delivery devices, the vacuum systems, all laser DAQ and control devices, all

diagnostics, and the UHI-OL power supplies. The access door to this room from the experiment floor will be situated at the east side (left side of Figure 8-8). Part of this room will be used as an anteroom for entrance to HED-LAS, which is a clean room requiring clothes changing and interlock.

The second infrastructure room, HED-RK2, will be located on the north side of the HED-LAS room on the same level of 4.8 m above the experiment floor. The electronic racks in this room will accommodate the capacitor bank and power supplies for the HE-OL system, which require at least five standard 19-inch racks. This room has a size of 2.5 x 11.5 m² and an inner height of 2.5 m. Figure 8-9 shows the two infrastructure rooms.

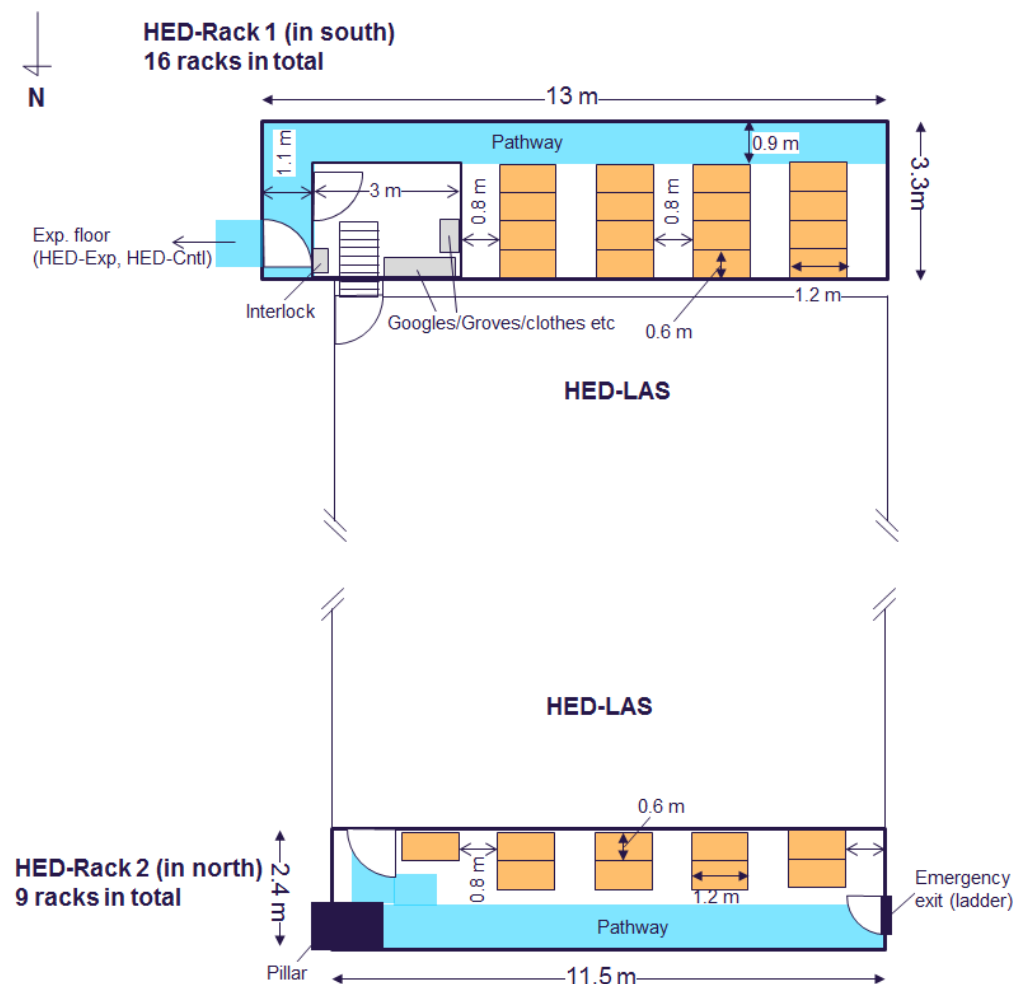


Figure 8-9. Layout of the infrastructure room HED-RK1 (top) and HED-RK2 (bottom)

9 Project issues

This chapter includes an outline of interfaces to other work packages and the HIBEF user consortium, a breakdown of WP82 tasks in terms of the various devices that are part of the HED instrument, and an outline of the schedule to construct and commission the HED instrument.

9.1 Interfaces to other work packages

The HED instrument work package (WP82) has several interfaces with other work packages of the European XFEL project. Some aspects of these interfaces are described below for each of the other work packages. Beyond the scope of this CDR, the interfaces to at least those work packages with several critical items will be discussed in detail with the involved groups and will be described in corresponding documents.

X-Ray Optics and Beam Transport (WP73)

With WP73, several interfaces exist due to the fact that the HED instrument depends on the beam delivery enabled by WP73. In addition, some of the HED optics components are located inside the XTD tunnels and integrated into the standard beam delivery system under WP73 responsibility. Close contact between the work packages and regular meetings will be used to follow progress and identify issues in a timely fashion.

In preparation of this CDR, the following interface items were identified and discussed.

Beam delivery mirrors (two offset and one distribution mirror)

- HED aims at 25 keV radiation.
- WP73 will investigate use of second stripe (Pt) or bare substrate to raise high-energy cut-off.

- The second offset mirror can be tuned such that it generates a high-energy cut-off above 9 keV, therefore making an additional harmonic-suppression mirror inside the HED instrument unnecessary.
- All mirrors will have adaptive bending. When using the CRLs for focusing, this system can be used to make the mirrors flat.
- WP73 will investigate possibilities to select single trains (at 10 Hz rate) for reflection to HED. This may be done either by using special electron beam techniques or by moving the mirror into the central beam.
- WP73 defines, integrates, funds, procures, coordinates, and installs.

Collimation and focusing scheme

- The HED CDR foresees to use CRL focusing using three devices.
- CRL1 is defined jointly with WP83 (MID instrument) to collimate the X-ray beam.
- CRL2 will provide intermediate focusing at HED and is located ~ 100 m in front of the experiment hall.
- CRL3 will provide tight focusing (few micrometres).
- WP82 aims to have unified CRL devices at HED and other instruments.
- WP73 integrates, procures, coordinates, installs, and may provide some funding for mechanical support and/or vacuum components for CRL1 and CRL2.
- WP82 takes the lead on CRL3 inside HED-OPT.
- WP82 defines and funds.

Beam sizes and damage

- WP82 provides lists of estimated beam sizes at location of beam transport devices to enable WP73 to check for damage and heating issues.
- First implementation of SDU and pulse picker devices is probably only good enough for 10 Hz single-pulse operation.
- Heating will reduce number of useable pulses at monochromator. Details are found in [43].

Split and delay unit (SDU)

- An agreement will be concluded with U Münster about the deliverables, time schedule, and responsibilities. U Münster currently applies for additional funds for SDU diagnostics. Once the outcome is known, the agreement could be drafted.
- WP73 has some resources foreseen for integration and installation.
- WP73 integrates, coordinates internally, and assists in installation.
- WP82 defines and coordinates with U Münster.

Monochromator

- WP73 is responsible for building a standard monochromator.
- Second monochromator is responsibility of WP82.
- WP82 analyses beam offset issue in detail. A four-bounce monochromator will ease this constraint.
- WP82 further has a request for a high-resolution monochromator.
- Requirement to resolution is still to be determined. Si(511) provides roughly 100 meV at 8–10 keV, uses artificial channel-cut geometry, and can be tuned from 8 to 24 keV. Higher resolution requires use of back reflection channel cut. HED is involved in an experiment at LCLS to solve open issues on this matter.
- WP82 proposes to investigate the possibility of a combination of four-bounce and high-resolution monochromator in one device.

Gas monitor detector (GMD)

- HED requests to have some online monitor towards the end of the beam transport. This was implemented in spring 2013.
- WP73 integrates, coordinates, and partly installs (joint activity with WP74).

Pulse picker

- WP73 proposes to investigate existing design suitable for 10 Hz operation.
- WP73 integrates and assists in installation.
- WP82 defines, procures, funds, and coordinates.

Beam shutter

- Beam shutter includes 30/32 mm B₄C/W aperture limiting the maximum beam size at this location.
- WP73 defines, integrates, funds, procures, coordinates, and installs.
- A second shutter should be installed at the end of HED-OPT. WP82 is responsible for this device.

Vacuum interface to HED instrument inside XHEXP

- HED will have ~ 20 m vacuum tube (DN100), which ideally should not require lead shielding. This requires interlocking the vacuum and collimating the X-ray beam so it cannot hit the tube wall.
- Collimation can be achieved by means of the beam shutter collimator plus one additional collimator of identical or smaller size located at least 20 m before the shutter. This corresponds to the position of the GMD.
- Vacuum interface with metal-tightened valve plus ion getter pump on the instrument side of the valve to measure pressure. This is a WP73 task.
- Due to the high pressures inside the HED interaction chambers (10^{-6} – 10^{-4} mbar) and the ablation processes, apertures will be placed in the beam transport between HED-OPT and HED-EXP. A vacuum sensor, and possibly a particle sensor, should be placed inside HED-OPT to provide a vacuum signal to the vacuum interface.
- WP82 will seek advice and approval from WP73 for the design and integration of the instrument vacuum system.

X-Ray Photon Diagnostics (WP74)

Diagnostics are an important area and WP74 offered to support WP82 in addressing related issues. A close contact between the work packages was agreed. If joint projects are defined, regular meetings will be used to follow progress and identify issues timely. In preparation of this CDR, the following points were discussed concerning different classes of diagnostics.

Gas-based diagnostics as part of X-ray beam transport

- WP74 is responsible for constructing and commissioning these devices. In the HED beam transport, two XGMD/XBPMs and one PES system are integrated. WP74 coordinates these activities with WP73.
- After commissioning of these devices, WP74 will transfer its know-how required for operation to WP82.
- WP74 builds a PES detector using Kr and Xe gas for the SASE2 beamline. This device will measure photon energy and (possibly) bandwidth. It is not clear at present if these observables are necessary for HED operation.

Other X-ray diagnostics

- WP74 offers to support WP82 in the selection and design of these devices. Technical design and implementation should be the role of the European XFEL Central Instrumentation Engineering (CIE) team working for the scientific instruments. Ideally, common solutions should be found and implemented.
- WP74 has an ongoing programme for diamond-based transmission intensity and beam position monitors. Currently, there are providers of 100 μm thick diamond but not of the more suitable 50 μm material. These detectors will be tested by WP74 in 2013 with X-ray FEL beam. After these tests, WP74 will be able to provide full assessment.
- For backscatter monitors, WP74 has already evaluated the options and can assist in design and implementation.

- WP74 has developed two screen designs and will provide support in defining requirements and selecting an optimized design for the HED beam transport.
- WP74 is working on a proposal to integrate a spectrum measurement using bend crystals into the SASE beam transport.
- One scientist position in WP74 will be dedicated to timing diagnostics. Starting in April 2013, this person should provide expertise and help to define the HED device.

Detector Development (WP75)

The definition of detectors for the HED instrument is at present at an early stage. It seems relatively clear that 0D, 1D, and 2D detectors will be employed at the HED instrument, but the details of the experiments and the detector requirements are unknown at present. Experiments at the HED instrument will use sub-Hz, Hz, 10 Hz, but also MHz repetition rates. For experiments utilizing repetition rates of 10 Hz or less, the frame rate requirements for 2D detectors are more relaxed. Some detectors could operate under ambient conditions, others need to be located in vacuum. Vacuum means typically 10^{-6} mbar inside the IA chambers and 10^{-8} mbar in the beam transport section. Electromagnetic pulse (EMP) issues related to the high-power laser must be analysed. A close contact between the work packages and the timely (before summer 2013) definition of detector requirements was agreed. Once projects are defined, regular meetings will be used to follow progress and identify issues in a timely fashion. In preparation of this CDR, the following points were discussed concerning different classes of detectors.

0D fast detectors

- Point detectors will be used for the I_0 backscatter intensity monitor (BSM) measuring the incident photon flux with high precision.
- This detector should be suitable for 4.5 MHz repetition rate operation, meaning that the signal should be provided in less than 200 ns.
- In addition, a high dynamic range is required. Ideally, operating over more than eight orders of magnitude should be possible.

- This can only be achieved by using more than one detector and by optimizing the electronic and mechanic realization.
- WP75 is tasked with veto signal generation and will support WP82 in building such a detector.

1D fast detectors

- 1D detectors will be used for FEL spectrum measurements and for spectroscopy measurements (emission, inelastic scattering).
- Due to the operation mode of the HED instrument, 10 Hz operation will be sufficient for a large class of experiments.
- 25 μm pixel size will be extremely helpful for spectroscopy, but detailed design will have to be established.
- Simplified FXE setup for spectrum measurement [44] may be applied.
- Plan 2 Gotthard-type detectors are foreseen for HED.

2D fast detectors

- These will be needed for certain types of experiments, but details need to be determined. Conventional CCD detectors operating at 1–10 Hz have been considered.
- Applications are imaging and SAXS. No requirements have yet been detailed.
- It needs to be analysed if the Fast-CCD detector developed by LBNL will be a useful option for HED. Its small dynamic range must be considered. For SAXS, the detectors should have a central hole or at least a slot. The mixed-mode pixel array detector (MMPAD) maybe an alternative option (pixel size 150 μm) that can in principle provide a dynamic range of 10^8 .

DAQ and Control Systems (WP76)

(to be completed until fall 2013)

Devices to be controlled.

Rack requirements and definitions.

Vacuum control system.

Instrument control, data collection and visualization.

Data retrieval and scientific computing.

Optical Lasers (WP78)

The interfaces with WP78 concern the definition, design, construction, and installation as well as the operation of the various OL systems used at the HED instrument. WP78 possesses laser expertise that should flow into the design of all laser systems at the HED instrument. WP78 will build up the PP-OL system and will provide laser beam to the SASE2-LAS room. WP82 will be responsible for the installations in the SASE2-LAS room related to the HED instrument, and for installations in the other HED rooms. WP78 and WP82 will collaborate on all issues related to provision and usage of the PP-OL system. WP78 has assigned one person (G. Palmer) to establish the interface to the scientific instruments; on the HED instrument side, M. Nakatsutsumi will be the contact person. In addition, WP78 will assign one person (G. Priebe) to provide support with the integration of the large laser systems to be provided through the HIBEF UC. A close contact between the work packages and regular meetings of the contact persons will be used to follow progress and identify issues in a timely fashion. In preparation of this CDR, the following interface items were identified and discussed.

Requirements to and implementation of PP-OL

- PP-OL will be used for sample excitation in pump–probe experiments, for sample diagnostics (e.g. FDI or time-resolved microscopy), for OL–X-ray cross-correlation measurements to determine the X-ray arrival, and for OL–OL cross-correlation to determine the jitter of the high-energy laser pulse delivery.
- WP78 and WP82 will collaborate closely to develop methods to achieve targeted pulse duration, pointing stability, switching between various operation modes such as changes in pulse energy, frequency conversion, and temporal chirping. It is relatively clear that the highest attainable pulse energies will be relevant for WP82. PP-OL will be used to cover the range of 0.2–4.5 MHz for experiments enabling high repetition rate.

- Both the $\lambda = 800$ nm and the $\lambda = 1030$ nm pulse will be provided to the HED instrument. In a first phase, only frequency doubling and tripling will be foreseen, no continuous wavelength coverage.

Involvement of WP78 staff in HED laser system integration

- WP78 will support WP82 in its tasks to design and build up the various laser systems at the HED instrument. The responsibility will be with WP82.
- WP78 will participate in the commissioning of the PP-OL at the HED instrument for the applications outlined above.

Interface to laser control

- WP78 and WP82 will jointly define the laser parameters to be monitored and stored in the experiment metadata by users (or staff) during the operation of the HED instrument. The visualization of these parameters has to be part of the HED control system.
- WP78 and WP82 will jointly define the laser parameters to be changed and adjusted by users (or staff) for the operation of the HED instrument. Access to selected parameters has to be enabled in the HED control system.

Sample Environment (WP79)

(to be completed until fall 2013)

Fast sample mover

Sample delivery to chamber

Sample fabrication

Scientific Instrument MID (WP83)

CRL1 device

- WP83 and WP82 will jointly define the requirements to this device and share related funding.

Floor space allocation and joint areas

- WP82 and WP83 developed and agreed on the layout, which now forms the basis for the SASE2 instruments.
- WP83 and WP82 define, use, and are jointly responsible for the SASE2-LAS room with the optics to set the PP-OL parameters for use in the instruments.
- WP83 and WP82 define, use, and are jointly responsible for the SASE2 preparation room.

Use of central beam for HED

- The use of the central X-ray FEL beam for HED is a long-term development project. WP82 and WP83 agree on its potential and will investigate possible implementations.

Radiation Safety (WP35 and European XFEL)

(to be completed until fall 2013)

Approval of beam transport scheme

Approval of hutches and experiment area

Personnel Interlocks (WP38)

In a meeting with WP38, the ideas for the interlock of the HED instrument were discussed. No major problems were identified. However, deviating from a first proposal, the concept for the HED instrument interlock was somewhat modified.

Interlock for HED-OPT and HED-EXP incl. laser-generated X-rays

- A particularity of the HED instrument is the generation of X-rays by high-energy lasers in HED-EXP. While the laser operating system and the related laser interlock system are separate, the interlock system provided by WP38 will provide the functionality to interlock HED-EXP to enable operation of the high-energy lasers.

- The HED instrument will feature three modes of operation:
 - Open access
 - X-ray FEL delivery enabled (applies to HED-OPT and HED-EXP, which form two independent interlock areas with a safety shutter in between)
 - OL and X-ray FEL delivery enabled (applies to HED-EXP). HED-EXP is searched and interlocked. To avoid radiation leaking towards HED-OPT, the existing shutter between HED-EXP and HED-OPT must be closed.

Layout of the interlock system

- HED-OPT will have only one entrance with a double door.
- HED-EXP has two entrances: a large door for transport and a small door at the chicane for personnel access during operation. Both doors need to be interlocked. The system is similar to experiment hutches at PETRA III at DESY.
- The interlock system has a mounting depth of 20 cm from the wall.

Electromagnetic Compatibility (EMC) (WP39)

(to be completed until fall 2013)

Technical services

(to be completed until fall 2013)

Requirements for XHEXP infrastructure

Infrastructure implementation

Hutch and concrete components definition

Hutch and concrete implementation

PBS coordination

(to be completed until fall 2013)

Time and installation planning

Transport issues

9.2 Work breakdown structure

The work breakdown of the HED instrument at present is very rough. This will improve as soon as more details are established. Table 9-1 shows the breakdown including one level of subcategory. The completeness still has to be verified.

Table 9-1. Work breakdown list of major components of the HED instrument including allocation of coordination responsibility and funding source. This breakdown includes CRL1 and devices beyond the distribution mirror, which defines the HED-specific beam transport. (Key: HS = Harald Sinn (WP73), KA = Karen Appel (WP82), MN = Motoaki Nakatsutsumi (WP82), TC = Technical Coordination group, TBD = to be determined.)

Component	Subcomponent	Coordination	Funding
CRL	CRL1	WP73/CIE	WP73/82/83
	CRL2	WP73/CIE	WP82
	CRL3	KA/CIE	WP82
Distribution mirror	—	HS	WP73
SDU	—	KAWP73	U Münster
Monochromator	Standard	WP73	WP73
	HR mono	KA	WP82
	QWP	TBD	UC
Diagnostics	XBPMs	WP73/WP74	WP74
	Time diagnostics	MN	WP82
	Spectrum	KA	WP82
	Screens	KA	WP82
	I_0	KA	WP82
Beam transport & vacuum	Collimator	HS	WP82
	Transport tube	KA/CIE	WP82
	Pulse picker	HS/CIE	WP82
	Slits	KA/CIE	WP82

Component	Subcomponent	Coordination	Funding
	Attenuator	KA/CIE	WP82
	Beam stop	CIE/HS	WP82
	Vacuum comp.	CIE	WP82
IA chambers	IA1	KA	WP82
	IA2	TBD	UC
	IA3	TBD	UC
Sample holder/movement	—	MN	WP82
Rooms/hutches	HED-OPT	MN	WP82
	HED-EXP	MN	WP82/UC
	HED-LAS	MN	WP82
	SASE2-LAS	MN	WP82/83
	HED-CTR	MN	WP82
	HED-RK1	MN	TC/WP82
	HED-RK2	MN	TC/WP82/UC
Detectors	0D (diodes)	TBD	WP82
	1D (Gotthard)	TBD	WP82
	2D (CCDs)	TBD	WP82/UC
	2D (large-area)	TBD	WP82/UC
Laser	FS-OL	MN	UC
	NS-OL	MN	UC
	PP-OL	MN/WP78	WP82/WP78
	X-ray beam alignment	MN	WP82
	OL-OL cross-correlation setup	MN	WP82
	OL transport	MN	WP82
	FDI instrument	MN	WP82
	VISAR	MN	tbd
Electronics and cables	—	TBD	TC/TBD

A Acknowledgements

This conceptual design report was written by the HED group members Motoaki Nakatsutsumi and Thomas Tschentscher, with contributions from Karen Appel (HED group), Tom Cowan (HZDR), Anna Ferrari (HZDR), Hans-Peter Schlenvoigt (HZDR), Jörg Stempffer (DESY), and Martin von Zimmermann (DESY).

First of all, we thank the HED advisory review team—Richard W. Lee (chair), Patrick Audebert (LULI), Andrew Higginbotham (U Oxford), Hae-Ja Lee (SLAC), Hanns-Peter Liermann (DESY), David Neely (STFC), Paul Neumayer (GSI), Klaus Sokolowski-Tinten (U Duisburg), and Sven Toleikis (DESY)—for their thorough review of the present CDR.

We are very grateful to Harald Sinn of the X-Ray Optics and Beam Transport group for substantial input to our X-ray beam transport concept.

We thank Max Lederer of the Optical Lasers group for extensive advice on the optical laser concept. Guido Palmer markedly contributed to the PP-OL beam transport design. We are grateful for his support.

We thank Jan Grünert of the X-Ray Photon Diagnostics group for giving us substantial advice on XGMD/XBPMs, monitors, spectrometers, and timing tools.

Tobias Haas and Niko Saaristo of the Technical Coordination group provided useful comments on our room designs and integrated our conceptual layout into CAD drawings. We acknowledge their support.

We thank Anders Madsen, Gabriele Ansaldi, Jörg Hallmann, and Thomas Roth of the MID instrument group for many contributions on our shared issues: CRL concept, experiment hutch layout, and many others.

Sebastian Roling and Helmut Zacharias (Westfälische Wilhelms-Universität Münster) significantly contributed to the split and delay unit design and development. We thank them very much for their activity and support.

We are grateful for useful discussions with JJ X-Ray, particularly Christian Mammen, and for allowing us to use its X-ray optics design in this report.

We thank Sigrid Kozielski of the Safety and Radiation Protection group and Albrecht Leuschner (DESY) for their careful advice on our radiation shielding concept.

In addition, we acknowledge helpful discussions with and suggestions from Erik Brambrink (LULI), Ryan Coffee (SLAC), Jerome Hastings (SLAC), Aymeric Robert (SLAC), and Christian Schroer (TU Dresden).

We would like to thank our other colleagues at European XFEL for fruitful discussions and for contributing ideas: Andrew Aquila, Lewis Batchelor, Christian Bressler, Nicola Coppola, Martin Dommach, Andreas Galler, Wojciech Gawelda, Klaus Giewekemeyer, Antonios-Vassilios Lalechos, Adrian Mancuso, Tommaso Mazza, Michael Meyer, Cigdem Ozkan, Nadja Reimers, Osama Ahmed Salem, Andreas Schertz, Joachim Schulz, Wolfgang Tscheu, Gerd Wellenreuther, and Christopher Youngman.

We thank Kurt Ament and Ilka Flegel for assistance in formatting and proofreading this report.

B Report on the HED-ART meeting

The HED-ART Committee met on March 11, 2013 to discuss the progress being made on the plans for the HED instrument at the European XFEL. The attendees are listed in an appendix. The primary responsibility was to review the CDR that had been provided to the committee members about 10 days prior to the meeting.

The meeting consisted of seven presentations with a free exchange of ideas occurring during the presentations. Lest anyone gets the idea that this document indicates only those things that were questioned and this is representative of the meeting – that is far from the case. The CDR was responsive to the need and the very few things we discuss below are intended as assistance to the HED team.

Presentation I: Introduction. (Presenter – T. Tschentscher)

The charge to the committee was provided with a brief but general recapitulation of the history of the effort. The two basic desired results from the meeting were:

- 1 Determine where any problems with the CDR may occur and then to fill in any missing pieces.
- 2 Generally comment on the CDR

Presentation II: Overview of the HED instrument (Presenter – T. Tschentscher)

The plan for hiring was discussed and it was indicated that there are to be two hires to deal with the work on the HED instrument. These are one scientist and one engineer.

It was discussed that, although the burst mode for maximizing the data rate is of importance to European XFEL, it is somewhat difficult to implement for a large subset of experiments to be developed at the HED instrument. The

issue is the largely destructive nature of the process by which the samples are brought to a high energy density state. Thus, the sample replacement rate is slow, consuming much time, particularly when compared to the potential MHz repetition rates available with the Pump-Probe laser. Further, the repetition rate of many of the HED experiments will depend on optical lasers as the pump. In these cases the repetition rate will be dictated by the slower of the optical laser repetition rate or the sample replacement rate. On the other hand, for liquids and gases brought to the HED state, the accumulation of data at high repetition rates is clearly possible and the limit on the repetition rate will be dictated by the detectors.

This presentation indicated that a different way of performing HED experiments is needed at the European XFEL than that now employed at High Energy Laser facilities, as well as at femtosecond pulse laser facilities. This gave rise to a discussion of the importance of beam-sharing, in the following manner: It was indicated that the proposed mode of operation at the SASE-2 beamline was to have each of the two planned instruments (MID and HED) get 50% of the beam time each day for five days a week and then have a two-day period for the turnover of the instrument to a new experiment. Since the HED experiments may/will have a low repetition rate it is clear that a relatively rapid beam-sharing option could keep the SASE-2 beamline running at high efficiency. However, methods to provide stable, rapid beam-sharing require a concerted effort, which did not seem to be a priority. This may be of concern.

A brief discussion occurred concerning the use of FXE versus HED for the lower part of the energy range, i.e., 3 to 5 keV, which seemed a reasonable fall back position.

Presentation III: Contributions to HED from the Helmholtz User Consortium (Presenter – T. Cowan)

This presentation was essentially about “in-kind” contributions to the HED at European XFEL. To a large degree the efforts of Tom Cowan seem to be well received and quite successful. The Consortium is quite diverse and brings novel capabilities to the HED instrument. The foremost of these experiments entails a plan for a high intensity, i.e., TW-class, laser to produce relativistic

electron beams. The basic idea is to use the XFEL to study the interaction of these relativistic electron beams with solid density matter.

There were two questions that were left unclear: 1) There was a priority proposal system associated to the Consortium, but it was not made clear how this would work. 2) Further, additional diagnostics could be brought to the HED instrument by individual researchers, who would also be given priority access, and the manner in which this would occur was also not clear. However, as the issue of priority did not impinge on the brief to the committee, these questions may be addressed elsewhere.

The sense of the committee was unanimous in its approval of the contributions being derived from the Consortium.

Presentation IV: HED Beam Transport System (Presenter – M. Nakatsutsumi)

This straightforward talk that contained the description of the beamline optics, which, in addition to the standard attenuators, timing tools, collimators, etc. did include a split and delay unit, as well as a monochromator.

There were questions concerning the temporal structure of the pulse, which was described as having a large number of possible modes including everything from 1 pulse/second to 2700 pulse/second. These questions were addressed and resolved.

The one issue that arose in this part of the discussions was the need for a two-dimensional focal-plane intensity monitor that can verify the intensity pattern and possible overlap of the optical and X-ray beams. This question was left open.

Presentation V: The Experiment Room and Concept (Presenter – T. Tschentscher)

This presentation made it clear that the intent was to place three chambers in the HED experiment room. The general feeling was that this was at least one chamber too many. The general crowding that will occur when users bring experiment-specific instrumentation, e.g., sample viewers, will create an

extremely crowded workspace. It is understood that the number of chambers is derived from the need to make experimental change-overs in two days; however, the sense of the committee was that this may be difficult. A more detailed look at an experimental setup may illuminate the subject – see further comments in the wrap-up session.

There was a series of suggestions arising from the potential crowding in the experiment room, that concerned the placement of the VISAR and FDI systems. It was pointed out that the lasers for these devices, as well as the data collection apparatus, i.e., the streak cameras for the VISAR and the spectrometer for the FDI, along with some of the optical components could be placed above the HED experiment room in the laser room. This may be useful in relieving congestion in the experiment room.

Presentation VI: HED Focusing Concept (Presenter – M. Nakatsutsumi)

The discussion of the HED focusing was dominated by the use of compound beryllium lens. This choice seemed appropriate and the designs provided were well thought through. The ART asked for a verification that the proposed design can provide a variation of spot sizes. As discussed at the meeting there was a desire for foci between 50 and 200 μm , and it was requested that the information should be appropriate for the various chambers and include damage scenarios.

Presentation VII: The HED Laser plan (Presenter – T. Tschentscher)

The presentation of the laser plan was well received. The Pump-Probe laser provides a high-repetition rate and comments indicated that the repetition rate of the facility must be matched to the greatest extent possible. Again, although this is highly desirable, an independent determination of the potential for high-repetition rate HED experiments needs to be undertaken.

The group was in strong support of the high-intensity TW laser to be part of the contribution made by the Consortium. This laser required a laser room that would be built in a space that is not contiguous to the experiment room; however, it would be transported into the experimental room.

The selection of a ns-type laser scalable to 100 Joules and having a 10 Hz operation mode was discussed. There were two options, the first is a slab laser built by a company in the USA, National Energetics. The second is a diode pumped laser that has recently been demonstrated by a group in the UK. The latter seems to be scalable to 100 Joules and may be provided by the appropriate agency in the UK as an in-kind contribution. The committee was strongly in favor of pursuing the diode-pumped optical laser, as the technology is promising and may provide a very cost effective way forward to achieving high-repetition rate relatively high energy lasers. If possible the associated agency in the UK should be contacted to determine the possibilities.

Summary of the Open Discussion:

After all presentations the committee engaged in an open discussion of what could be done to move the CDR closer to its final form. Three main areas were discussed.

First, to ensure that nothing gets left out, the idea was proposed that two HED experiments be worked through in some detail to create a more complete knowledge of how the HED experiment room will function. To do this Tom Cowan would define an experiment using the TW beam to create relativistic electron beams and study their interaction within a solid density sample, while Andy Higginbotham would develop an experiment that would create a shock and measure the state of the shocked sample using diffraction, complemented with a VISAR and any other instrumentation necessary. In this way the level of instrumentation required in the HED experiment room can be better understood.

Second, there is a gap in the discussion when it comes to detector requirements. This was particularly noted for the HED experiments that will use diffraction as a diagnostic. In particular, the provision of a large area detector with high dynamic range and the possibility to achieve Q-ranges up to $\sim 10 \text{ \AA}^{-1}$ for scattering experiments at the HED instrument was considered important. However, the discussion of the HED instrument needs beyond those already included in the CDR, e.g., VISAR and FDI, need consideration.

At some level the exercise to develop the two experiments mentioned above may improve this situation.

Third, the CDR as written provides a great deal of information that may be more easily grasped if there was a sense of what must be 'dropped' if the various requirements laid out in the CDR are not realized. For example, if there is no 100J laser system, what other requirements are obviated – if any. Another way of looking at this is to include the “what ifs” to understand the interdependence of various aspects of the stated requirements.

Committee members

- R.W. Lee (LBNL) -chair-
- P. Audebert (LULI) -European XFEL SAC-
- A. Higginbotham (U Oxford)
- H. Lee (SLAC)
- H.-P. Liermann (DESY)
- D. Neely (STFC)
- P. Neumayer (GSI)
- K. Sokolowski-Tinten (U Duisburg)
- S. Toileikis (DESY)
- T. Cowan (HZDR) -guest/HIBEF UC

C References

- [1] Th. Tschentscher: “Layout of the X-Ray Systems at the European XFEL”, XFEL.EU TR-2011-001 (2011)
[doi:10.3204/XFEL.EU/TR-2011-001](https://doi.org/10.3204/XFEL.EU/TR-2011-001)
- [2] R. Brinkmann et al. (Eds.): “TESLA XFEL: First Stage of the X-Ray Laser laboratory – Technical Design Report – Supplement”, Preprint, DESY 2002-167, TESLA-FEL 2002-09
- [3] M. Altarelli et al. (eds.), “XFEL: The European X-ray Free-Electron Laser Technical Design Report”, DESY Report 2006-097 (2006)
[doi:10.3204/DESY_06-097](https://doi.org/10.3204/DESY_06-097)
- [4] A. Plech, V. Kotaidis, S. Gresillon, C. Dahmen, G. von Plessen: “Laser-induced heating and melting of gold nanoparticles studied by time-resolved x-ray scattering”, Phys. Rev. B **70**, 195423 (2004)
[doi:10.1103/PhysRevB.70.195423](https://doi.org/10.1103/PhysRevB.70.195423)
- [5] A. Rousse et al., “Non-thermalmelting in semiconductors measured at femtosecond resolution”, Nature **410**, 65 (2001).
[doi:10.1038/35065045](https://doi.org/10.1038/35065045)
- [6] K. Sokolowski-Tinten et al.: “Femtosecond X-ray measurement of coherent lattice vibrations near the Lindemann stability limit”, Nature **422**, 287 (2003).
[doi:10.1038/nature01490](https://doi.org/10.1038/nature01490)
- [7] D. M. Fritz et al.: “Ultrafast Bond Softening in Bismuth: Mapping a Solid's Interatomic Potential with X-rays”, Science **315**, 633 (2007).
[doi:10.1126/science.1135009](https://doi.org/10.1126/science.1135009)
- [8] V. Recoules, J. Cl  rouin, G. Z  rah, P.M. Anglade, and S. Mazevet: “Effect of Intense Laser Irradiation on the Lattice Stability of Semiconductors and Metals”, Phys. Rev. Lett. **96**, 055503 (2006)
[doi:10.1103/PhysRevLett.96.055503](https://doi.org/10.1103/PhysRevLett.96.055503)
- [9] F. Bottin and G. Z  rah: “Formation enthalpies of monovacancies in aluminum and gold under the condition of intense laser irradiation”, Phys. Rev. B **75**, 174114 (2007)
[doi:10.1103/PhysRevB.75.174114](https://doi.org/10.1103/PhysRevB.75.174114)

- [10] F. Dorchies et al.: LCLS experiment L532 “Unravelling the non-equilibrium electron – ion ultrafast dynamics in warm dense Mo and Ag with time-resolved XANES”
- [11] D.K. Bradley et al.: “Diamond at 800 GPa”,
Phys. Rev. Lett. **102**, 075503 (2009)
[doi:10.1103/PhysRevLett.102.075503](https://doi.org/10.1103/PhysRevLett.102.075503)
- [12] C.J. Pickard and R.J. Needs: “Aluminium at terapascal pressures”,
Nature Materials **9**, 624 (2010)
[doi:10.1038/nmat2796](https://doi.org/10.1038/nmat2796)
- [13] D.C. Swift et al.: “Mass-radius relationships for exoplanets”,
Astrophys. J., **744**, 59 (2012).
[doi:10.1088/0004-637X/744/1/59](https://doi.org/10.1088/0004-637X/744/1/59)
- [14] D.E. Frantanduono et al.: “The direct measurement of ablation pressure driven by 351-nm laser radiation”,
J. Appl. Phys. **110**, 073110 (2011)
[doi:10.1063/1.3646554](https://doi.org/10.1063/1.3646554)
- [15] J.P.C. Ruff et al.: “Magnetoelastics of a Spin Liquid: X-Ray Diffraction Studies of Tb₂Ti₂O₇ in Pulsed Magnetic Fields”,
Phys. Rev. Lett. **105**, 077203 (2010)
[doi:10.1103/PhysRevLett.105.077203](https://doi.org/10.1103/PhysRevLett.105.077203)
- [16] T. Inami et al.: “Resonant magnetic x-ray diffraction study on the successive metamagnetic transitions of TbB₄ up to 30 T”,
J Physics CS **211**, 012010 (2010)
[doi:10.1088/1742-6596/211/1/012010](https://doi.org/10.1088/1742-6596/211/1/012010)
- [17] S. Yoshii et al.: “Multistep Magnetization Plateaus in the Shastry-Sutherland System TbB₄”,
Phys. Rev. Lett. **101**, 087202 (2008)
[doi:10.1103/PhysRevLett.101.087202](https://doi.org/10.1103/PhysRevLett.101.087202)
- [18] B. Nagler et al.: “Turning solid aluminium transparent by intense soft X-ray photoionization”, Nature Phys. **5**, 693, (2009)
[doi:10.1103/PhysRevLett.101.087202](https://doi.org/10.1103/PhysRevLett.101.087202)
- [19] A. Levy et al., submitted
- [20] Y. Sentoku, A. J. Kemp, R. Presura, M.S. Bakeman, and T.E. Cowan: “Isochoric heating in heterogeneous solid targets with ultrashort laser pulses”, Phys. Plasmas **14**, 122701 (2007)
[doi:10.1063/1.2816439](https://doi.org/10.1063/1.2816439)

- [21] A. Di Piazza, C. Müller, K.Z. Hatsagortsyan, C.H. Keitel: “Extremely high-intensity laser interactions with fundamental quantum systems”, *Rev. Mod. Phys.* **84**, 1202 (2012)
[doi:10.1103/RevModPhys.84.1177](https://doi.org/10.1103/RevModPhys.84.1177)
- [22] Y.I. Salamin, S.X. Huc, K.Z. Hatsagortsyana, C.H. Keitela: “Relativistic high-power laser–matter interactions”, *Phys. Rept.* **427**, 41 (2006)
[doi:10.1016/j.physrep.2006.01.002](https://doi.org/10.1016/j.physrep.2006.01.002)
- [23] M. Marklund, P.K. Shukla: “Nonlinear collective effects in photon-photon and photon-plasma interactions”, *Rev. Mod. Phys.* **78**, 591 (2006)
[doi:10.1103/RevModPhys.78.591](https://doi.org/10.1103/RevModPhys.78.591)
- [24] O. Klein: “Die Reflexion von Elektronen an einem Potentialsprung nach der relativistischen Dynamik von Dirac”, *Zeitschrift für Physik* **53**, 157 (1929)
[doi:10.1007/BF01339716](https://doi.org/10.1007/BF01339716)
- [25] T. Heinzl, B. Liesfeld, K.U. Amthor, H. Schwöerer, R. Sauerbrey, A. Wipf: “On the observation of vacuum birefringence”, *Opt. Commun.* **267**, 318 (2006)
[doi:10.1016/j.optcom.2006.06.053](https://doi.org/10.1016/j.optcom.2006.06.053)
T. Heinzl, A. Ilderton: “Exploring high-intensity QED at ELI”, *Eur. Phys. J. D* **55**, 359–364
[doi:10.1140/epjd/e2009-00113-x](https://doi.org/10.1140/epjd/e2009-00113-x)
- [26] B. Marx et al.: “Determination of high-purity polarization state of X-rays”, *Optics Comm.* **284**, 915 (2011)
[doi:10.1016/j.optcom.2010.10.054](https://doi.org/10.1016/j.optcom.2010.10.054)
- [27] K. Homma, D. Habs, T. Tajima: “Probing vacuum birefringence by phase-contrast Fourier imaging under fields of high-intensity lasers”, *Appl. Phys. B* **104**, 769 (2011)
[doi:10.1007/s00340-011-4568-2](https://doi.org/10.1007/s00340-011-4568-2)
- [28] A. Di Piazza, K.Z. Hatsagortsyan, C.H. Keitel: “Enhancement of vacuum polarization effects in a plasma”, *Phys. Plasmas* **14**, 032102 (2007)
[doi:10.1063/1.2646541](https://doi.org/10.1063/1.2646541)
- [29] The Center for X-Ray Optics, Lawrence Berkeley National Laboratory, Materials Sciences Division: “X-Ray Interactions With Matter”,
http://henke.lbl.gov/optical_constants/
- [30] S. Vinko et al.: “Creation and diagnosis of a solid-density plasma with an X-ray free-electron laser”, *Nature* **482**, 59 (2012)
[doi:10.1038/nature10746](https://doi.org/10.1038/nature10746)

- [31] A. Benuzzi-Mounaix et al.: “Electronic Structure Investigation of Highly Compressed Aluminum with K Edge Absorption Spectroscopy”, *Phys. Rev. Lett.* **107**, 165006 (2011).
[doi:10.1103/PhysRevLett.107.165006](https://doi.org/10.1103/PhysRevLett.107.165006)
- [32] S.H. Glenzer, R. Redmer: “X-ray Thomson scattering in high energy density plasmas”, *Rev. Mod. Phys.* **81**, 1625 (2009)
[doi:10.1103/RevModPhys.81.1625](https://doi.org/10.1103/RevModPhys.81.1625)
- [33] G. Geloni, V. Kocharyanb, E. Saldinb: “A novel self-seeding scheme for hard X-ray FELs”, *J. Mod. Opt.* **58**, 1391 (2011)
[doi:10.1080/09500340.2011.586473](https://doi.org/10.1080/09500340.2011.586473)
- [34] J. Amann et al.: “Demonstration of self-seeding in a hard-X-ray free-electron laser”, *Nature Photonics* **6**, 693–698 (2012)
[doi:10.1038/nphoton.2012.180](https://doi.org/10.1038/nphoton.2012.180)
- [35] E.A. Schneidmiller, M.V. Yurkov, “Photon beam properties at the European XFEL”, XFEL.EU TR-2011-006 (2011)
[doi:10.3204/DESY11-152](https://doi.org/10.3204/DESY11-152)
- [36] H. Sinn, J. Gaudin, L. Samoylova, A.Trapp, G. Galasso: “Conceptual Design Report: X-Ray Optics and Beam Transport”, XFEL.EU TR-2011-002 (2011)
[doi:10.3204/XFEL.EU/TR-2011-002](https://doi.org/10.3204/XFEL.EU/TR-2011-002)
- [37] B. Lengeler et al., “Imaging by parabolic refractive lenses in the hard X-ray range”, *J. Synchrotron Rad.* **6**, 1153 (1999)
[doi:10.1107/S0909049599009747](https://doi.org/10.1107/S0909049599009747)
- [38] S.P. Hau-Riege et al.: “Interaction of short X-ray pulses with low-Z X-ray optics materials at the LCLS free-electron laser”, *Opt. Exp.* **18**, 23933 (2010)
[doi:10.1364/OE.18.023933](https://doi.org/10.1364/OE.18.023933)
- [39] C.M. Günther et al.: “Sequential femtosecond X-ray imaging”, *Nat. Photonics* **5**, 99 (2011)
[doi:10.1038/nphoton.2010.287](https://doi.org/10.1038/nphoton.2010.287)
- [40] S. Roling et al.: “Temporal and spatial coherence properties of free-electron-laser pulses in the extreme ultraviolet regime”, *Phys. Rev. St. AB* **14**, 080701(2011)
[doi:10.1103/PhysRevSTAB.14.080701](https://doi.org/10.1103/PhysRevSTAB.14.080701)
- [41] R. Mitzner et al.: “Spatio-temporal coherence of free electron laser pulses in the soft X-ray regime”, *Opt. Exp.* **16**, 19909 (2008)
[doi:10.1364/OE.16.019909](https://doi.org/10.1364/OE.16.019909)

- [42] S. Roling et al.: Proc. SPIE 8504, 850407 (2012)
- [43] H. Sinn, M. Dommach, X. Dong, D. La Civita, L. Samoylova, R. Villanueva, F. Yang: "Technical Design Report: X-Ray Optics and Beam Transport", XFEL.EU TR-2012-006 (2012)
[doi:10.3204/XFEL.EU/TR-2012-006](https://doi.org/10.3204/XFEL.EU/TR-2012-006)
- [44] Ch. Bressler, A. Galler, W. Gawelda: "Technical Design Report: Scientific Instrument FXE", XFEL.EU TR-2012-008 (2012)
[doi:10.3204/XFEL.EU/TR-2012-008](https://doi.org/10.3204/XFEL.EU/TR-2012-008)
- [45] J. Grünert, "Conceptual Design Report: Framework for X-Ray Photon Diagnostics at the European XFEL", XFEL.EU TR-2012-003 (2012)
[doi:10.3204/XFEL.EU/TR-2012-003](https://doi.org/10.3204/XFEL.EU/TR-2012-003)
J. Buck, "Conceptual Design Report: Online Time-of-Flight Photoemission Spectrometer for X-ray Photon Diagnostics", XFEL.EU TR-2012-002 (2012)
[doi:10.3204/XFEL.EU/TR-2012-002](https://doi.org/10.3204/XFEL.EU/TR-2012-002)
- [46] C.A. Heynam et al., "National Ignition Facility laser performance status", Appl. Opt. **46**, 3276 (2007).
[doi:10.1364/AO.46.003276](https://doi.org/10.1364/AO.46.003276)
- [47] M.J. Lederer, M. Pergament, M. Kellert, C. Mendez: Proc. SPIE **8504**, (2012), X-ray Free-Electron Lasers: Beam Diagnostics, Beamline Instrumentation, and Applications, San Diego, USA (08/12/2012)
- [48] G. Cerullo and S. De Silvestria, "Ultrafast optical parametric amplifiers" Rev. Sci. Inst. **74**, 1 (2003)
[doi:10.1063/1.1523642](https://doi.org/10.1063/1.1523642)
- [49] H. Yoneda, H. Morikami, K. Ueda, R.M. More: "Ultrashort-Pulse Laser Ellipsometric Pump-Probe Experiments on Gold Targets", Phys. Rev. Lett. **91**, 075004 (2003)
[doi:10.1103/PhysRevLett.91.075004](https://doi.org/10.1103/PhysRevLett.91.075004)
- [50] J.-P. Geindre, P. Audebert, S. Rebibo, J.-C. Gauthier. "Single-shot spectral interferometry with chirped pulses", Opt. Lett. **26**, 1612 (2001)
[doi:10.1103/PhysRevLett.91.075004](https://doi.org/10.1103/PhysRevLett.91.075004)
- [51] A. Jullien et al.: "10⁻¹⁰ temporal contrast for femtosecond ultraintense lasers by cross-polarized wave generation", Opt. Lett. **30**, 920 (2005)
[doi:10.1364/OL.30.000920](https://doi.org/10.1364/OL.30.000920)

- [52] P.M. Celliers et al.: “Line-imaging velocimeter for shock diagnostics at the OMEGA laser facility”, Rev. Sci. Inst. **75**, 4916 (2004)
[doi:10.1063/1.1807008](https://doi.org/10.1063/1.1807008)
- [53] J.E. Miller et al., “Streaked optical pyrometer system for laser-driven shock-wave experiments on OMEGA”, Rev. Sci. Inst. **78**, 034903 (2007)
[doi:10.1063/1.2712189](https://doi.org/10.1063/1.2712189)
- [54] M.R. Bionta et al.: “Spectral encoding of X-ray/optical relative delay”, Opt. Exp. **19**, 21855 (2011)
[doi:10.1364/OE.19.021855](https://doi.org/10.1364/OE.19.021855)
- [55] M. Harmand et al.: “Achieving few-femtosecond time-sorting at hard X-ray free-electron lasers”, Nature Photonics **7**, 215, (2013)
[doi:10.1038/nphoton.2013.11](https://doi.org/10.1038/nphoton.2013.11)
- [56] Y. Asano: “Shielding design calculation for SPring-8 beamlines using STAC8”, J. Synchrotron Rad. **5**, 615 (1998).
[doi:10.1107/S0909049597019249](https://doi.org/10.1107/S0909049597019249)
- [57] A. Fasso, A. Ferrari, J. Ranft, P.R. Sala, “FLUKA: a multi-particle transport code”, CERN-2005-10 (2005), INFN/TC_05/11, SLAC-R-773; G. Battistoni et al., “The FLUKA code: description and benchmarking”, Proceeding of the Hadronic Shower Simulation Workshop 2006, Fermilab 6–8 September 2006, M. Albrow, R. Raja editors, AIP Conference Proceeding **896**, 31 (2007)
- [58] K. Zeil et al.: “The scaling of proton energies in ultrashort pulse laser plasma acceleration”, New J. Phys. **12** 045015 (2010)
[doi:10.1088/1367-2630/12/4/045015](https://doi.org/10.1088/1367-2630/12/4/045015)
- [59] T. Kluge T. Cowan, A. Debus, U. Schramm, K. Zeil, M. Bussmann: “Electron temperature scaling in laser interaction with solids”, Phys. Rev. Lett. **107**, 205003 (2011)
[doi:10.1103/PhysRevLett.107.205003](https://doi.org/10.1103/PhysRevLett.107.205003)